Evaluation of NDT Technologies to Assess Presence and Extent of Delamination of HMA Airfield Pavements

Volume I: Technical Report

Conducted for
Airfield Asphalt Pavement Technology Program
Federal Aviation Administration
AAPTP Research Project 06-04

March 2010

Center for Transportation Infrastructure Systems
The University of Texas at El Paso
El Paso, TX 79968
(915) 747-6925

Evaluation of NDT Technologies to Assess Presence and Extent of Delamination of HMA Airfield Pavements

Volume I: Technical Report

by

Manuel Celaya, MSCE, EIT
Dante Mejía, BSCE
Selcan Ertem, MSCE
Soheil Nazarian, Ph.D., PE
Chetana Rao, Ph.D., PE
Harold Von Quintus, PE
Parisa Shokouhi, Ph.D.

AAPTP Research Project 06-04
Non-Destructive Testing to Identify Presence and Extent of Delamination of HMA Airfield Pavements

Conducted for
Airfield Asphalt Pavement Technology Program
in cooperation with the Federal Aviation Administration

March 2010

Center for Transportation Infrastructure Systems
The University of Texas at El Paso
El Paso, TX 79968-0516

ACKNOWLEDGEMENT OF SPONSORSHIP

This report has been prepared for Auburn University under the Airport Asphalt Pavement Technology Program (AAPTP). Funding is provided by the Federal Aviation Administration (FAA) under Cooperative Agreement Number 04-G-038. Dr. David Brill is the Contracting Officer, Technical Representative, and serves as a Program Manager in the FAA Airport Technology Branch at the William J. Hughes Technical Center. Mr. Monte Symons served as the Project Director for this project.

The AAPTP and the FAA thank the Project Technical Panel that willingly gave of their expertise and time for the development of this report. They were responsible for the oversight and technical direction. The names of those individuals on the Project Technical Panel follow:

1. Rodney Joel
2. Kathleen T. Hall
3. Gary Harvey
4. Luis Rodriquez
5. Monte Symons

DISCLAIMER

TABLE OF CONTENTS

LIST OF FIGURES

LIST OF TABLES

ACKNOWLEDGEMENTS

The authors wish to acknowledge Miss Selcan Ertem and Mr. Dante Mejía of UTEP for their contributions to this project. Our appreciation is also extended to Ms. Joanna Ambroz and Mr. Stewart Craig of Portland International Airport and Mr. Robert Pellan, Mr. Ben Barrett, and Mr. Tom Pyle of Boston Logan International Airport.

ABSTRACT

Sufficient bonding between the hot mix asphalt layers is essential to ensure the desired structural capacity of a pavement. Delamination or debonding problems are particularly more severe on airfield pavements, due to higher traffic loads applied by aircrafts. Further progression of delamination may result in stripping of the lower layers due to the intrusion of moisture or may develop other dangerous distresses such as foreign object debris. The existing nondestructive testing procedures and equipment that have the potential to address the problem were identified and their effectiveness and potential for success were evaluated. The Ground Penetrating Radar, Falling Weight Deflectometer, Thermography, Sonic/Seismic Methods and Impulse Response were evaluated on a controlled pavement section that was specifically constructed with various levels and depths of debonding and two airfields. Most technologies can detect severe delamination successfully. Even though not perfect, the impulse response method (with a site specific temperature adjustment) and ultrasonic surface wave method are the most promising methods for detecting debonded sections.

SUMMARY OF FINDINGS

In this study, the existing NDT procedures and equipment that have the potential to detect the debonding and delamination of hot mix asphalt (HMA) layers were identified and their effectiveness and potential for success were evaluated. Based on literature survey and analyses of the technical and practical strength and concerns, the methods considered for evaluation are summarized in Table I.

Table I – Methods Considered for Evaluation in This Study

Method / Device									
Electro-magnetic	**Impulse**			**Vibration**		**Seismic/Sonic**			**Thermal**
Air-launched and Ground-Coupled Ground Penetrating Radar (GPR)	Falling Weight Deflectometer (FWD)	Light Weight Deflectometer (LWD)	Impulse Response (IR)	Stiffness Gauge (SG)	High Frequency Sweep (HFS)	Impact Echo (IE)	Ultrasonic Surface Waves (USW)	Ultrasound (US)	Thermal Imaging (TI)

For a rigorous experimental evaluation of these methods, a 130 ft by 9 ft pavement section containing ten distinct sections was constructed with known sizes (from 6 in. by 6 in. to 4 ft by 4ft), depths (2.5 in. and 5 in.), severity (partial-debonding, full-debonding and severe delamination), surface mix (fine and coarse mixes) and climatic condition (cool and hot). Based on an initial evaluation, the feasible technologies were narrowed down to the methods shown in Table II.

The technical and practical parameters that most likely affect the successful detection of delamination with NDT methods include the accuracy, reproducibility, detectability threshold, speed of data collection, speed of data analysis, and the sophistication of data analysis.

Table II – Methods Found Feasible from Phase I Field Study

Electromagnetic	Impulse		Seismic/Sonic
Ground-Coupled Ground Penetrating Radar (GPR)	Falling Weight Deflectometer (FWD)	Impulse Response (IR)	Ultrasonic Surface Waves (USW)

The ***accuracy*** was judged by correlating the response of the NDT methods to the degree of debonding induced in the sections. The ***reproducibility*** associated with different test procedures was quantified by conducting triplicate tests with each NDT device. The ***detectability threshold*** was assessed by the percent of defects identified as a function of size, depth and severity. The ***speed of data collection*** was judged based on the time needed to set up and test time per point. The time to complete the analysis of the raw data for each methodology was used to assess the ***speed of analysis.*** The ***sophistication of data analysis*** was estimated by asking personnel with different levels of experience (an expert, a person that is familiar with the method and a new user that was just trained) to conduct the analysis. The parameters described above were given relative weights as shown in Table III to determine an overall ranking for different methods.

The rankings of the methods are shown in Table IV. None of the methods could find all of the debonded areas. However, some methods performed better for some certain application. Table V demonstrates the best applications of each method. Based on the outcome of the study, the following statements can be made:

- The impulse-response method could detect about 59% of the debonded areas with the majority of defects detected were the fully-debonded areas (both shallow and deep).
- The USW method as implemented in the PSPA could detect 53% of the debonded areas. PSPA could detect the shallow debonding (both partial and full) the best.

Table III – Weight Factors of Parameters Used in Evaluation of Methods

Evaluation Category	Relative Weight
Accuracy	0.35
Reproducibility	0.20
Detectability Threshold	0.20
Speed of Data Collection	0.15
Speed of Data Analysis	0.05
Sophistication of Data Analysis	0.05
Total	**1.00**

Table IV – Ranking of Most Feasible Methods

Parameter / Method	Accuracy	Reproducibility	Detectability Threshold	Speed of Data Collection	Speed of Data Analysis	Sophistication of Data Analysis	Ranking
	Weight Factor						
	0.35	0.2	0.2	0.15	0.05	0.05	
PSPA Ultrasonic Surface waves	3	3	3	3	3	3	2
FWD Modulus	2	3	1	3	3	3	3
Impulse Response Flexibility	4	5	3	3	3	3	1
Ground Coupled GPR	1	5	1	5	1	1	4

Table V – Recommended Best Applications for Most Feasible Methods

Defect Type		Detection Ranking			
Depth	**Bonding**	**PSPA**	**IR**	**FWD (Def.)**	**GPR**
Deep	**Fully Debonded**		√		
	Partially Debonded		**?**		
Shallow	**Fully Debonded**	√	√	√	√
	Partially Debonded	√			
Severe Delamination		√	√	√	√

- The FWD could detect about 46% of the debonded areas (primarily full debonding) based on the backcalculation of the modulus of the HMA layer.
- GPR could detect 33% of the debonded areas, primarily when talcum powder or clay was used as the debonding agent. GPR could be used as a qualitatively method to identify severely debonded areas, especially in the presence of moisture.

The evaluation of the technologies was carried out both in the cool weather and hot weather. Almost all methods either performed equally well or better in the cool weather. One major practical recommendation of this study is that the IR, FWD and USW methods require temperature adjustments for their success. Approximate temperature adjustment relationships exist for the USW and FWD methods. However, for the IR a site specific temperature adjustment protocol may be needed.

The feasible methods recommended by this study can be significantly improved by implementing more sophisticated yet practical analysis schemes.

CHAPTER 1

INTRODUCTION

To achieve the desired bearing capacity of a pavement structure and, as a result, a longer service life, sufficient bonding between the pavement layers is essential. Other than a reduction in the structural bearing capacity, a poor bond and the subsequent delamination or debonding between the surfacing layers reduces the serviceability and pavement performance. If delamination goes undetected, it can ultimately result in the peeling away of thin overlays from the surface of the roadway.

Delamination or debonding problems are particularly more severe on airfield pavements, due to higher traffic loads applied by aircrafts. Especially, the situation is more critical on runways at the high-speed taxiway exits, where airplanes brake and turn (Bognacki et al., 2007), or on areas under large horizontal load of aircraft at takeoff, creating slippage due to inadequate bonding between the top layer and the layer below. In severe cases, it can lead to runway closures (Tsubokawa et al., 2007). As an example, Figure 1.1 shows a case of asphalt delamination that occurred due to loss of bond between the surface and binder courses for a runway constructed only one year before the incident. In this case, the thickness of the surface course that suffered delamination was 2 in., the slippage area was 12 ft wide and 25 ft long, and the runway had to be closed for repairs.

Some other studies have found that the cause of airport delamination can be attributed to intersection of multiple-traffic paths on runways and large shear forces caused by pivoting wheels (Carroll and Dempsey, 2007). Delamination problems in airfield pavements are often preceded by slippage failures that can be detected by the presence of curved grooves on the surface, as illustrated in Figure 1.2, (Bognacki et al., 2007) or half-moon-shaped cracks having

Figure 1.1 – Slippage Failure due to Loss of Bond at Nagoya Airport (from Tsubokawa et al., 2007)

Figure 1.2 – Slippage at High-Speed Taxiway ("Curved" Grooves Indicate Slippage, Bognacki et al., 2007)

two ends pointed away from the direction of traffic, as detailed in Figure 1.3 (Shahin, 2005). These debonding and slippage problems can be aggravated with aggregate with inadequate aggregate interlock used in the asphalt pavement or insufficient amount of tack coat between layers (Bognacki et al., 2007).

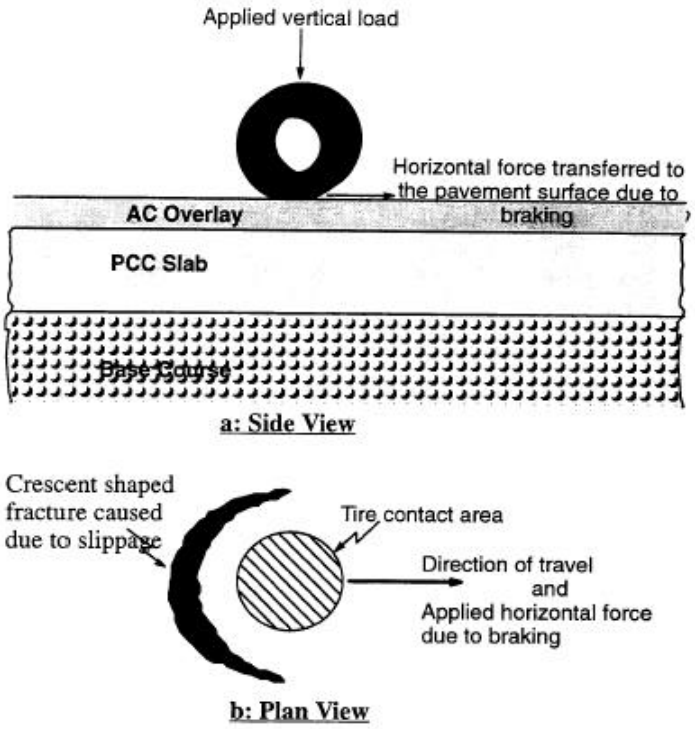

Figure 1.3 – Typical Slippage Failure (from Kulkarni, 2004)

Besides the risk of damage to the aircrafts because of foreign object debris (FOD), the delaminated layers and their associated cracks require recurrent maintenance activities, and may lead to premature need for major rehabilitation of the airfields. If undetected, the progression of delamination may result in stripping of the lower layers due to the intrusion of moisture.

The objective of this study was to provide a comprehensive procedure and guidance to estimate the presence and extent of hot mix asphalt (HMA) delamination in airport pavements. To that end, nondestructive procedures capable of locating areas of delamination were identified, tested and conclusions on their applicability were drawn.

Common conditions of past instances of major damage to airport HMA pavements resulting from delamination are identified, and the key indicators that may be used to identify potential areas of delamination are discussed in Chapter 2. The existing nondestructive test (NDT) procedures and/or equipment that have been used or have the potential to address the

problem are identified and their effectiveness and potential for success are evaluated in Chapter 3. The more effective methods are then more critically studied.

Chapter 4 details the construction of a control pavement section with different types, severity and depths of debonding and Chapter 5 contains the preliminary evaluation of several NDT methods on the control section. Chapter 6 describes the verification tests of selected NDT methods on the same control section.

The results from field investigation of selected NDT methods at two actual airfields are presented in Chapter 7. Chapter 8 includes the evaluation of NDT methods based on results obtained from the control section and the recommendation of most promising methods for detecting delamination of HMA. Finally, Chapter 9 presents the summary and conclusions of this report.

CHAPTER 2

DELAMINATION OF HMA AIRPORT PAVEMENTS

Three modes of debonding or delamination can occur: 1) delamination between two layers/lifts of HMA, 2) debonding between HMA overlay and portland cement concrete (PCC) slab, and 3) debonding between base and HMA. All three modes impact the structural and functional performance of the airfields. However, the most critical ones are the shallow delamination of two HMA layers and debonding of thin HMA overlays over PCC slabs.

The lack of interface bonding may lead to several premature distresses of which slippage, cracking, delamination and distortion are most prominent. In most cases, delamination occurs either at high temperature or very high loads (especially horizontal loads) or a combination of the two when there is a poor bond between the surface and binder courses. Therefore, special attention has to be given to areas where horizontal loads are the largest such as frequent braking and accelerating zones, sharp curves or at the intersection of multiple-traffic paths.

Manifestation of delamination and its detrimental effects are perhaps more severe on airfield pavements, due to higher loads applied by aircrafts. The situation is most critical on runways at the high-speed taxiway exits, where airplanes brake and turn (Bognacki et al., 2007). In areas under large horizontal loads where aircrafts turn or break or takeoff, slippage due to inadequate bonding between the different lifts of the surface layer are also of particular concern (Tsubokawa et al., 2007). Delamination may also occur at the intersection of multiple-traffic paths on runways where large shear forces are exerted by pivoting wheels (Carroll and Dempsey, 2007). Jet blasts can particularly complicate the problem by converting fragments of the delaminated layer into foreign object debris (FOD).

Some construction practices in airfield industry may also aggravate the occurrence of delamination defects. For example, smoothness criteria and its tight tolerance required by the FAA drive contractors into constructing pavements with multiple thinner lifts rather than fewer thicker lifts. Multiple layers may not act as one solid unit under shear forces and are therefore, more delamination susceptible. On the other hand, such defects could be avoided by treating and cleaning the surfaces of dust and debris and applying sufficient amount of tack coat prior to placing the overlay. Other factors such as leakage of jet turbine fluids and exhausts on the airfield pavements are considered responsible for delamination problems on military airports (Department of the Air Force, 2002, Newman, and Shoenberger, 2002).

Asphalt layer thickness plays a key role in preventing delamination. Increasing layer thickness reduces the interfacial shear stress, due to vertical and horizontal loads (Kulkarni, 2004). Even though the presence of a delaminated layer at any depth is undesirable, Hammons et al. (2005) have shown that under truck traffic, the delamination or even stripping deeper than 8 in. impacts the performance of the pavement less significantly, and the risk of surface distress is small (Hammons et al., 2005). As such, the focus of delamination detection should be on layers close to the surface (say the top 5 in.).

Other experimental studies have shown that the interface properties depend more seriously on the type of materials in contact, rather than on the amount of the applied tack coat and the interface condition (Kruntcheva et al., 2006). In that study it was suggested that the interface bond should be described by introducing a vertical shear reaction modulus (against uplifting of the asphalt layer) as well as the horizontal shear reaction modulus.

Generally speaking, for the pavement to be structurally and functionally sound, a proper interface bonding between the upper and lower HMA layers is necessary. The Asphalt Institute

MS-16 manual indicates that slippage cracks result from a lack of bond between the surface and the layer beneath. Distortion, a result of asphalt layer instability, can take a number of different forms such as shoving, pushing, corrugation or rutting. Corrugation is a form of plastic movement typified by ripples across the asphalt surface which occurs usually at intersections where there is acceleration or deceleration of vehicles. This distress is a functional failure of the pavement and can affect the ride quality and safety. The development of slippage cracks, crescent or half-moon shaped, is also a result of poor interfacial bond. In this distress, under the shearing action of the traffic, the asphalt mix moves laterally away from the rest of the surface. Some reasons for a lack of bonding between the asphalt layers are:

- Poor condition of the old pavement - presence of dust, oil, rubber, dirt, water or any other non-adhesive materials;
- Application of excessive, inadequate or non-uniform tack coat;
- Highly polished aggregate on existing surface which may be water sensitive and/or use of tack coat that may not be compatible with the polished aggregates;
- Use of mixture having a high sand content, especially with rounded particles;
- Use of improper construction technique and lack of proper degree of compaction of the HMA layer.

In summary, the debonding or delamination could be caused by any one or a combination of any of the factors listed above. In addition to the above criteria, the following factors may contribute to the delamination: (a) improper consideration of temperature and field conditions, (b) excessive load repetitions and vehicular accelerations and, (c) very thin surface layer thickness. In practice, most of the delamination distresses can be attributed to either improper

construction techniques or choice of inappropriate tack coat. Pertinent research conducted in the area of HMA concrete delamination is briefly described below.

Mohammad et al (2002) measured the influence of different tack coats on the interface shear strength of adjacent layers. They conducted a load-controlled, simple shear test by shearing the specimens at interface. Lateral confinement was provided by a collar (Figure 2.1) that ensured the failure was at interface and nowhere else. The specimens were manufactured in three steps:

- Compact the 'bottom' part of the specimen in a Superpave gyratory compactor
- After cooling, apply the tack coat at the specified rate
- Insert the 'bottom' specimen in the gyratory mold, pour loose asphalt mix over the tack coat, and compact.

The target air void content for each of the bottom and top specimens was 6%. Each of those specimens was tested in a SST machine at a loading rate of 50 lb/min until failure. The testing was conducted at temperatures of 25°C and 55°C. It was observed that CRS-2P emulsion performed better than PG64-22, PG76-22M, SS-1, SS-1H, and CSS-1h. In addition, for each of the tack coats, an optimum rate of application that gave the highest shear strength was determined. The study demonstrated that even under the most optimal performance of tack coat, the maximum strength attained is only 83% of monolithic mixture strength, implying that interfaces potentially cause slip planes.

Shahin et al (1986) discussed the effect of layer slippage on the performance of asphalt pavements. Using BISAR (Bituminous Structures Analysis in Roads) and the French Shell model (Bonnaure et al., 1980) for analysis, various scenarios were evaluated about the fatigue life of a typical airfield pavement. The pavement section analyzed had a 2-inch thick overlay

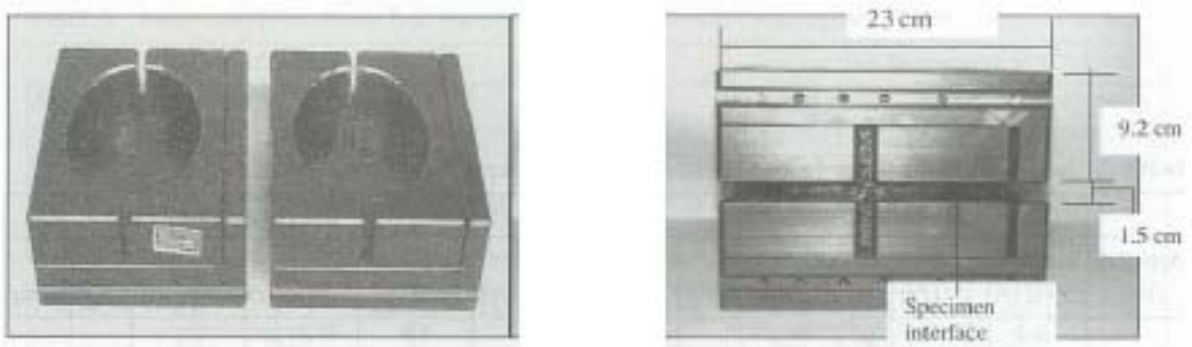

(a) Collars to provide lateral confinement (b) Assembled collars with specimen inside

Figure 2.1 – Collars Designed for Testing Samples in Shear (Mohammad et al., 2002)

over a 4-inch thick HMA surface course. The criteria for failure considered were the tensile stress at the bottom of the asphalt layers (overlay and the original surface course) and the vertical compressive strain on the subgrade. Shahin et al. (1986) made the following observations:

- Only a small amount of slippage is sufficient to produce strains in the pavement that approach those of the free slippage case.
- The tensile stress at the bottom of the overlay causes a compressive stress to develop on the upper surface of the asphalt surface layer. This causes a relative movement of points on the either side of the interface. This distortion further weakens the bond between the asphalt layers, allowing more slippage leading to higher strains.
- The subgrade strains increase with increasing slippage. Because two thinner layers are not as stiff as a single layer of the same overall thickness, the compressive vertical strain on the subgrade increases.
- Further, under the action of horizontal loads, the horizontal strains for no friction are much higher than those with full friction.

The principal normal tensile strains, developed by the horizontal loads along the back edge of the contact area, are of the same magnitude and cause progressive failure along the rear

edge. This tensile failure would cause slippage cracks in the overlay. If the overlay is not properly bonded to the underlying layers, the overlay moves resulting in opening of the cracks. These cracks are crescent shaped. In order to fix these cracks, either the existing layer needs to be removed and re-paved or a thicker well-bonded overlay should be placed on the existing overlay. In addition to strong interlayer bonding, the authors suggested an overlay stiffness of at least 500 ksi.

A research to evaluate the adhesion between asphalt mixes was conducted by Uzan (1976) and Uzan et al. (1978) using the Goodman's constitutive law:

$$\tau = \boldsymbol{K} \times \Delta \boldsymbol{u} \tag{2.1}$$

where τ is the shear stress at interface, Δu the relative horizontal displacement of the two faces at the interface, and K is the horizontal interface reaction modulus.

The analysis was carried out using the BISAR program for a test section at different levels of adhesion. It was observed that for a perfectly smooth interface (K=0) the tensile radial strain at the bottom of the uppermost layer was higher than for the perfectly rough interface. The top of the second layer also changed to compressive strain when K approached zero. Further, even an adherence of 90% provides results that were close to a smooth condition as described in Shahin et al. (1986). Direct shear tests were performed on the layered asphalt concrete specimens with shearing along the tack coat at different temperatures, vertical pressures and rates of application of tack coat. The following three components that contribute to the interface shear strength were identified:

- Adhesion, represented by the tensile properties of the slip plane.
- Friction, from roughness of the two faces.

- Interlocking, from the penetration of aggregates into the voids of the other layer. The interlocking component depends on the texture of the surfaces in contact and properties of the asphalt mix.

It was suggested that measurement of the adhesion component, which is indicated by rupture of the bond between layers in the bitumen or mastic phase, could be done by a tensile test (the interlocking effect would be absent for pure tension.).

The following factors largely influenced the interface shear strength:

- *Temperature:* The effect of higher temperatures is more dominant while testing in tension than in compression. With increasing vertical pressures, the interlocking component becomes more dominant than the adhesion component.
- *Tack Coat Rate:* The tack coat usually functions in the following two ways:
    - Fills voids on the surface.
    - Increases the interface film thickness or gets absorbed in the adjacent layers.

The filling of voids on the surface of the mixes increases the contact area and consequently the adhesion. However, excessive film thickness decreases the adhesion and aggregate interlock. Very low tack coat rate could result in the loss of adhesion component. Hence, it is required that the tack coat be applied at an optimum rate.

- *Rate of Deformation:* The rate of shear deformation is an important factor in controlling the strength and deformation ability of the interface. Generally, with increasing the rate of deformation, the magnitude of stress developed increases.

A common method for measuring the bond strength of asphalt cores is the pull-off test (Tschegg et al., 1995). For this test, a 4-in.-diameter core is drilled from the top surface down through the overlay, through the interface, and about 2 in. into the base layer. A Steel plate is

glued to the top surface of the core. The core is then pulled off with a tension machine in the axial direction of the base layer. The maximum load is registered during the pull-off test. This is a simple test method but gives only the adhesive tensile strength with large scatter in the results. The reasons for the scatter in the results are: eccentricity of load, small core diameter and large aggregate size, notches at the surface of the cores by drilling or burst out aggregates, stress concentrations, uncontrolled temperature, and indentation effects owing to rough surfaces. In addition, the test was useless if the tensile strength of the mix was lower than the interface bond strength.

To avoid such drawbacks, a 'Wedge Splitting Test' was developed (Tschegg et al., 1995). In that test, a block of asphalt concrete was made to crack along a predetermined joint at a steady rate. The splitting was done by a wedge that was located in a groove between the two blocks of asphalt. The force and the displacements were recorded during the crack propagation until complete separation of the specimen took place. Based on the shape of the force-displacement curve, a differentiation between brittle and ductile behavior was possible. It was found that with increasing temperature, the plastic behavior of the asphalt increased. There was a decrease in the peak loads with an increase in the temperature. At low temperatures, it was found that the relationship between the force and the crack opening displacement was linear. However, this test could not distinguish between the two different types of tack coats used for that study.

Ameri-Gaznon et al (1990) evaluated the octahedral shear stress (OSS) and the octahedral shear stress ratio (OSR) for different pavement sections. In particular, the OSR and the rut resistance in an asphalt concrete pavement (ACP) overlay were evaluated based on the overlay thickness, interlayer bonding and horizontal surface shear. The properties of the bituminous materials were evaluated using the triaxial test. The cohesion, *c,* and the angle of internal

friction, φ, were determined at 104°F at a loading rate of 4 in./min. The modified ILLIPAVE finite element computer program was used to calculate the OSR's within ACP layers. In the absence of the interlayer bond, the overlay acted independently of the rest of the pavement system allowing greater relative movement in between the two asphalt layers. This reduced the confining stress causing larger OSS in the overlay.

They found that a 4-inch thick overlay was the most critical one when there was free slippage. With increase in the bonding, the critical thickness increased to 6 in. For a complete bond, the stress levels were the highest at the mid height of the ACP overlay. With the loss of bond, the critical stress shifts to the bottom of the surface layer. The stress levels were far more critical than when a complete bond exists. Typically, with increasing the stiffness, it is expected that the shear stresses would decrease. For a poor interlayer bond, the trends were the opposite. The authors also found that the horizontal surface shear force doubled the OSS induced in the ACP overlay for full bond as compared to the no-bond conditions.

Hachiya and Sato (1997) conducted a three-step study. The first step consisted of analyzing the airport runway and taxiway using BISAR to calculate the interface shear stresses and strains. The results showed that shear stresses at interfaces depended on surface layer thickness (thinner layers producing higher shear stresses) and horizontal force on the surface. An increase in the horizontal force, in form of acceleration and braking, caused an increase in the interfacial shear stresses. The pavement failure was caused by interlayer separation due to increased shear and tensile cracking at the bottom of the top layer. Construction of thicker lifts can help reduce the interlayer shear stresses.

In the second step, laboratory tests were conducted on asphalt concrete specimens and emulsions. Asphalt specimens were tested in shear and tension at various temperatures in a

strain-controlled mode. The interfaces were hot jointed, cold jointed, tack coated (0.088 gal/yd^2) and monolithic. Tack coated joints performed better than cold joints but not as well as hot joints or monolithic construction. The interlayer shear strength was dependent on the type of the tack coat used (modified emulsions worked best), rate of application, curing time, and temperature.

In the third part, three sections were constructed and subjected to loading by an assembly similar to aircraft landing gear. The top layer in each of the sections was of the same thickness but constructed differently. The first section was constructed in three lifts, the second in two lifts, and for the third in a single lift. It was observed that the section constructed in a single lift rutted more than the other two. The section least likely to rut was the one with three lifts. Overall, it was suggested to use higher lift thicknesses and modified emulsions to reduce the interlayer slippage on airport pavements.

West et al. (2006) includes a comprehensive synthesis of the different tests developed by researchers around the globe to measure the bond strength between HMA layers. The various devices evaluated in that study fall into three major categories: shear strength tests [ASTRA (Italy), FDOT method (Florida), LPDS method (Swiss), Japan method, Superpave Shear Tester, Leutner test (Germany)], tensile strength tests (ATACKER, Austrian method, Canadian MTQ method) and torsion strength tests (ATACKER).

Eedula and Tandon (2006) used a simple shear device similar to ASTRA Shear Box Apparatus for laboratory evaluation of bond strength in recovered cores. The rate of loading, normal pressure, and temperature have been studied and optimized for measuring bond strength. Sholar et al. (2004) investigated the effect of different tack coat application rates, curing time, types of aggregates, rates of shear and moisture on the interfacial bond strength of composite asphalt specimens. A device, shown in Figure 2.2, was developed to test the specimens in shear.

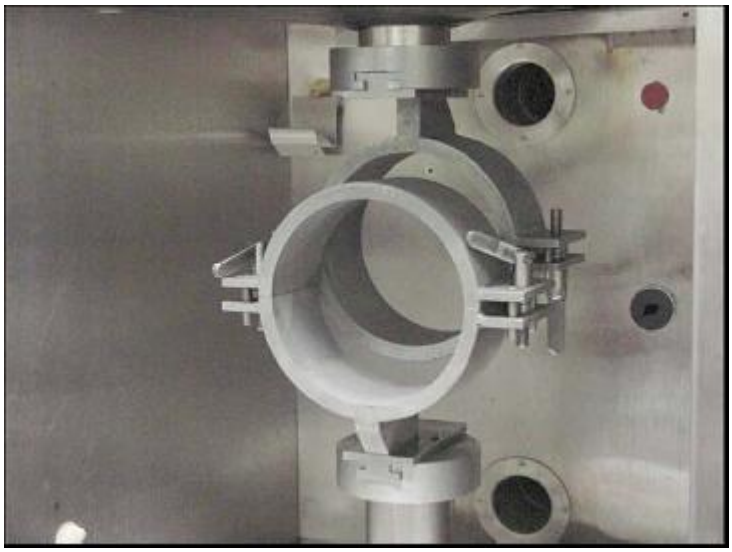

Figure 2.2 – Shearing Setup developed at FDOT (Sholar et al., 2004)

The device was mounted in a temperature controlled MTS test chamber. The shear strengths of composite samples were measured at constant strain rates. The shear strength of the interface was directly related to the rate of shear and inversely to the test temperature. It was observed that exposure of tack coat to moisture, prior to paving a new overlay, caused reduction in the interfacial shear strength. This emphasizes the need to have proper curing of tack coats before paving a new layer. Further, coarser gradations (19.0 mm) performed significantly better than finer (12.5 mm) gradations in terms of shear strengths. In addition, milling of the existing pavement surface before applying tack coat significantly increased the bond strength of the interface in shear. Increasing the rate of application of tack coat caused a marginal increase in the shear strength of the interface.

Mukhtar and Dempsey (1996) conducted tests to evaluate the shear strength of HMA-PCC interface. PCC specimens 2 in. in diameter by 2 in height were cast and cured for a period of 28 days. Subsequently, a tack coat was applied at one of the surfaces and the PCC specimen was inserted in the mold having 2-inch internal diameter. Loose asphalt mix was compacted to a density of 147 pcf in three 1-in. thick lifts. A vertical confining load of 79 psi was applied to

simulate the field condition corresponding to a 2.5-inch thick HMA overlay over PCC. The specimens were then sheared at interface in a strain-controlled mode at the rate of 1, 30 and 300 in./min. The testing was carried out at of 0, 20, 40, 60, 80 and 100 °F. It was observed that, regardless of the testing temperature and shearing rate, monolithic HMA specimens had higher shear strength than specimens jointed at the interface. The shear strength of the interface increased with higher rate of shear and lowering of temperature. Analysis performed by the authors indicated maximum shear stresses below the wheel.

CHAPTER 3

METHODS FOR DETECTING DELAMINATION OF HMA

The desirable method should ideally detect the onset of delamination as soon as possible, as opposed to detecting the problems in its advanced stages. Therefore, an appropriate practical nondestructive tool capable of detecting the potential of delamination or debonding during or shortly after construction is very desirable. Under well executed construction practices, the bond strength between two adjacent layers increases for some time after placement because of the curing of the tack coat. The time to reach the ultimate bond strength is also affected by a number of environmental parameters (such as ambient temperature).

The most common use of the equipment is most likely for the evaluation of the existing pavements, sometimes with unknown construction documentation, for forensic purposes. In this case, the desirable NDT equipment should ideally be able to cover a large area of the airfield in a rapid manner, and should be able to detect the onset of delamination when it is extended over a small area.

A number of NDT technologies have been developed that can be potentially employed for the detection of delamination within HMA layers. Most of these technologies have been used extensively for detecting the delamination in PCC slabs rather than HMA layers. The detection of delamination in PCC is much more straightforward than in the HMA. Some of the difficulties in directly applying successful technologies used for identifying PCC delamination arise from the following:

- concrete slabs are typically placed in thicker lifts than HMA layers,
- the cement paste generates an almost homogenous layer as opposed to the HMA that is essentially a particulate matter (especially for coarser mixes such as SMA),

- the tack coat at the interface of successive HMA layer may act as a weak bonding agent, complicating the detection of debonding,
- changes in temperature play a key role in the measured mechanical properties of HMA layers as well as the adhesion characteristics of tack coat that will affect the results of some of the NDT test.

Table 3.1 contains a list of the NDT technologies which have the potential to detect delamination within HMA layers. The following section provides an overview of these candidate NDT techniques and brief discussion on their advantages, disadvantages, and possible limitations when used for detection of delamination within HMA. More detailed information on these technologies is given in Appendix A. It is recommended that the readers review Appendix A to become familiar with the methods and terminologies discussed below.

The methods can be categorized into five broad groups of Electromagnetic, Impulse, Vibration, Seismic/Sonic and Thermal. A brief description of each method is provided next.

Electromagnetic Methods

Ground Penetrating Radar

The application of GPR in detecting delamination has been found to be questionable. Even at frequencies of 1 to 2 GHz, the GPR wavelengths in asphalt are too long to resolve the thin delamination. Numerical modeling of the GPR signals for the case of delaminated asphalt was carried out by Smith and Scullion (1993). The results indicated that the detection of an air-filled delamination of 0.2 in. or larger water-filled delamination of 0.1 in. and larger at a minimum depth of 2 in. may be detected using a 2.5 GHz GPR antenna. The maximum speed for data acquisition suggested was 10 mph.

Table 3.1 – List of Feasible Technologies for Detecting Delamination of HMA Layers

Method	Device	Advantages	Concerns
Electro-magnetic	GPR	Rapid test, provides full areal coverage	Cannot directly detect delamination even at 1 or 2 GHz
Impulse	FWD	Available and well understood, rapid test	Impulse duration too long to focus on top thin layers, variability in thickness and modulus of sublayers may mask the detection of delamination
	LWD	Easier to perform tests than FWD	
	Impulse Response	Have been successful to detect different levels of debonding in HMA, rapid test, needed components are readily available	Even though automated analysis available, automated equipment is not available
Vibration	Stiffness Gauge	Input load is controlled, equipment available	Coupling to HMA problematic, load is too light, frequency range is too low
	High-frequency Sweep	Reasonably priced equipment is available for other applications	Automation may be required, has not been used on HMA
Seismic/ Sonic	Impact-Echo	Proven technology for detection of delamination in concrete, automated equipment is available	Limited use for detecting HMA delamination, coupling of energy to coarser mixes
	SASW	automated equipment is available, feasibility has been shown in HMA	Coupling of energy to coarser mixes, thinner top layers
	Ultrasound	Proven technology for detection of delamination in concrete, automated equipment is available	Has not been used on HMA, frequency content may be too high that interact with coarse aggregates
Thermal	Thermography	Rapid test, provides full areal coverage, automated equipment and interpretation	Highly dependent on environmental conditions such as wind speed, ambient temperature, and sunlight, can only be used to detect very shallow delamination

Based on other field investigations, the GPR survey may provide useful information which may indicate delamination between asphalt layers. For example, the much larger amplitudes in GPR radargrams mark the location of delaminated zones.

Impulse Methods

Falling Weight Deflectometer (FWD)

A number of studies have been carried out to assess the suitability of the FWD for assessing the delamination of HMA layers. Intuitively, higher deflections are expected, if poor bond between asphalt layers exists. A new backcalculation process for assessing the bond condition between the HMA layers using FWD deflections has shown some promising results (Al Hakim, 1998). The backcalculated parameter in that process is a parameter called the interface stiffness (see Appendix A for definition). In the same study, the backcalculated interface stiffness from FWD deflection basins was found not to be successful for assessing of bond condition between thin HMA layers.

Other studies have compared the slippage susceptibility at asphalt interfaces with FWD measurements. A Tack Coat Failure Ratio (TFR) was defined as the ratio of the moduli of the HMA layers above and below the debonded interface measured form FWD. TFR compared well with the slippage susceptibility at the interfaces as defined in Gomba (2004). However, given the uncertainty in backcalculating the moduli of thin HMA layers, this observation may need further evaluation.

Other approaches have been carried out based on the "area" concept (a deflection basin curvature index), that calculates the overall composite modulus of the entire pavement structure (Hammonds et al., 2005). This process is described in Appendix A. The approach can be used effectively to approximate the relative stiffness of the uppermost bound layer(s) in a pavement

for comparative purposes. However, this is an empirical approach and has not been calibrated with FWD measurements.

Light Weight Deflectometer (LWD)

After an extensive review of the literature, no cases have been found that the LWD was used for detecting delamination. In general, the LWD is likely not suitable for the detection of delamination in real world applications because of the long duration of impulse and the limitations of sensor locations.

Impulse Response (IR) Method

In principle, the IR method is very similar to the LWD tests. The main difference is the higher ranges of frequencies excited in the IR method (several kilohertz for IR vs. less than 100 Hz for LWD). The IR method has shown promise as a quantitative and qualitative tool to obtain information about the interface bond between HMA interfaces. In the IR method, the bond condition is estimated from a parameter defined as Transfer Function Estimate (TFE). This parameter is obtained from the variation of the ratio of deflection measured with a geophone or an accelerometer and measured load imparted to the pavement with frequency. Different TFE values were attributed to different bonding condition (Kruntcheva et al., 2005).

Other approaches have focused on the fractal theory as a quantitative indicator of bond conditions. As reflected in Appendix A, in these studies it was feasible to determine ranges from well bonded areas to de-bonded areas of asphalt pavements (Sangiorgi et al., 2003). However, the differences in the values between the bonded and debonded conditions for pavements with thin structures are small.

Vibration Methods

Stiffness Gauge

The stiffness gauge imparts very small energy in the range of 100 to 200 Hz. Since the stiffness gauge is optimized for low-stiffness geo-materials, neither the force level nor the frequency range seems adequate for detecting delamination. A French study (Lepert et al., 1992) has shown that this technique may not be effective even when used in controlled experimental study test sections with different interface conditions

High Frequency Sweep

The high-intensity, high-frequency vibration generated by high frequency sweep devices primarily excites the pavement layer on top the delaminated layer. The resulting variation in stiffness with frequency for this method may be used to detect delamination but this method has not been proved in the field. This method has not been implemented for the detection of HMA delamination before.

Sonic/Ultrasonic/Seismic Methods

Impact Echo

This method has been effective in the detection of HMA delamination deeper than 4 in. (Armitage et al., 2000). When delamination occurs at depths less than 4 in., it is still possible to detect the existence of the delamination; however, no information regarding the depth to the delaminated layer can be drawn. A detailed description of the method is provided in Appendix A.

Ultrasonic Surface Waves

This method can be use not only to detect delamination but also identify the approximate depth of the debonded layers. In this method, the variation in the velocity with wavelength is

measured to generate a so-called dispersion curve (see Appendix A). The wavelength at which the phase velocity is no longer constant is closely related to the thickness of the top layer (Nazarian et al., 1997). For two layers with similar modulus bonded together, the variation in modulus with wavelength is more or less constant. However, when the two layers are debonded, the modulus will decrease significantly with wavelength below the interface of the two layers. This method has been successfully used in some forensic studies to detect HMA stripping (Hammons et al., 2005).

Some devices can automatically conduct the IE and SASW tests simultaneously and in a rapid manner.

Ultrasound

This method consists of generating a short ultrasonic impulse by a transmitting transducer, and recording the response through the material with up to 56 receivers. The depth of the defect is determined on the basis of the travel time of the impulse and the ultrasonic wave velocity. This method has proven to be effective in flaw detection mainly in concrete material (Garbacz and Garboczi, 2003). However, no research has been carried out to detect asphalt delamination.

Thermal Methods

Infrared Thermography

Infrared thermography (IR) is a diagnostic NDE method which relates changes in surface temperature of a material to subsurface or internal flaws. On existing pavements, the IR technology can be used to relate local temperature gradients to the presence of shallow subsurface flaws in HMA. It is believed that the trapped air in a delamination or cracked zone acts as an insulator blocking the heat transfer between the HMA lifts above and below the

delaminated interface. Consequently, the surface of the pavement over the delaminated area exhibits a temperature gradient (negative at night and positive during the day) with respect to its surrounding fully bonded area (Moropoulou et al., 2002). This method depends on environment and climate conditions and daytime.

Some promising results in terms of detecting shallow delamination (2 to 3 in.) in HMA using IR are reported by Tsubokawa et al. (2007). However, some unfavorable results are also reported by Hammons et al. (2005). No information regarding depth at which delamination occurs can be obtained with this method.

Assessment of Methods for Detecting Delamination

A number of parameters should be assessed to ensure that the methods can detect the delamination of HMA layers in an accurate, repeatable and practical manner. The factors considered in this study consist of the following:

- Detectability threshold
- Speed of data collection and coverage
- Speed of data analysis and interpretation
- Availability of commercial equipment
- Expertise needed for data processing and data interpretation
- Equipment reliability
- Past experience with the method for detecting delamination of HMA
- Ability to implement procedures without Specialists

The assessment of these factors for the NDT methods included in Table 3.1 is summarized in Table 3.2 and the rational beyond this assessment is described below.

Detectability Extent

The detectability extent is defined as the planar extent of debonding that should occur before they can be detected by the method. Two levels of detectability extent are used (localized and extensive). "Localized debonding" refers to small areas (say less than 3 ft in dimensions) where "extensive debonding" refers to when a large area of the airfield is debonded. Intuitively, the methods that can detect the smaller defects are more desirable. However, this factor should be viewed in conjunction with the detectability threshold and whether the data is collected continuously or the tests are spot tests as discussed below.

In general, the Vibration and Seismic/ Sonic methods are capable of detecting smaller defected areas since they are localized tests. Depending on the speed of operation, the GPR can also detect localized defects.

Detectability Threshold

The detectability threshold is defined as the stage at which the delamination can be detected by the method. Two levels of detectability threshold are used (onset and advanced). The onset of delamination is defined as when the two layers are debonded but they are still in contact, whereas the advanced stage is defined as when the two layers are significantly separated due to the intrusion of moisture or the deterioration of the HMA layers at the boundary of the layers.

Impulse response, Impact Echo and SASW methods require only separation of the layers to detect the debonding. GPR at least theoretically requires either 0.2 in. of separation between the adjacent layers to detect the separation of the reflected waves from the top and bottom of the separated layers.

Speed of Data Collection and Coverage

The GPR and thermography method collect data in a continuous manner, whereas the other methods are all spot measurements. The rates of production of the methods that collect data at discrete points are similar and between 25 to 40 points/hr.

Speed of Data Analysis

The data analysis is defined as processing the raw data collected by the device into either a single parameter or a graphical output. For almost all methods, the data analysis is quite rapid and in most cases the results are available for inspection in the field.

Expertise Needed for Data Processing and Data Interpretation

Data processing and interpretation is defined as locating the locations of debonded areas from the analyzed data. This includes filtering the analyzed data and delineating the anomalies detected into the debonding of the layers.

None of the methods are currently perceived to be easy to interpret without adequate training. The GPR and the Impulse Response methods may require higher levels of expertise than the others for this purpose.

Availability of Equipment

For almost all methods, off-the-shelf equipment is available that can be purchased.

Reliability of Equipment

The reliability of the equipment is defined as the ruggedness of the equipment in terms of day-to-day production and the feasibility of using the equipment under different environmental and real-world conditions. Most of the devices proposed in Table 3.2 have been evaluated for reliability of the operation, and for the most part demonstrated their reliability. The

Table 3.2 – Advantages, Disadvantages and Potential Use of Feasible Methods

Method	Device	Equipment Limitations and Capabilities							Past Experience	Ability to implement procedures/ equipment without Specialists
		Detectability Extent	Detectability Threshold	Speed of Data Collection and Area Coverage	Speed of Data Analysis	Availability and accessibility of equipment	Expertise Needed for Data Processing and Interpretation	Equipment Reliability		
Electro-magnetic	GPR	Small	Advanced	Rapid/ Continuous	Slow	Commercially Available	High	High	Mixed Results	Medium
Impulse	FWD	Extensive	Advanced	5 min./ point	Rapid	Commercially Available	High	High	Mixed Results	Medium
	LWD	Small		2 min./ point	Rapid	Commercially Available	Unknown	Medium	None	Medium
	Impulse Response	Small	Onset	2 min./ point	Rapid	Commercially Available	High	High	Some	High
Vibration	Stiffness Gauge	Unknown	Unknown	2 min./ point	Unknown	Commercially Available	Unknown	High	None	Unknown
	High-frequency Sweep	Unknown	Onset	Unknown	Unknown	Research Stage	Unknown	Unknown	None	Unknown
Seismic/ Sonic	Impact-Echo	Small	Onset	2 min./ point	Rapid	Commercially Available	Medium	High	Some	High
	SASW	Small	Advanced	2 min./ point	Rapid	Commercially Available	Medium	High	Some	High
	Ultrasound	Unknown	Unknown	2 min./ point	Unknown	Commercially Available	Unknown	High	None	Unknown
Thermal	Thermography	Extensive	Advanced	Rapid/ Continuous	Rapid	Commercially Available	Medium	Medium	Mixed Results	Low

thermography has been ranked medium because favorable environmental conditions are needed for its use.

Past Experience with the Method for Detecting Delamination of HMA

Based on the literature survey and the experience of the research team, the outcome of past experience of organizations that have attempted these tests are summarized to either "mixed results," "some," and "none." "Mixed results" refers to the cases when different organizations have reported both favorable and unfavorable experience with detecting debonding of HMA for a given method. "Some" refers that the experience with the method has been positive but the number of studies are limited to draw a definite conclusion. A number of methods ranked as "None" signifies that they have never been used to detect delamination of HMA layers.

Ability to Implement Procedures without Specialists

The ability of utilizing these methods by technicians routinely without the need for specialists is also considered. This factor is important for organizations that prefer not to outsource their pavement evaluation program. For the most part, the data collection can be carried out by the technicians. However, the data interpretations may need different levels of expertise. The thermography requires specialized equipment and interpretations that, at least in the near future may require specialists for data collection and analysis. The GPR still requires experts to interpret the data. The methods with the highest chance of being implemented in-house are the impulse response, impact-echo and SASW. However, even these methods require appropriate training for a conscientious technician or engineer.

Based on the qualitative information provided in Table 3.2, the methods were ranked in a quantitative manner as shown in Table 3.3. The ranking is based on a utility analysis considering

Table 3.3 – Evaluation of NDT Methods

Method	Device	Evaluation Category							Total	Categorizing Methods by Tier
		Applicability to Delamination Detection and Limitations/ Restrictions of Test Equipment	Accuracy and Repeatability of Test Results	Equipment State of Development	Time Required for Data Analysis	Production Rate, Time Required for Testing	Initial Cost and Maintenance/ Operational Cost of Test Equipment	Data Collection Guidelines and Data Presentation		
Utility Weight		**0.25**	**0.25**	**0.1**	**0.15**	**0.1**	**0.1**	**0.05**	**1.00**	
Electro-magnetic	GPR	3	3	5	5	5	1	5	3.6	**1**
Impulse	FWD	1	3	5	3	3	3	3	2.7	**2**
	LWD	1	3	3	3	3	5	3	2.7	**2**
	Impulse Response	3	5	3	5	3	3	3	3.8	**1**
Vibration	Stiffness Gauge	1	1	3	3	3	5	1	2.1	**3**
	High-frequency Sweep	3	1	3	3	3	3	3	2.5	**3**
Seismic/ Sonic	Impact-Echo	3	5	5	5	3	3	3	4.0	**1**
	SASW	3	5	5	5	3	3	3	4.0	**1**
	Ultrasound	3	3	3	3	3	3	3	3.0	**2**
Thermal	Thermography	3	3	5	3	5	1	3	3.2	**2**

several parameters with different weighting factors. The following parameters were selected for ranking in the order of importance:

1. Applicability to Delamination Detection and Limitations/Restrictions of Test Equipment
2. Accuracy and Repeatability of Test Results
3. Time Required for Data Analysis
4. Equipment State of Development
5. Production Rate
6. Time Required for Testing
7. Initial Equipment Cost and Maintenance/Operational Cost of Test Equipment
8. Data Collection Guidelines and Data Presentation

The first two parameters were given higher weights of 0.25 out of 1 since they are the most important factors in deciding whether a method is appropriate or not. Time required for analysis was weighted slightly higher than other parameters since the timely delivery of results deemed important. The data collection guidelines and data presentation is rather important but they were not deemed as important as other practical items enumerated under items 4 through 7.

Each of the eight criteria listed above was ranked either 1 (low), 3 (average) or 5 (high). The weighted averages of the individual rankings were used to categorize the methods into the following three tiers:

- Tier 1, which includes GPR, Impulse Response, Impact echo and SASW, seems to have the best chance to provide a practical solution to the detection of delamination. Based on the research team's experience and others, these four tests may have the highest probability of success.

- Tier 2, which consists of Ultrasound, thermography and FWD/LWD, are either not used before or has not always proven effective.
- Tier 3 methods consist of the stiffness gauge and high-frequency sweep. These methods have not been used for the delamination detection before and the research team has concerns with their probability of success.

Based on this analysis, the focus of evaluation was shifted on the tier 1, and to lesser extend tier 2 and tier 3 methods.

CHAPTER 4

CONSTRUCTION OF CONTROL PAVEMENT SECTION

The construction of a pavement section to evaluate all NDT methods is detailed in this chapter. Several laboratory tests that were conducted to identify and evaluate debonding agents are described first. Then, the construction of the pavement section is detailed. Three levels of debonding between two layers of HMA, ranging from bonded to partially-bonded to fully-debonded, were replicated. In addition, a case of extremely severe debonding of HMA was also reproduced.

Laboratory Tests to Determine Suitability of Debonding Agents

Two local HMA mixes that met the Federal Aviation Administration (FAA) specifications were considered. One mix met the requirements of Item P-401 (Plant Mix Bituminous Pavements) and the other Item P-403 (Base, Leveling or Surface Course). The job mix formulas of these two mixes are included in Appendix B.

To establish the suitability of different materials to be used as debonding agents, a series of laboratory tests were conducted. Kruntcheva et al. (2004) recommended clay slurry and talcum powder to reproduce partial and full debonding between two lifts, respectively. In addition to these agents, grease and thin paper soaked in motor oil were considered. A tack coat in compliance with Item P-603 at a rate of 0.14 g/yd^2 (0.7 lit/m^2) was also used as control bonding agent. Direct shear tests were performed to assess the bond strength.

The process of preparation of the specimens is shown in Figure 4.1. After several iterations, the following steps were followed:

- Compacting a bottom lift using a gyratory compactor to a relative density of about 90%
- Applying a bonding agent (Figures 4.1a and 4.1b)

- Compacting the top lift using 75 blows of a Marshall Hammer according to ASTM D6926-04 (Figure 4.1c)

The specimens were approximately 4 in. (100 mm) in diameter and 4.2 in. (105 mm) in height (Figure 4.1d).

a) Tack Coat

b) Clay Slurry

c) Marshall Compaction

d) Final Specimens

Figure 4.1 – Preparation of Laboratory Specimens and Specimens Ready for Shear Tests

The shear device used in this study is shown in Figure 4.2. The bottom lift of the specimen was trimmed so the interface between the top and bottom lifts of the specimen precisely matched with the interface of the top and bottom plates of the direct shear device. The

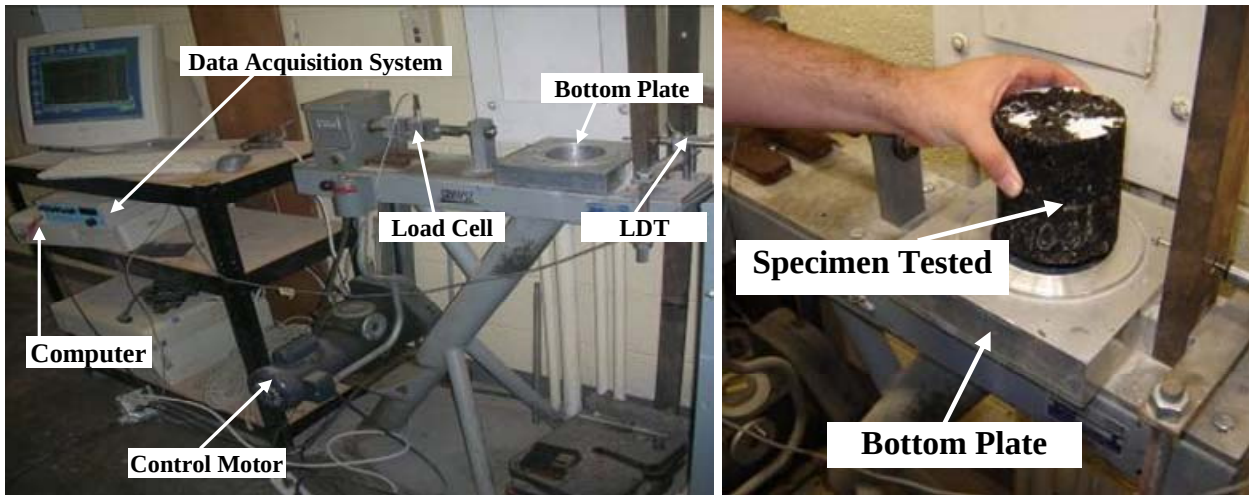

Figure 4.2 – Schematic of Shear Apparatus

specimen was sheared at a constant rate of 0.05 in./min (1.3 mm/min, see Figure 4.3) after a vertical load of 50 lbs was applied to the specimen. All tests were conducted at laboratory temperature of 72°F (22°C). A load cell attached to the system measured the load applied at any moment, while a linear displacement transducer (LDT) measured the displacement between the top and bottom lifts. Figure 4.4 illustrates typical shear forces measured with tack coat and talcum powder as bonding agents. The shear strength is simply the maximum force measured divided by the area of the specimen. The shear strengths measured for each bonding agent are presented in Table 4.1. Two sets of specimens were prepared. One set consisted of the P-403 mix as the bottom lift and the P-401 mix as the top lift. The other set comprised of two lifts of the P-401 mix. Three to seven replicate specimens were prepared for each debonding agent. For both sets of specimens, the highest bond strengths were associated with the tack coat (about 33 psi, 220 kPa), and the lowest with a thin paper soaked in motor oil (about 5 psi, 35 kPa). The coefficients of variation (COVs) of the results are rather high for most bonding agents. Aside from experimental errors, the shear resistance from aggregate interaction might explain the high COVs of these results.

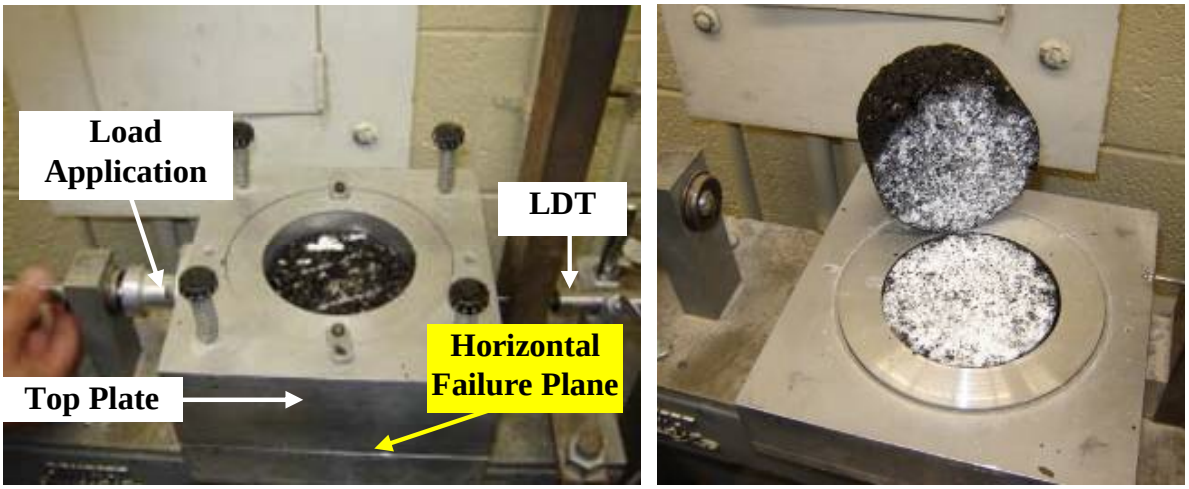

Figure 4.3 – Detail of Asphalt Sample Placement on Shear Device

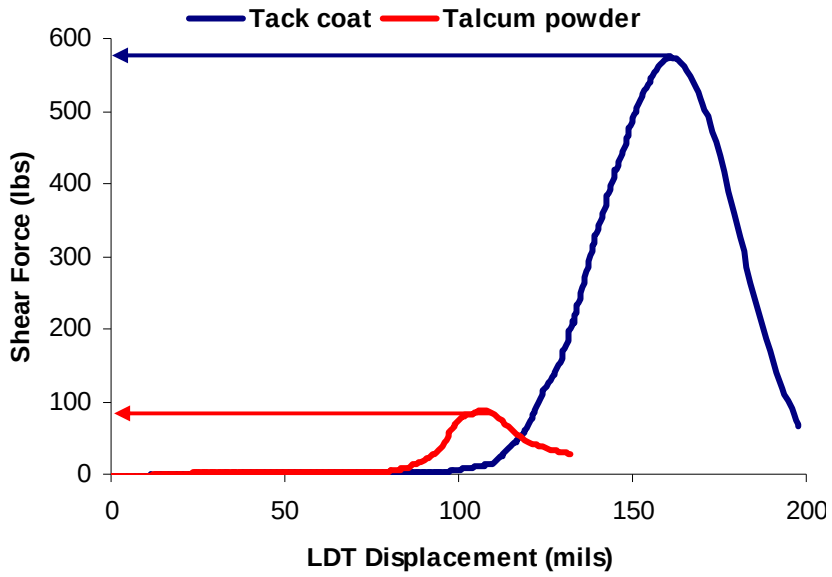

Figure 4.4 – Test Output from Shear Device

The debonding agents used in the construction of the pavement section are summarized in Table 4.2. In addition to the proposed materials, a severe debonding was reproduced by placing a piece of thick corrugated cardboard in selected areas.

Table 4.1 – Shear Strengths (in psi) for Laboratory Prepared Specimens

Sample Condition	P-401/P-401 Mixes					P-403/P-401 Mixes			
	Tack Coat	Talcum Powder	Clay Slurry	Grease	Paper Soaked in Motor Oil	Tack Coat	Talcum Powder	Clay Slurry	Paper Soaked in Motor Oil
Average*	35	20	22	19	5	32	17	27	5
COV	36%	51%	75%	19%	34%	24%	5%	19%	47%

** of three to seven specimens*

Table 4.2 – Summary of Debonding Agents Considered for the Controlled Study

Partial Debonding	Full Debonding	Control Bonding	Severe Debonding
Clay Slurry	Paper Soaked in Motor Oil	Regular Amount of Tack Coat as per FAA Item P-603	Cardboard between Layers
Talcum Powder			
Grease			

Construction of Test Section

Details on the construction of the test section can be found in Appendix C. Ten different sections were constructed in a vacant lot within UTEP property, as shown in Figure 4.5. The final layout of the sections is depicted in Figure 4.6. Each section was 9 ft long (2.7 m) by 10 ft (3 m) wide. Three transition zones were incorporated [a 10 ft (3 m) section before Section 1, a 15 ft (4.6 m) section between Sections 5 and 6 and a 10 ft (3 m) section beyond Section 10] to minimize the variability of the laid down mix during construction.

The nominal pavement cross-section for all sections consisted of a prepared sandy-silt subgrade and about 8 in. (200 mm) of HMA placed in three lifts. The first two lifts of the HMA were the same for all sections. The bottom lift consisted of about 3 in. (75 mm) of a P-403 mix

and the middle lift 2.5 in. (63 mm) of a P-401 mix. The top lift of Sections 1 through 5 consisted of a coarse mix (P-403 mix) and Sections 6 through 10 a fine mix (P-401 mix).

Figure 4.5 – Location of Asphalt Section at UTEP Facilities

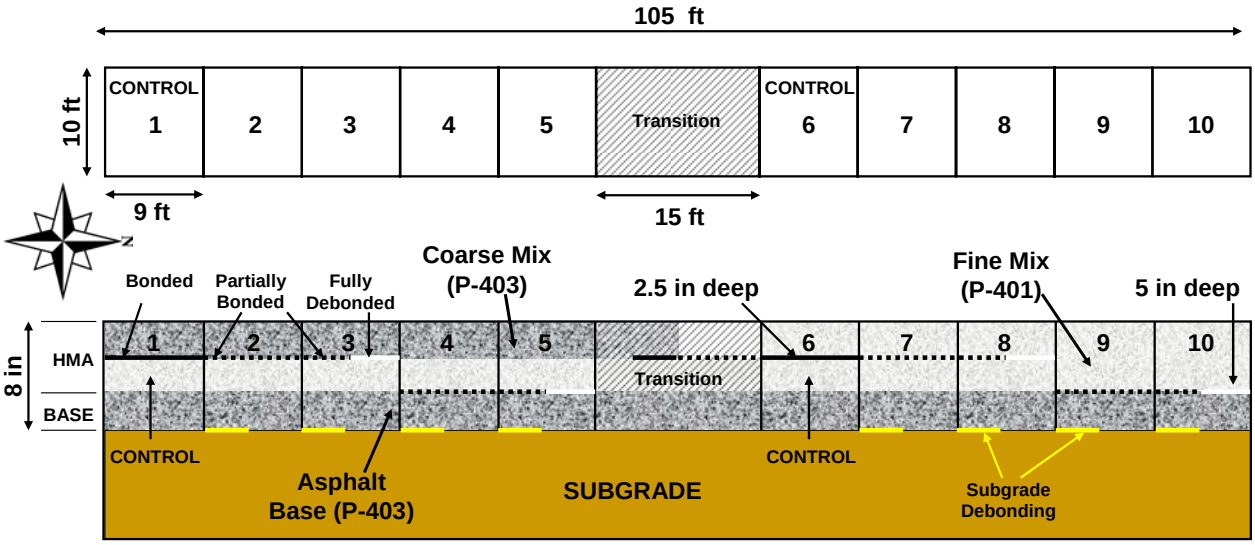

Figure 4.6 – Schematic of Controlled Section

A typical plan view of each section is depicted in Figure 4.7. The characteristics of the sections are summarized in Table 4.3. In general, a 4 ft (1.2 m) by 9 ft (3 m) area for each

section was debonded. In addition, smaller debonded areas were constructed to test the detectability threshold of the methods.

Details measurements for each point are included in Appendix C. Seismic moduli obtained with the PSPA on top of the second lift are presented in Figure 4.8. The surface temperature (T) was measured with a laser gun. The values presented were converted to a reference temperature of 77ºF using (Li and Nazarian, 1994):

$$Modulus_{77F} = \frac{Modulus_T}{(-0.00307 * T + 1.2627)} \tag{4.1}$$

The average PSPA modulus (converted to the reference temperature) of the second lift was 1733 ksi (12 GPa) and the average composite modulus of the first and second lift was 1791 ksi (12.3 GPa). The same points were tested 24 hr after the completion of the third lift (see Figure 4.9). The average modulus of the top lift was 2047 ksi (14 GPa) and the average composite modulus of the three lifts was 1753 ksi (12 GPa).

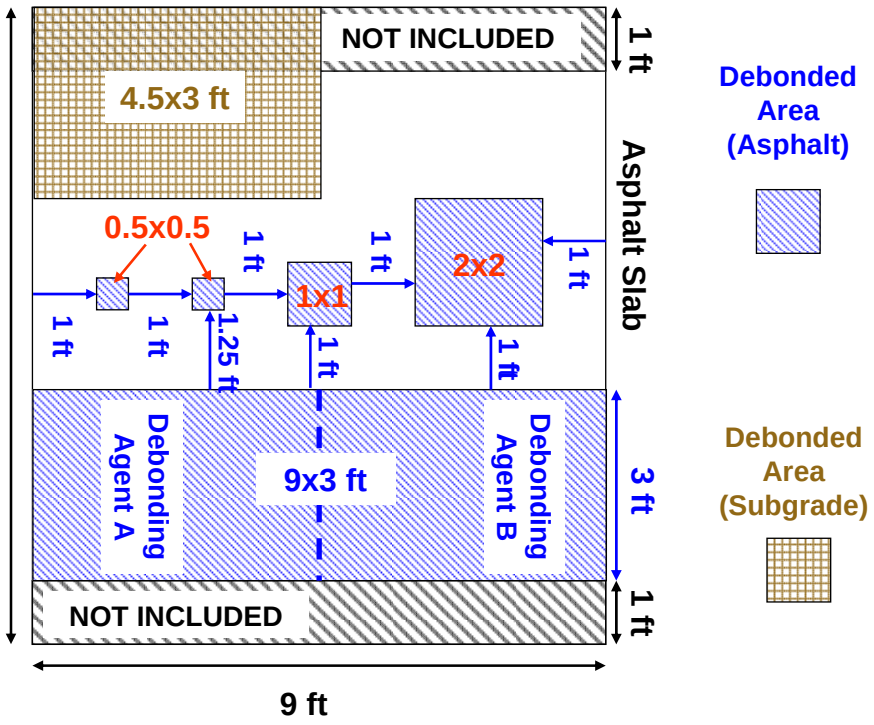

Figure 4.7 – Typical Layout for Partially and Fully Debonded Areas

Table 4.3 – Characteristics of Sections Used in This Study

Section	Surface Mix	Designation	Debonding Agent				
			Tack Coat	Grease (Agent A)	Clay Slurry (Agent B)	Talcum Powder (Agent A)	Paper with Oil (Agent B)
1	Coarse Mix	Control	√				
2		Shallow Partially-Debonded		√	√		
3		Shallow Fully-Debonded				√*	√
4		Deep Partially-Debonded		√	√		
5		Deep Fully-Debonded				√*	√
6	Fine Mix	Control	√				
7		Shallow Partially-Debonded		√	√		
8		Shallow Fully-Debonded				√*	√
9		Deep Partially-Debonded		√	√		
10		Deep Fully-Debonded				√*	√

** Partially-Debonded*

The NDG was used at 33 locations on the surface of the HMA. The variation in the relative density along the section is in Figure 4.10. Densities measured with the NDG are detailed in Appendix C. The average relative density was about 95%.

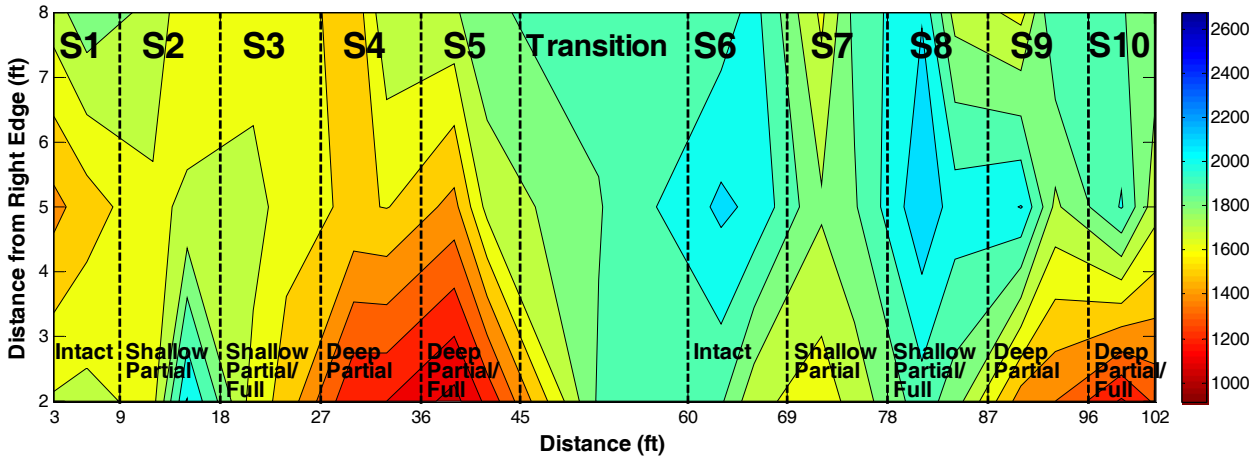

a) Lifts 1 and 2 Combined

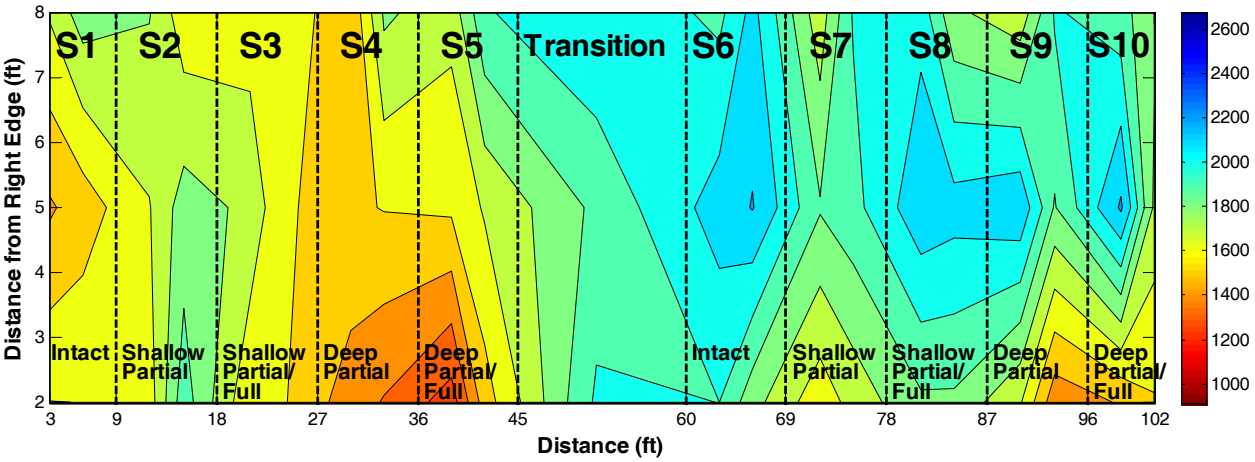

b) Second Lift

Figure 4.8 – PSPA Results after Second Day of Construction

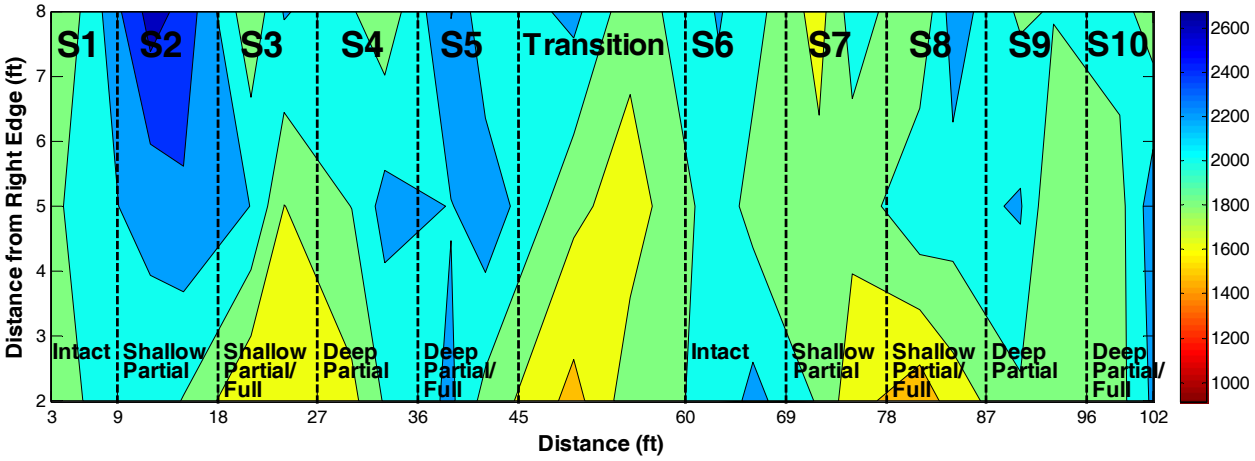

Figure 4.9 – PSPA Results for Top Lift after Completion of Construction

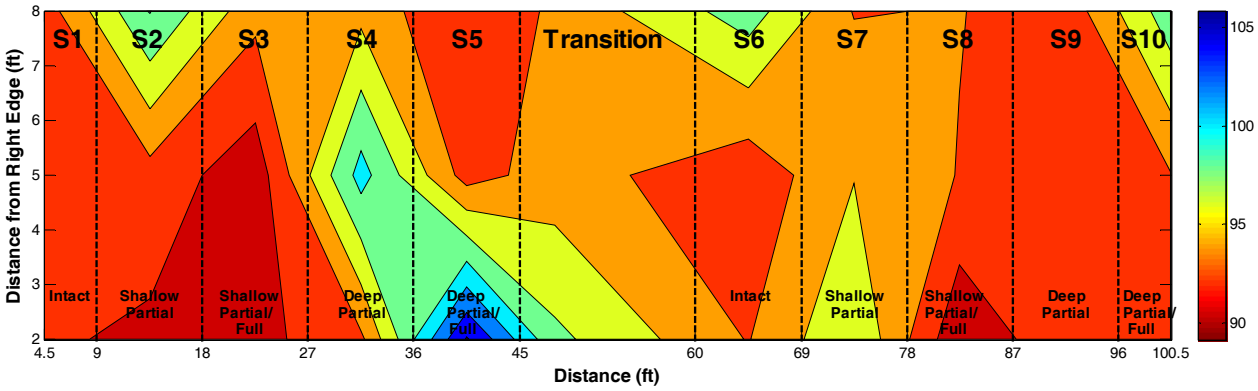

Figure 4.10 – Variation of Percentage of Marshall Density on Controlled Study

CHAPTER 5

PRELIMINARY EVALUATION OF NDT METHODS

The preliminary evaluation with several NDT methods on the control pavement section is included in this chapter. Table 5.1 contains a list of NDT technologies employed for the detection of debonding within HMA layers. These NDT methods are extensively described in Appendix A. As such, only the results with each one will be presented in this chapter.

Table 5.1 – List of NDT Technologies Used on the Controlled Study

Method / Device									
Electro-magnetic	**Impulse**			**Vibration**		**Seismic/Sonic**			**Thermal**
Ground Penetrating Radar (GPR)	Falling Weight Deflectometer (FWD)	Light Weight Deflectometer (LWD)	Impulse Response (IR)	Stiffness Gauge (SG)	High Frequency Sweep (HFS)	Impact Echo (IE)	Ultrasonic Surface Waves (USW)	Ultrasound (US)	Thermal Imaging (TI)

Location of Test Points

As shown in Figure 5.1, 25 points were evaluated on every section. The transversal spacing between lines varied, but the longitudinal spacing was fixed at 2 ft (0.6 m). The same number of lines was maintained on the transition section (between Sections 5 and 6). The number of points was increased to 8 with the same spacing. Preliminary core locations are also included in the figure.

Sonic/Ultrasonic Seismic Methods

Impact-Echo (IE) and Ultrasonic Surface Waves (USW)

A Portable Seismic Pavement Analyzer (PSPA) was used to conduct these two tests simultaneously. As shown in Figure 5.2, the PSPA consists of an automatic source and two receivers. A test and the field analysis would take about 15 seconds.

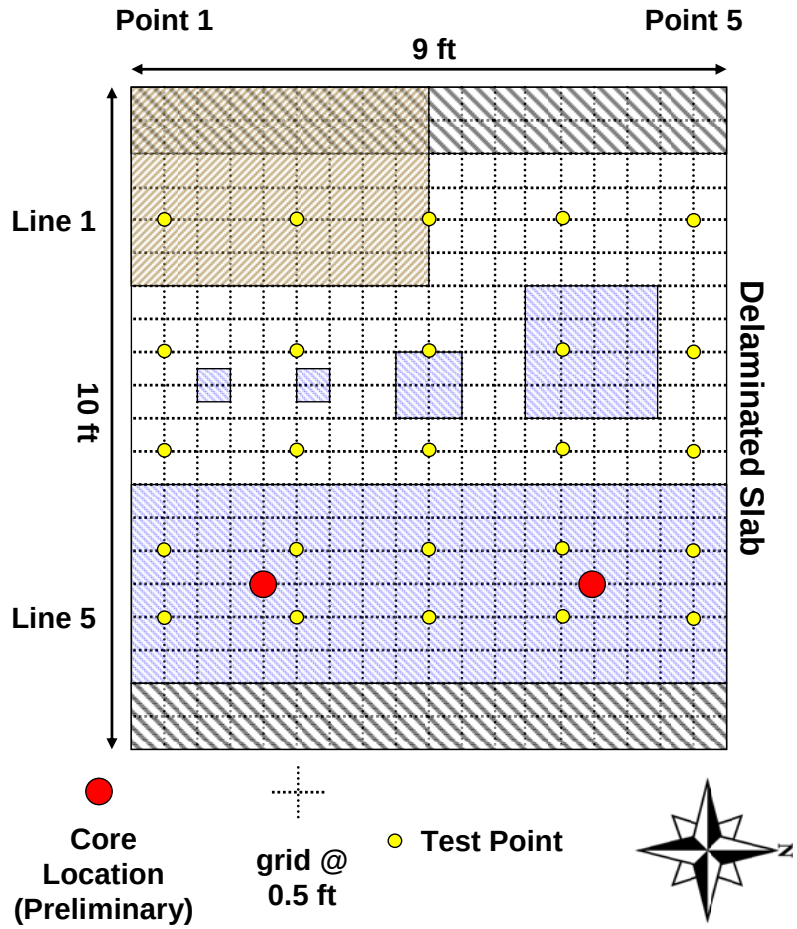

Figure 5.1 – Location of Test Points for a Given Section

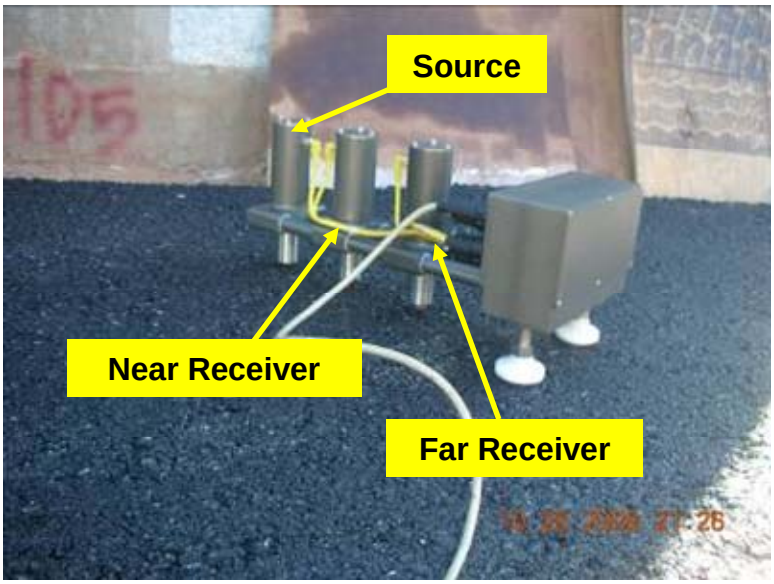

Figure 5.2 – PSPA Detail

Examples of typical voltage outputs of the three PSPA sensors as seen by the operator in the field are shown in Figure 5.3 for an intact and a severely debonded area. The time records from the two receivers (the black and green traces) are appreciably different from the two tests. The pulses are wider for the debonded record, and the minima of the two records from the intact areas are closer to one another than the ones from the damaged area.

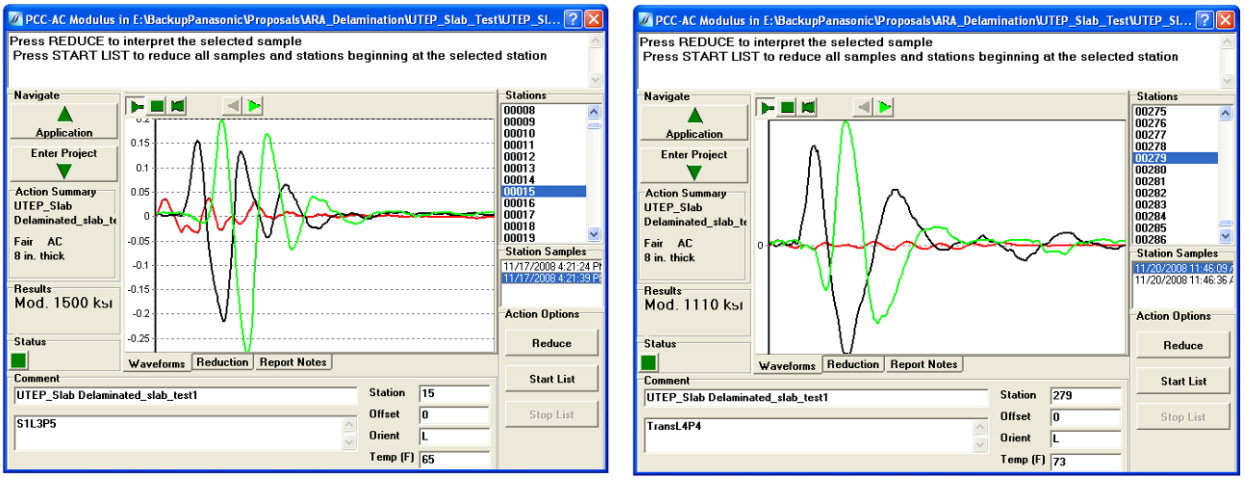

a) Intact **b) Severe Debonding**

Figure 5.3 – Time Records Results with PSPA on Controlled Study

Ultrasonic Surface Waves (USW) Results

The USW analysis page as seen by the operator in the field is shown in Figure 5.4 for the time records shown in Figure 5.3. The top graphs demonstrate the variation in modulus with wavelength (called dispersion curves). The dispersion curve for the intact area is fairly uniform; whereas for the damaged point a sharp decrease in modulus below a wavelength of 2.5 in. (63 mm, the location of the damage) is evident.

The vertical red lines in the graphs demonstrate the average moduli of the HMA layer from close to surface (1 in., 25 mm) to 8 in. (200 mm, nominal thickness of the layer). As reflected in the left hand side of the two graphs, these average moduli are about 1500 ksi (10 GPa) for the intact and 1130 ksi (7.8 GPa) for the damaged areas.

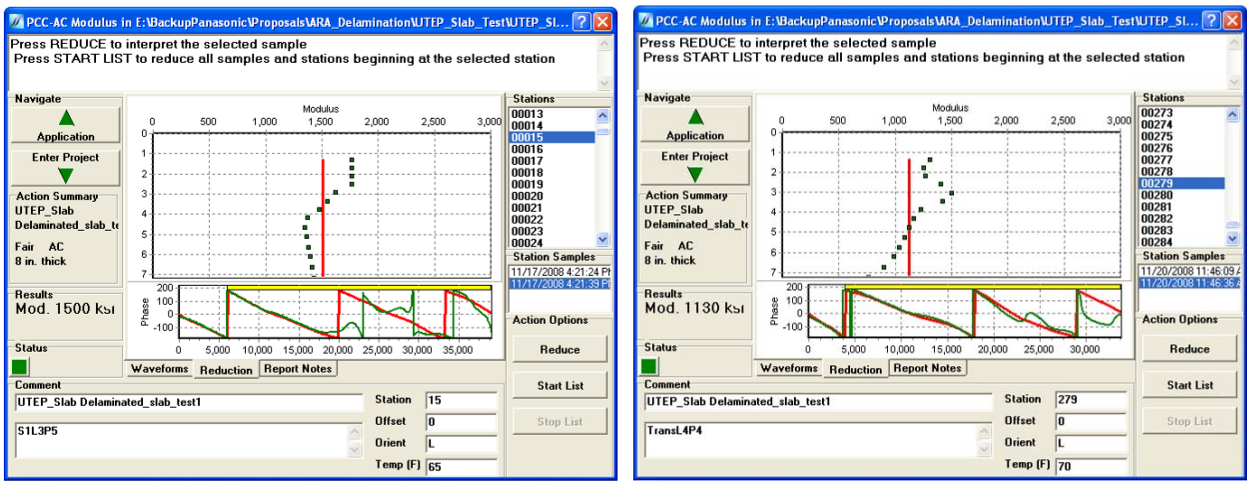

a) Intact **b) Severe Debonding**

Figure 5.4 – Dispersion Curve Results with PSPA on Controlled Study

The variation in the average moduli along the ten sections is shown in Figure 5.5. Moduli were adjusted for temperature using Equation 4.1. For the benefit of the readers, the figure is color-coded. The definition of each color is included in Table 5.2. The average and standard deviation of each control section (1 and 6) were used as reference. In Figure 5.5a that corresponds to the coarse surface mix, an area from the right hand side of Section 2 until the end of Section 5 generally exhibits lower moduli as anticipated. However, parts of Sections 2 and 4, both located on partially debonded sections, exhibit normal moduli. Similar trends are observed for the fine surface HMA sections (Figure 5.5b). However, in these sections the deep debonding is not as well defined as for the similar sections with coarse surface HMA.

The average moduli for the top 2.5 in. (63 mm) of the ten sections are shown in Figure 5.6a. Some indication of debonding is observed on the prepared damaged areas, particularly for Sections 3 and 5 (coarse mixes). On the sections prepared with fine mix, the reduction of modulus is smaller on the debonded areas. For the transition area, similar findings are obtained as detailed in Appendix D. When the overall thickness of 8 in. (200 mm) was considered, the

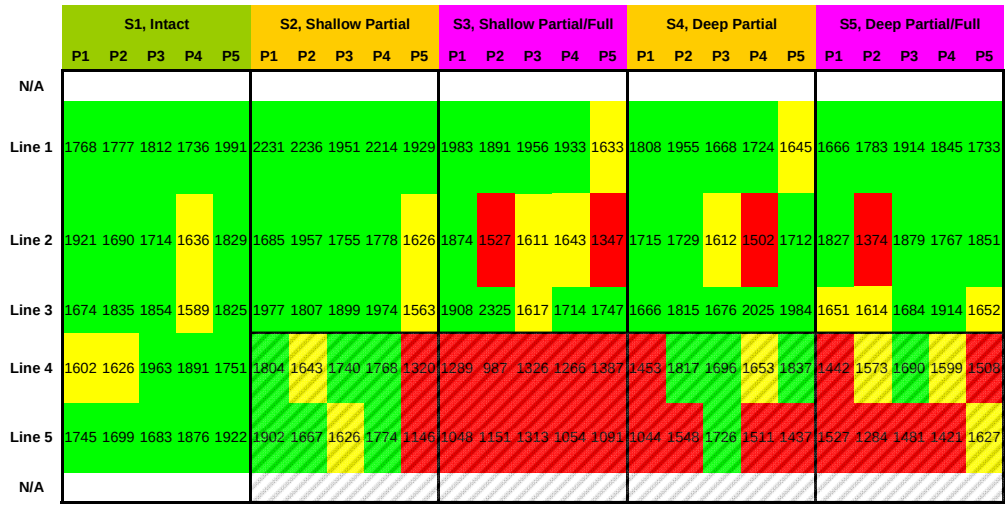

a) Sections 1 to 5

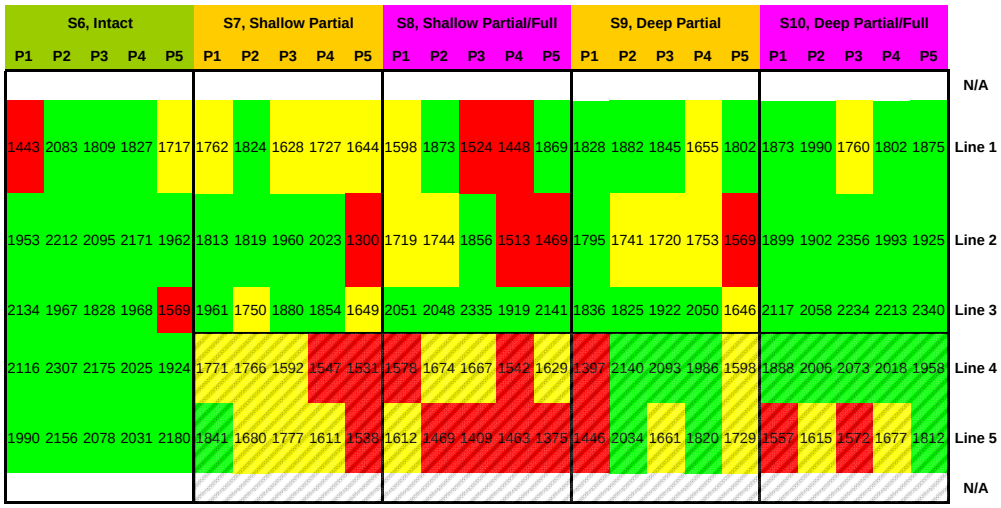

b) Sections 6 to 10

Figure 5.5 – Statistical Analysis of PSPA Modulus on Controlled Study

Table 5.2 – Criteria Used to Analyze Moduli on Controlled Study

Color Code	Modulus Value	Interpretation
Green	$E > E_{control} - \sigma_{control}$	Measured modulus is similar or higher than modulus from control section
Yellow	$E_{control} - \sigma_{control} > E > E_{control} - 2\,\sigma_{control}$	Measured modulus is somewhat less than control modulus
Red	$E < E_{control} - 2\,\sigma_{control}$	Measured modulus is substantially less than control modulus

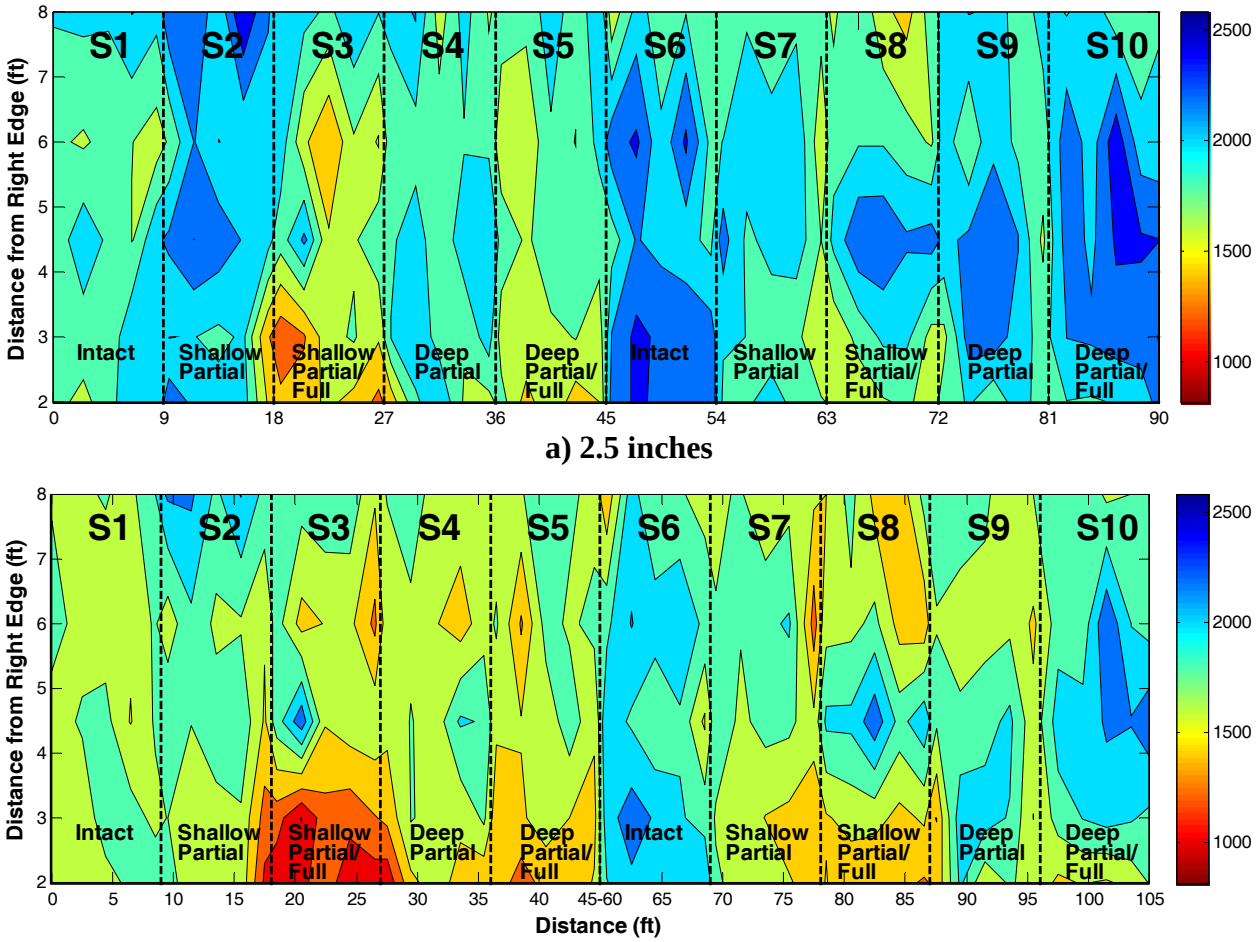

a) 2.5 inches

b) 8 inches

Figure 5.6 – Overall Modulus Results (Top View) on Controlled Study

indication of debonding on the prepared areas is more evident, as detailed in Figure 5.6b. This demonstrates that the USW analysis might be able to identify delaminated areas.

Detailed dispersion curves are presented in Figure 5.7 for the 5 lines and for the 10 sections. Prepared debonded areas are also depicted in the figures. A reduction in modulus can be observed in most sections except section 9. This demonstrates that the USW method might be able to identify delaminated areas.

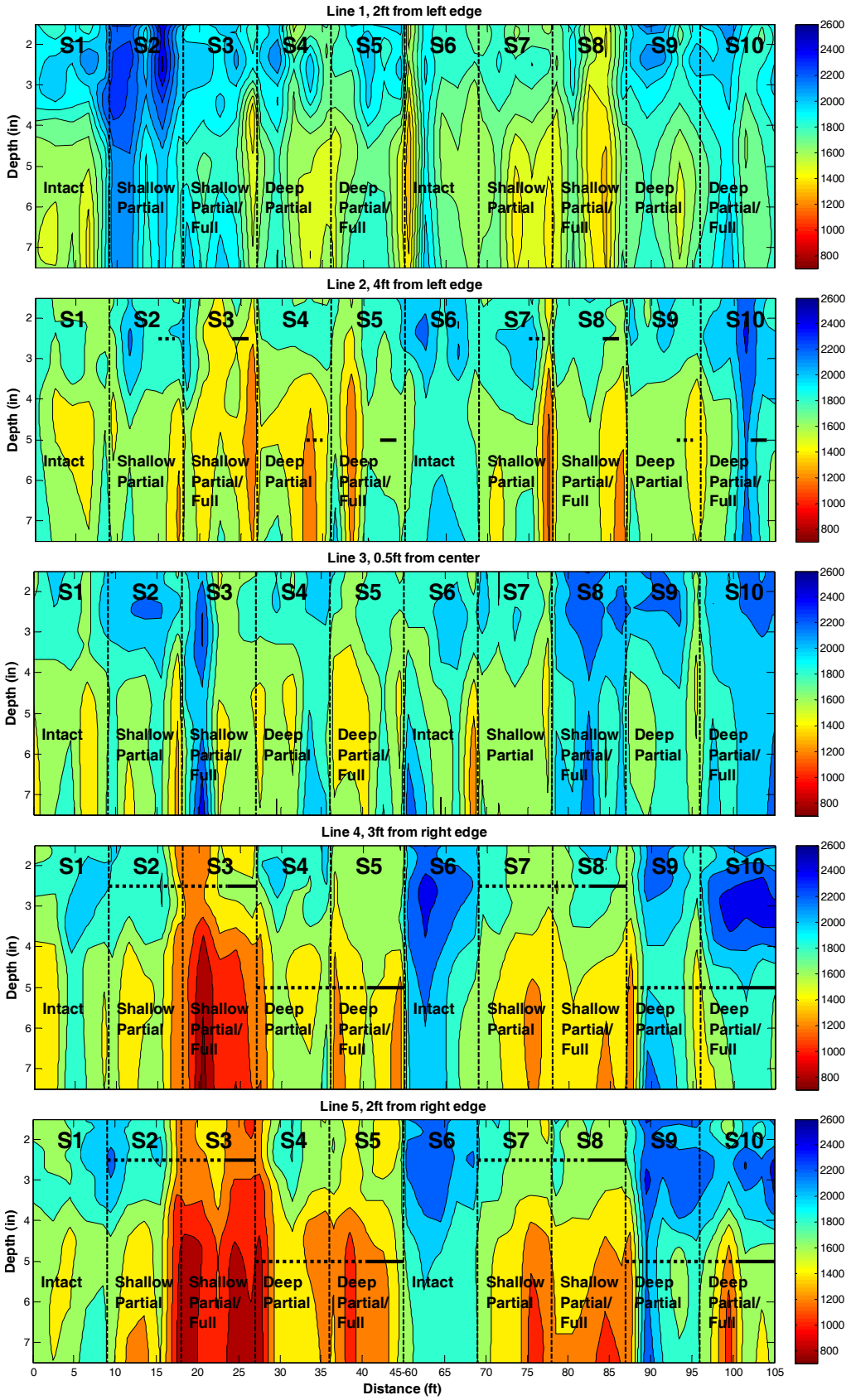

Figure 5.7 – Dispersion Curve Results for 5 Lines (Cross Section)

Impact-Echo (IE) Results

The IE method is based on detecting the resonance frequency of the standing wave reflecting from the bottom and the top of a pavement layer. The IE results are illustrated in Figure 5.8 for intact and severely debonded locations. The normalized amplitude of the frequency response on the PSPA receiver closer to the source was used. To obtain the frequency response, a Fast Fourier Transform (FFT) algorithm was applied to the time records from PSPA. For the case of the intact location, only a peak around 6800 Hz dominates the frequency spectrum. For the case of severe debonding, there is a shift to a lower frequency because a flexural (drum like) mode dominates the frequency response of the incident wave on the asphalt.

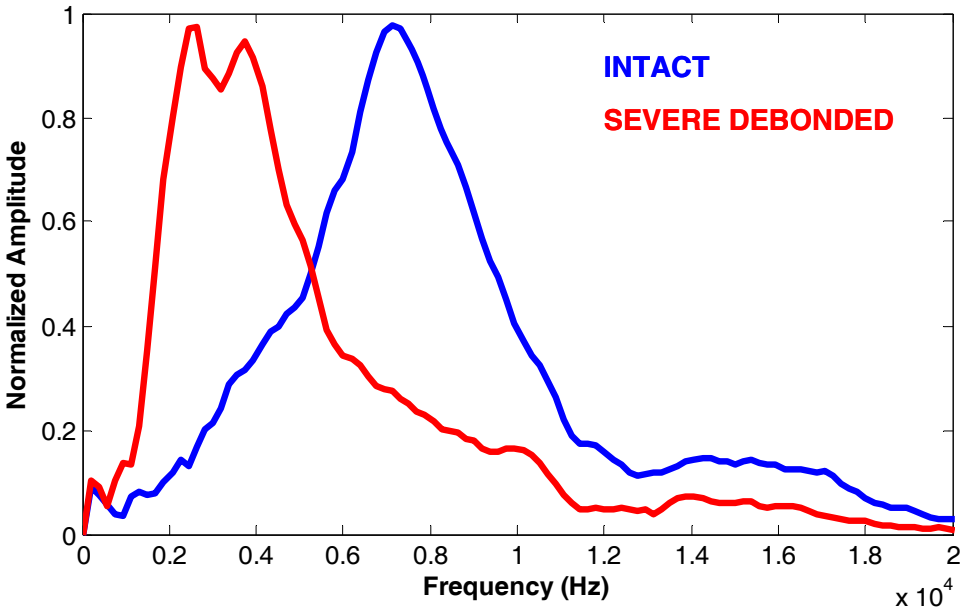

Figure 5.8 – IE Results with PSPA on Controlled Study

The contour maps of amplitude spectra are presented in Figure 5.9. On the intact section, all points show a predominant resonant frequency. Even though signs of debonding can be observed for some of the shallow fully-debonded area, the delineation of partially debonded areas from intact area seems difficult. Perhaps with more advanced analysis, this method can be

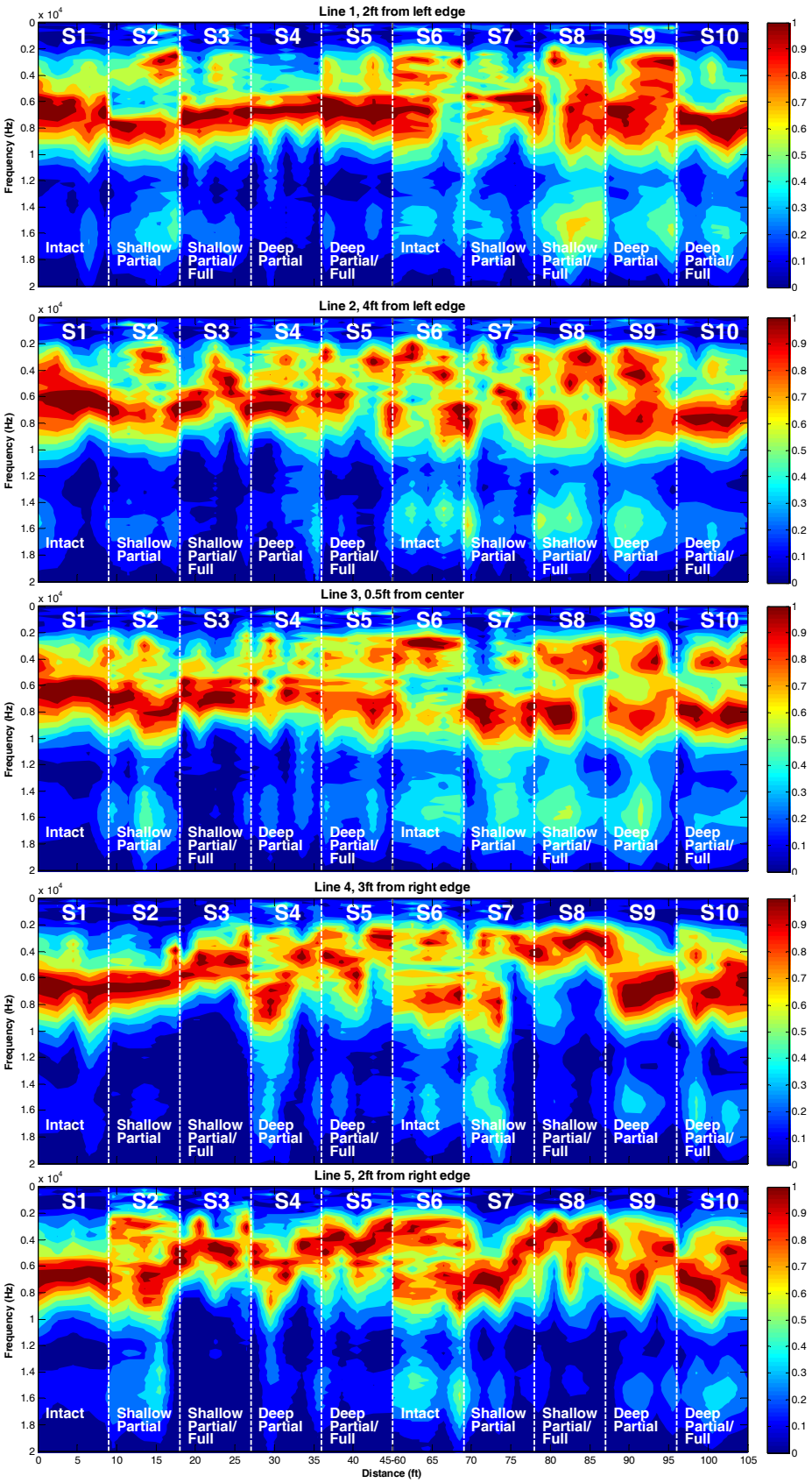

Figure 5.9 – Example of IE Results with PSPA on Controlled Study (Cross Section)

improved for day-to-day use. However, with the current state of the practice, the method may not be as reliable.

Ultrasonic (US)

An ultrasonic low frequency tomography (a.k.a. MIRA) is a low frequency ultrasonic linear array system developed by Acsys (in cooperation with BAM) especially for accelerated concrete inspection. This device is a multi-sensor ultrasonic echo (pulse echo) system, which uses the synthetic aperture focusing technique (SAFT) to provide nearly real-time images of the internal structure of the test object.

MIRA (Figure 5.10) consists of 10 measuring units, each including 4 low-frequency broadband (20-100 KHz) shear transducers with the nominal operation frequency of 50 KHz, polarized perpendicular to the length of the array. Each measuring unit includes also the electronics needed for generating, receiving, and digitizing the signals. The ten measuring units, which form the array, are packaged in the box. The data acquisition is controlled by a laptop computer and the connection between the array and the laptop is wireless.

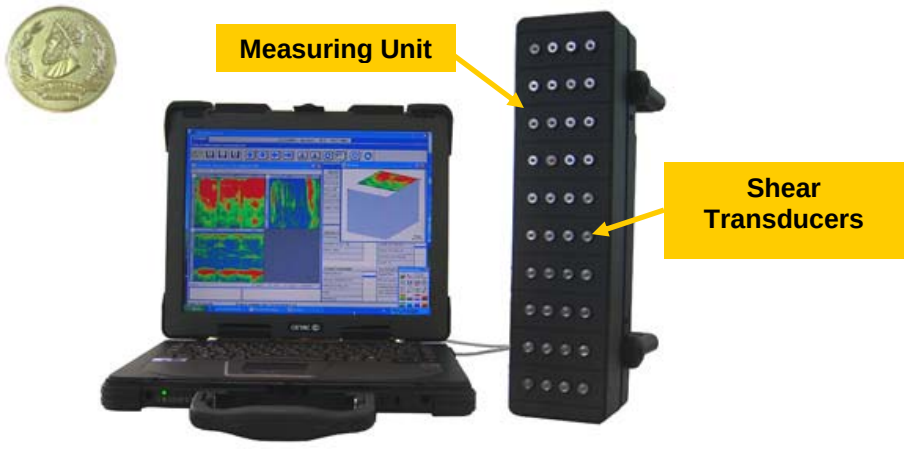

Figure 5.10 – Ultrasonic Linear Array System Used in Preliminary Evaluations

At every test point, a complete "sweep" is carried out (i.e., the first unit acts as the transmitter and all others as receivers, then the second unit acts as the transmitter and the others

record the signals, and this process continues). After one full sweep is completed in less than one second, the data is transferred to the computer, the image is reconstructed using the SAFT algorithm and displayed on the laptop screen (B-Scan). The data measured along a line can be combined into one data set and displayed as B-, C-, and D-scans (Figure 5.11).

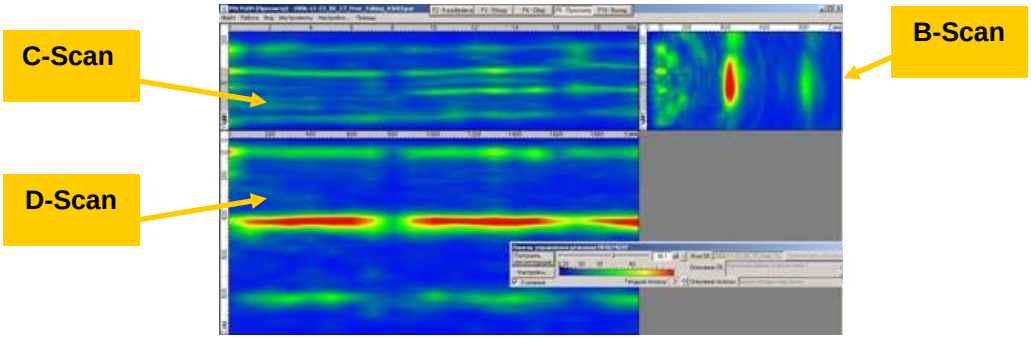

Figure 5.11 – 3D reconstructed Results of Line Measurements

Examples of B-Scans as seen immediately by the operator in the field on sections with no debonding (Section 6) and severe shallow debonding (transition section) are shown in Figure 5.12. The two B-scans are different. The first horizontal interface recognized in the B-Scan of the intact section is at a depth of about 5 in. (125 mm), which corresponds to the thickness of the top two HMA layers. As expected, the reflection from this interface is not very strong. Two other deep faint interfaces are also recognizable in this figure: one appears to be the multiple of the first reflecting interface and the other one might indicate the base-subgrade interface, although the latter interface is expected to appear at a depth of 8 in. (200 mm). This difference may be due to the inaccuracies in measuring the wave velocity during the calibration phase. A strong shallow interface is observed on the severely debonded section (Figure 5.12b). The interface appears at a depth of about 3 in. (75 mm), deeper than the expected 2.5 in. (64 mm, (marked by the red arrow). Multiple reflections are also observed in this figure; the first one particularly strong.

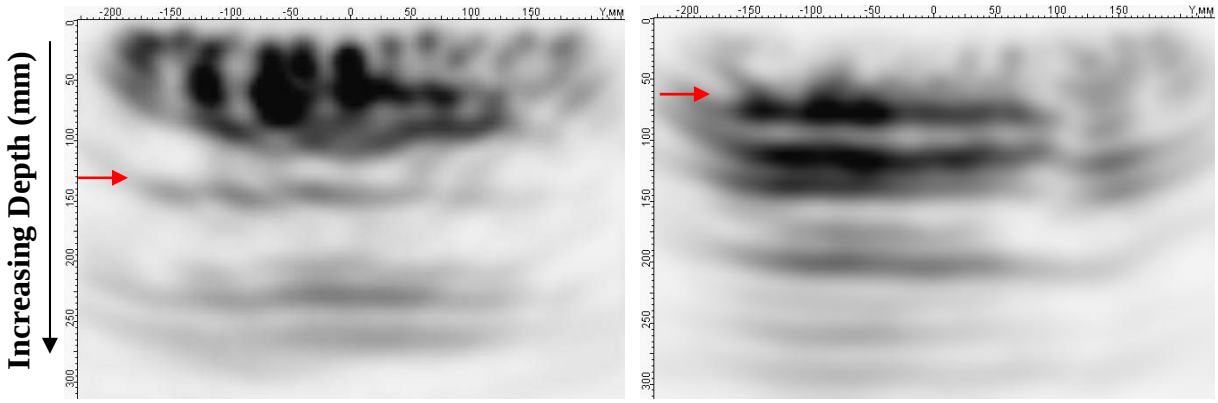

(a) Intact **(b) Severe Debonding**

Figure 5.12 – Examples of Images on Intact and Severely Debonded Sections

Two more field B-scans were obtained taken on shallow and deep fully debonded zones as shown in Figure 5.13. The image from the shallow and fully debonded section (Figure 5.13a) is similar to the severely debonded image (Figure 5.12b). The B-scan for the deep debonded section is rather different and features a very strong reflection at about 5 in. (130 mm) depth, where the debonding is expected. No more reflecting layers are present beyond this strong reflecting layer. A very faint multiple is present at about 11 in. (280 mm).

The test sections were designed and constructed such that they closely reflect the construction practices used for building actual runways. This consideration has resulted in an unavoidable symmetry in the structure of these sections. This built-in symmetry makes it difficult to distinguish, for example between the multiple reflections from a shallow delamination (at 5 in. and 7.5 in.) and direct reflections from the second and third structural interfaces at 5 in. and 8 in., respectively. More sophisticated post-processing algorithms may be used to remove multiples and differentiate different interfaces.

Ambiguities in interpretation of the results can be greatly reduced if instead of point measurements, line measurements are taken. Line measurements enable a 3-D reconstruction

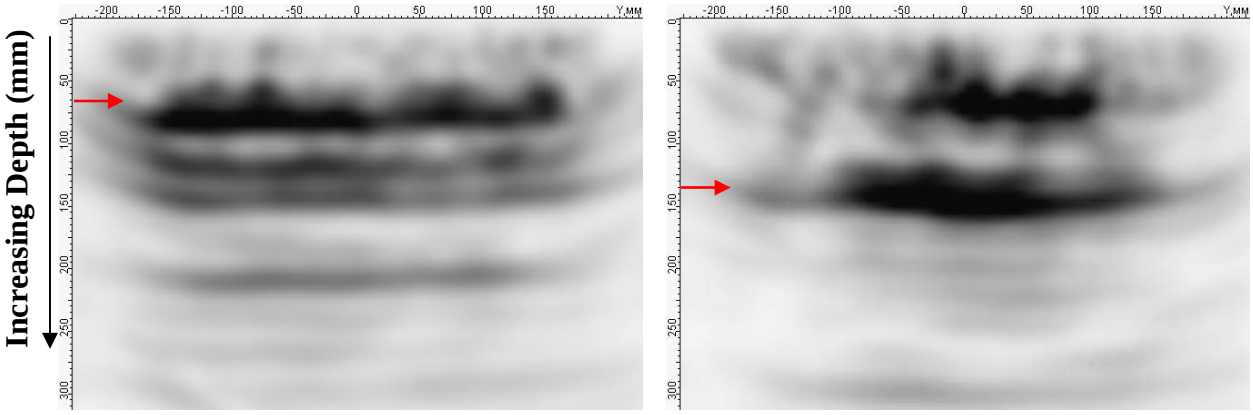

(a) Shallow Fully Debonded **(b) Deep Fully Debonded**

Figure 5.13 – Examples of Images on Sections with Shallow and Deep Debonding

and viewing of the results in the form of interrelated B-scans, C-scans, and D-scans. This will greatly facilitate the field interpretation of the results. However, line measurements require measurements at relatively small intervals of 4 in. (100 mm) which may make the field testing longer. Moreover, the data collection is sometimes challenging because of the difficulties in achieving the required coupling at certain positioning of the device, required to complete one line of measurements or a 'band'.

An example of a reconstructed band (without any additional post-processing) taken on Section 3 is shown in Figure 5.14. The C- and D-scans represent the field reconstructed results from a series of measurements taken at 4 in. (100 mm) steps along a 10 ft (3 m) long line and a 1.5 ft- (450 mm) wide band. The C-scan is taken at a depth of 3 in. (or 75 mm). The extent of built-in shallow fully debonded sections is marked with red. Despite the occasional difficulties with coupling (due to the HMA roughness), the debonded zones are distinguishable in the C-scan. The results of point and line measurements indicate that the ultrasonic measurements may be used to locate the debonded interfaces within HMA.

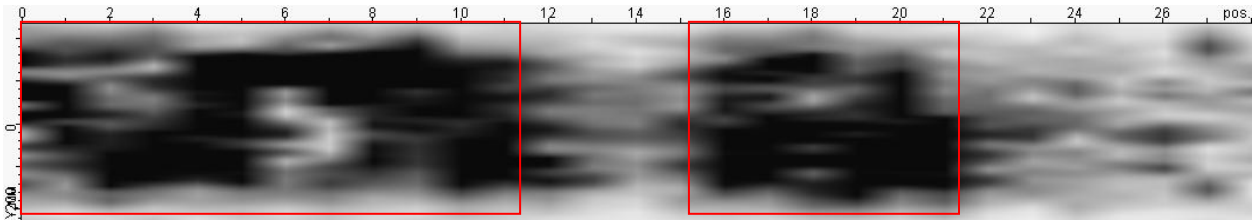

(a) C-Scan at 3 in. Depth

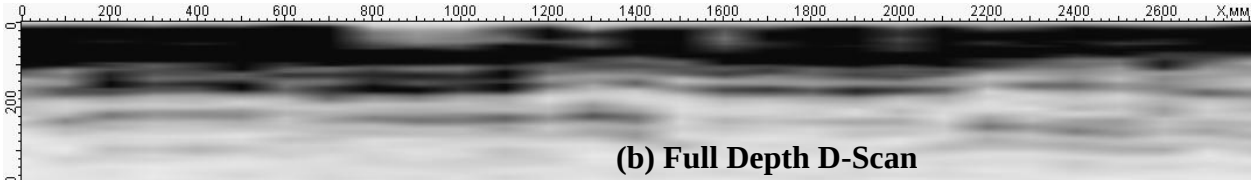

(b) Full Depth D-Scan

Figure 5.14 – Field Reconstructed Results from Line Measurements on Section 3

Impulse Methods

Falling Weight Deflectometer (FWD)

The FWD used on this study consisted of an impact loading mechanism and a set of seven geophones to measure vertical surface displacements. The entire system is trailer mounted as shown in Figure 5.15a. The first geophone (or SD1) was located right underneath the load and each of the other geophones was placed at 1 ft (300 mm) intervals (see Figure 5.15b). The loading device consisted of a 12 in. (300 mm) diameter load plate (Figure 5.15b) and an equivalent load of about 6,000 lbs (27 kN) was applied on the asphalt section at selected locations. A total of 90 points were considered in the preliminary study. Only Lines 1, 3 and 5 and Points 1, 3 and 5 of each section (see Figure 5.1 for details) were evaluated. Each test consisted of a setting drop, followed by three additional drops. The average vertical displacement of the last three drops measured with each geophone was used for every test location.

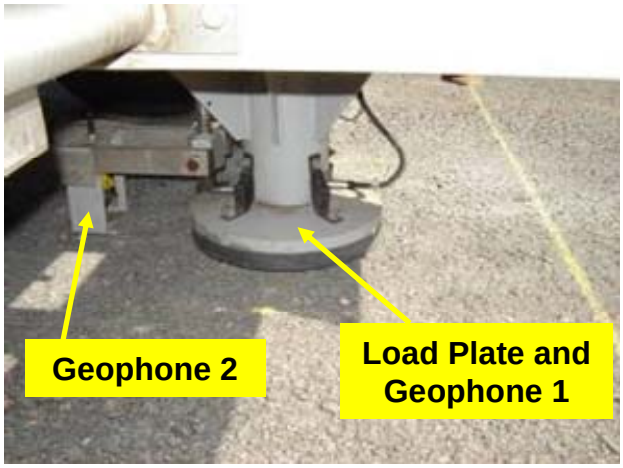

a) Trailer Mounted FWD **b) Load Plate Detail**

Figure 5.15 – Falling Weight Deflectometer on Controlled Study

Deflections measured for the seven geophones at an intact and the severely debonded locations are shown in Figure 5.16. Deflections of Geophones 1 and 2 (labeled as SD1 and SD2) are considerably greater at the severe debonded location. For the other five geophones, differences between intact and deboned deflections are small.

The variation in the deflection along the ten sections is shown in Figure 5.17. The color code criteria presented in Table 5.2 were used. In this case because higher deflections correspond to less stiff material, standard deviations were added instead of subtracted.

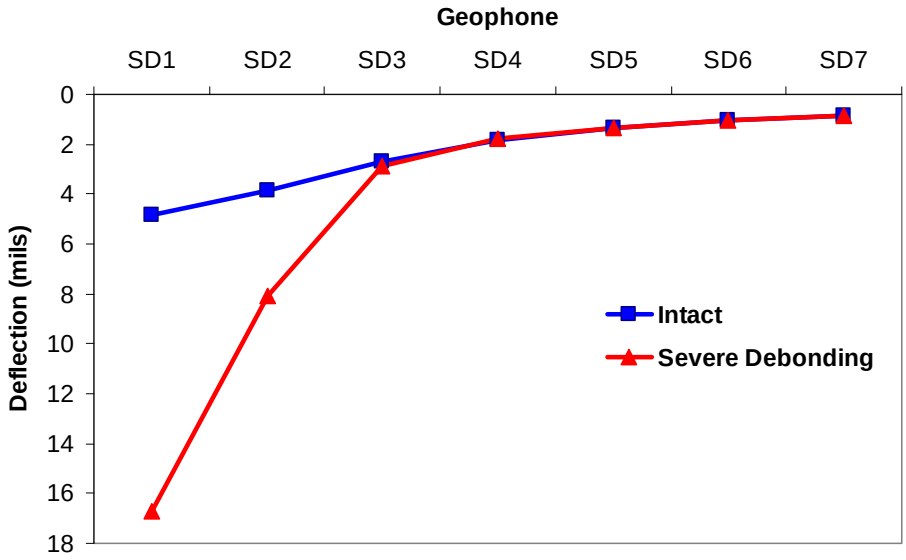

Figure 5.16 – Deflection Examples from FWD on Controlled Study

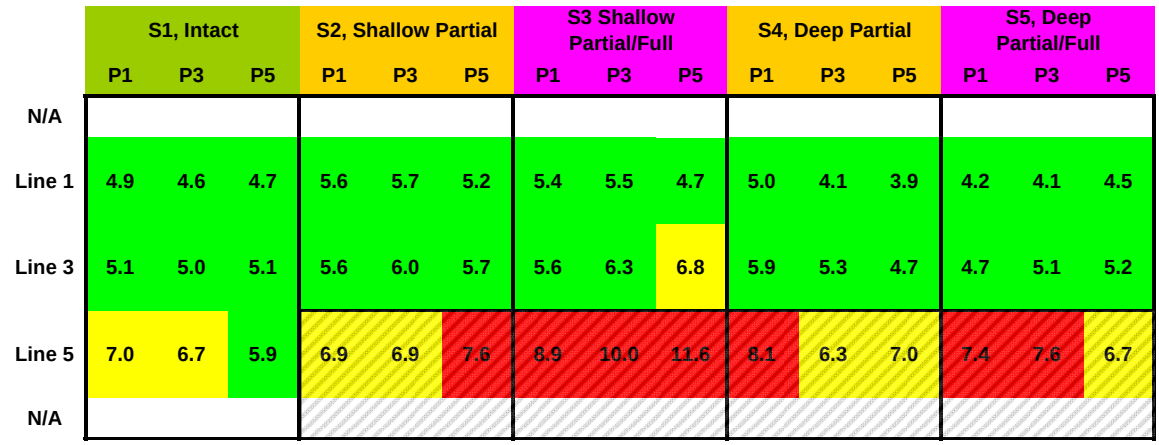

a) Sections 1 to 5

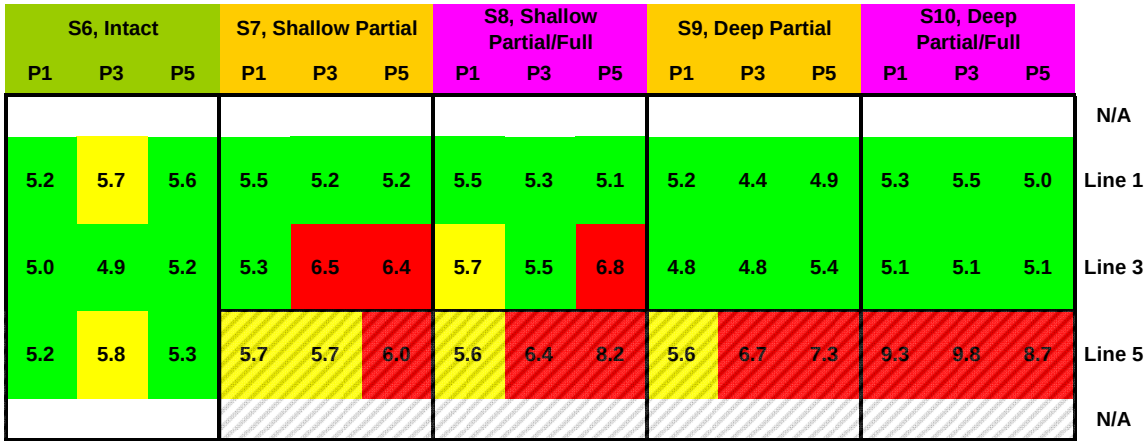

b) Sections 6 to 10

Figure 5.17 – Statistical Analysis of FWD Deflection on Controlled Study

As reflected in Figure 5.17, the deflections correspond to the debonding quite well. These deflections were converted to modulus using MODULUS 6.0 (Liu and Scullion, 2001). A 2-layer analysis that considered the entire asphalt thickness (8 in., 200 mm) and a subgrade was used. Asphalt moduli obtained with MODULUS are shown on Figure 5.18. In general, the FWD did quite well in detecting debonding. The only concern is perhaps the number of intact locations that are identified as inferior, especially on Sections 7 and 8.

Light Weight Deflectometer (LWD)

The LWD operates on a similar principle as the FWD, consisting of an impact loading mechanism and a geophone to measure deflections. The LWD used in this study is illustrated in

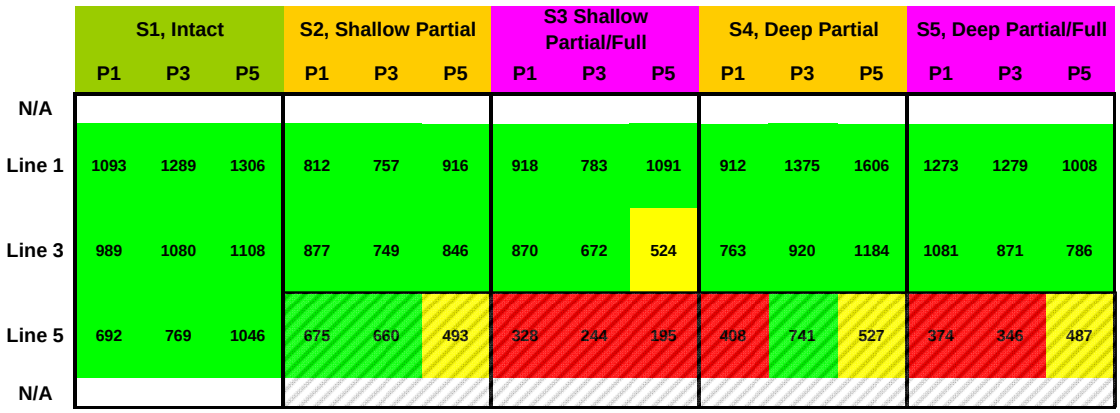

a) Sections 1 to 5

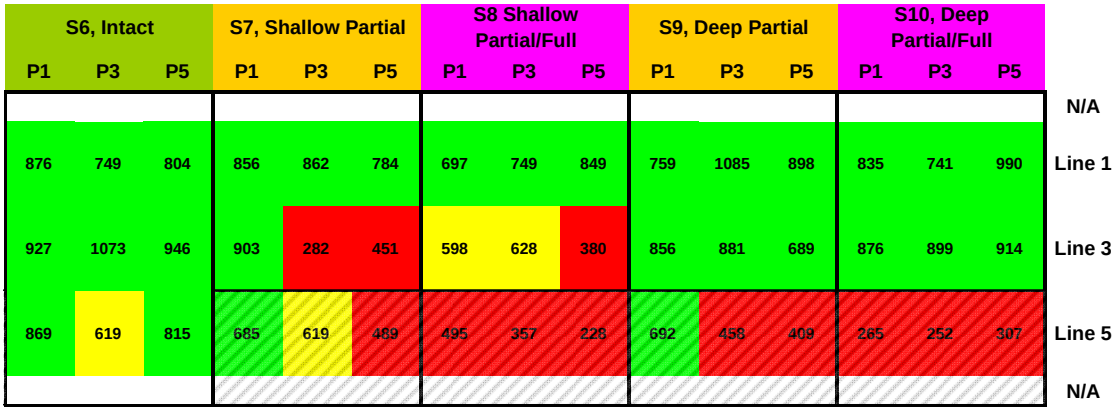

b) Sections 6 to 10

Figure 5.18 – FWD Moduli Results on Controlled Study

Figure 5.19. The device consisted of about 22 pound (100 N) load and a load plate of 8 in. (200 mm) diameter. A sensor underneath the load plate measured the deflection of the load plate during testing. The device also provides the material stiffness based on the deflection measured. For every test the load was raised about 20 in. (500 mm) and dropped to obtain an equivalent load of 1,600 lbs (7 kN). The average deflection and stiffness of three drops after a seating load are reported.

Deflections time-histories measured on the intact and severe debonded locations are shown in Figure 5.20. On the debonded location, maximum deflection (about 15 mils, 380 microns) was approximately 3 times larger than the intact location (5 mils, 125 microns). The debonded location was also replicated to study repeatability of the system. However,

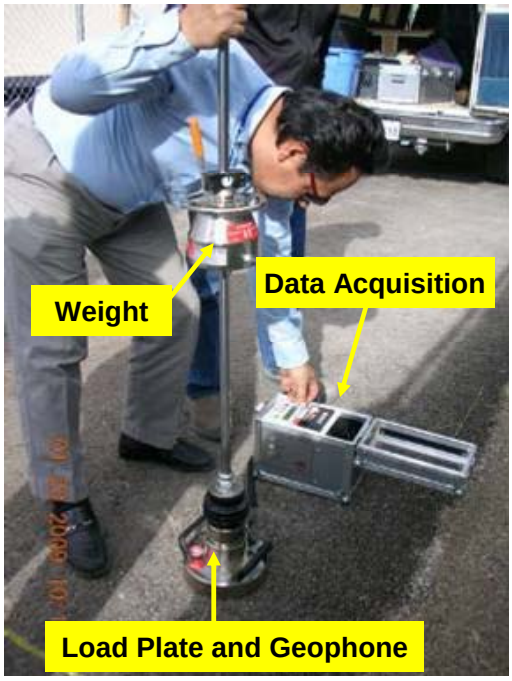

Figure 5.19 – Light Weight Deflectometer on Controlled Study

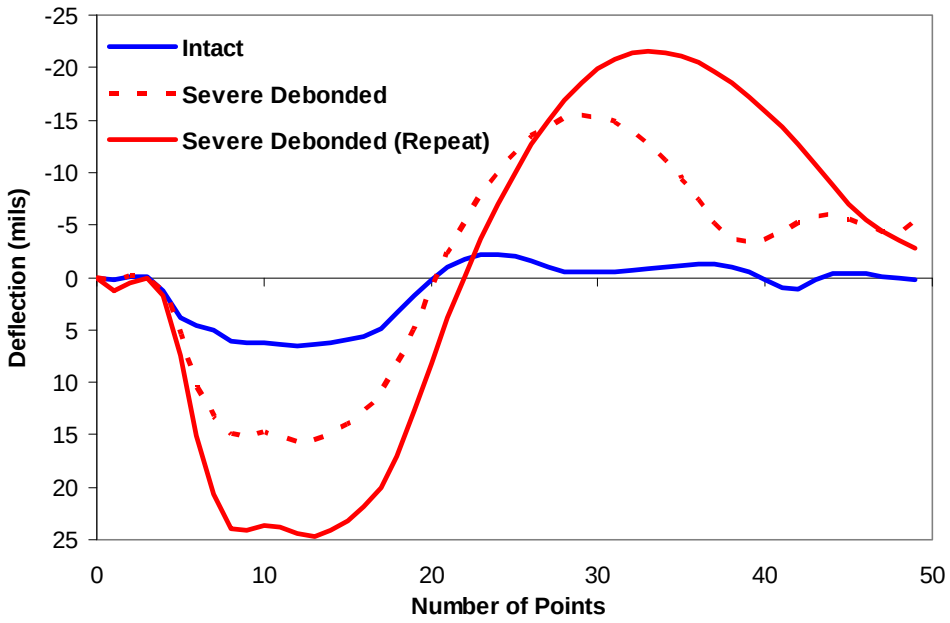

Figure 5.20 – Deflection Examples from LWD on Controlled Study

considerable differences were observed as judged by the maximum deflections measured of 15 and 25 mils for the same location.

The average deflections for the ten sections are shown in Figure 5.21. The LWD did not provide any indication of debonding for almost all debonded area, since higher deflections did not correspond to delaminated areas. However, a number of intact areas yielded higher deflections. Based on this study, it seems that the LWD may not be suitable for detecting debonding.

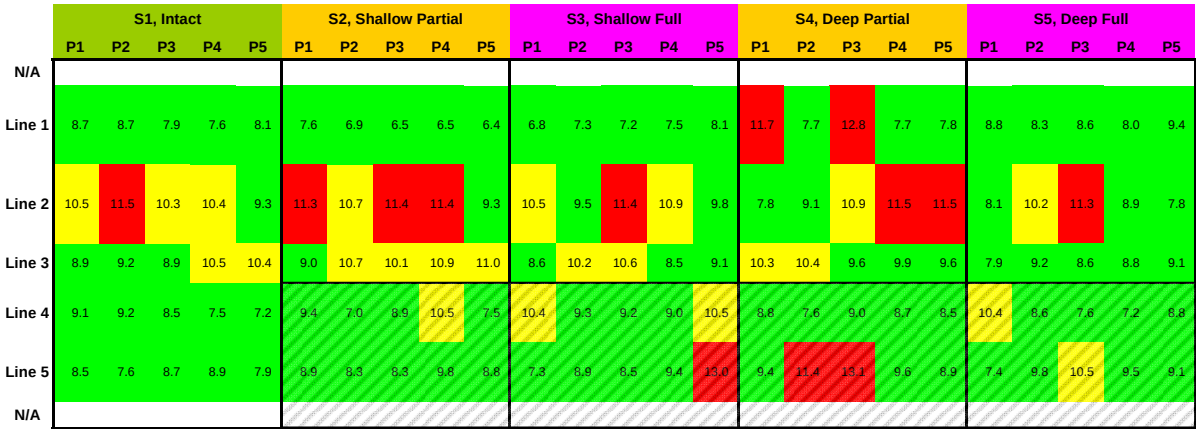

a) Sections 1 to 5

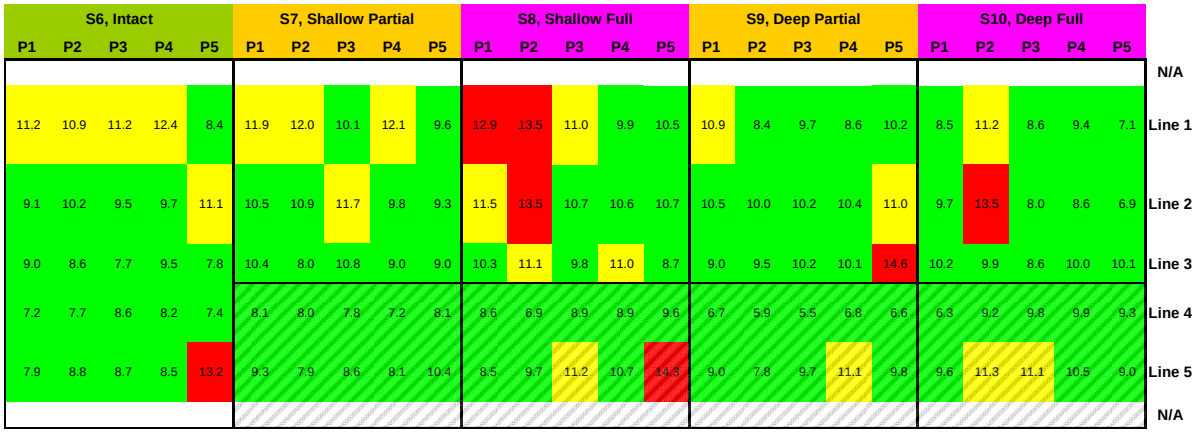

b) Sections 6 to 10

Figure 5.21 – Statistical Analysis of LWD Deflections on Controlled Study

Impulse Response (IR)

The basic operating principle of the impulse response method is to apply an impulsive loading to the pavement surface with a hammer and to measure the vertical displacement using a geophone. If structural distresses are present in the form of loss of adhesion between pavement

layers, this is reflected in the dynamic response of the pavement structure. The response is usually measured in terms of voltage amplitude of the geophone.

The equipment used in this study is shown in Figure 5.22. A 10-lb (45 N) hammer instrumented with a load cell and a 4.5-Hz geophone were used. Both the hammer and the receiver were connected to a portable field computer for data acquisition and storage. The time

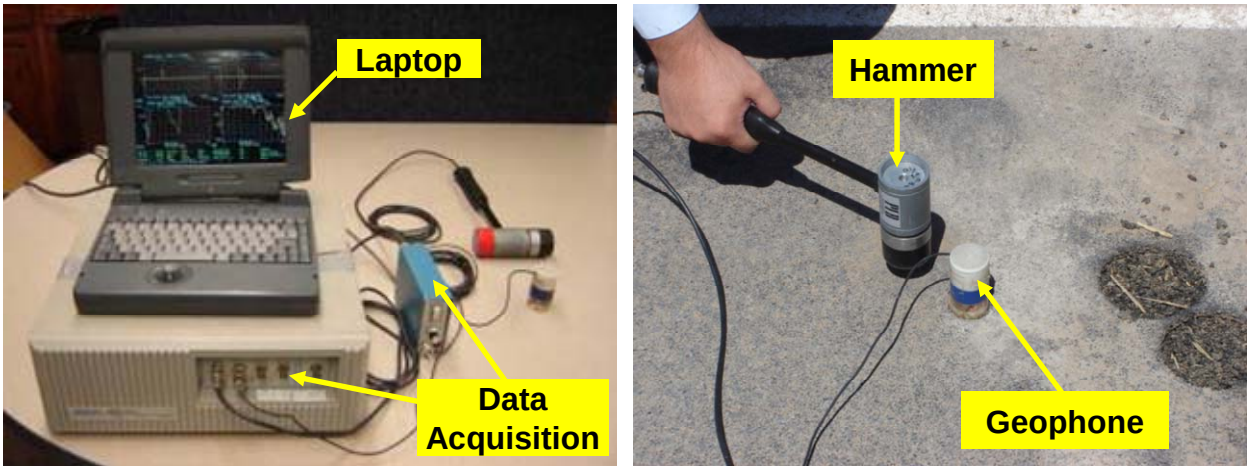

Figure 5.22 – Impulse Response Test Setup

needed to carry out one test, is about 30 seconds. The equivalent load applied by the hammer was kept constant and was around 2,500 lbs (11 kN).

An example of two test results on a sound and severely debonded area are shown in Figure 5.23. The voltage amplitude of the geophone for the severe debonded area was around three to four times as large as compared to the intact location, while the amplitude of the load remained similar. The pulse was also much wider for the debonded record. The ratio between the load cell and geophone amplitudes was used in this study first because of its simplicity. Smaller ratio corresponds to greater flexibility of the section and therefore debonded locations.

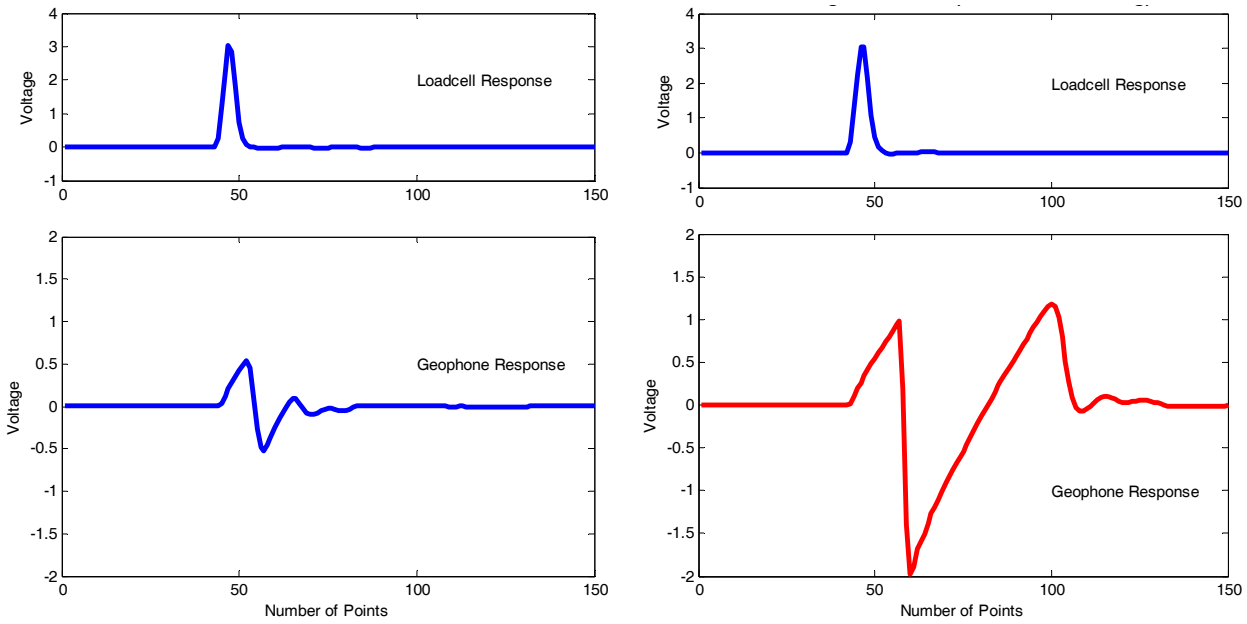

a) Intact **b) Severe Debonding**

Figure 5.23 – IR Examples on Controlled Study

Results are summarized and color-coded in Figure 5.24. Most of the fully debonded areas along lines 4 and 5 were identified on the coarse mix and only a few on the fine mix, mostly on line 5. Some partially debonded areas showed indication of marginally less stiff (marked as yellow), but some were found to be intact (green) or substantially less stiff (red). For the case of the intact locations (line 1 and sections 1 and 6), the majority of the points were categorized as intact.

A more appropriate but slightly more complicated analysis consisted of determining the frequency responses using a FFT algorithm. The frequency responses for the intact and severe debonding cases are presented in Figure 5.25. The amplitude spectra for the loads were similar. However, a significant difference was found when the geophone responses were compared. For the intact location the amplitude presented a dominant frequency of about 300 Hz with amplitude of 4.5 and for the severe debonded the frequency was erratic and the maximum amplitude was close to 30. The ratio of the maximum values of the FFT amplitude was used to compare the

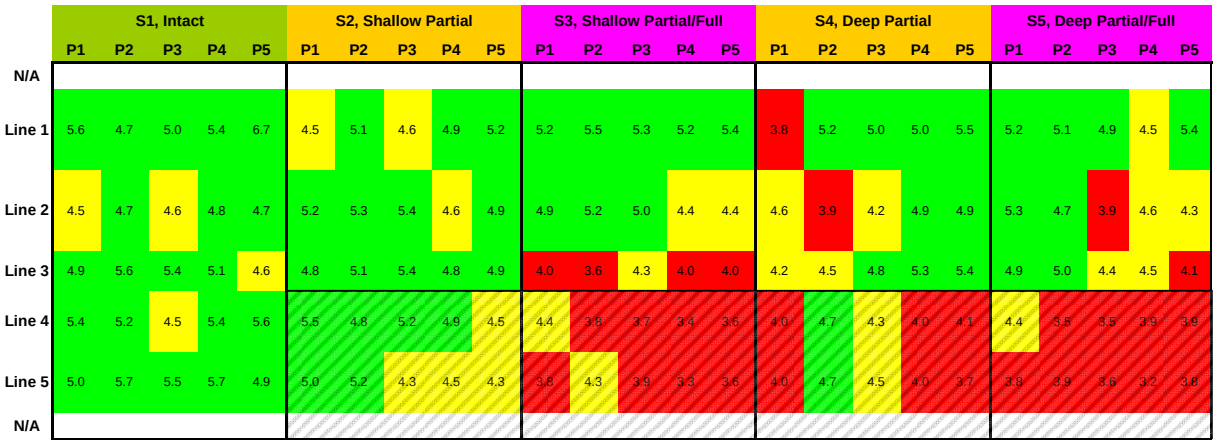

a) Sections 1 to 5

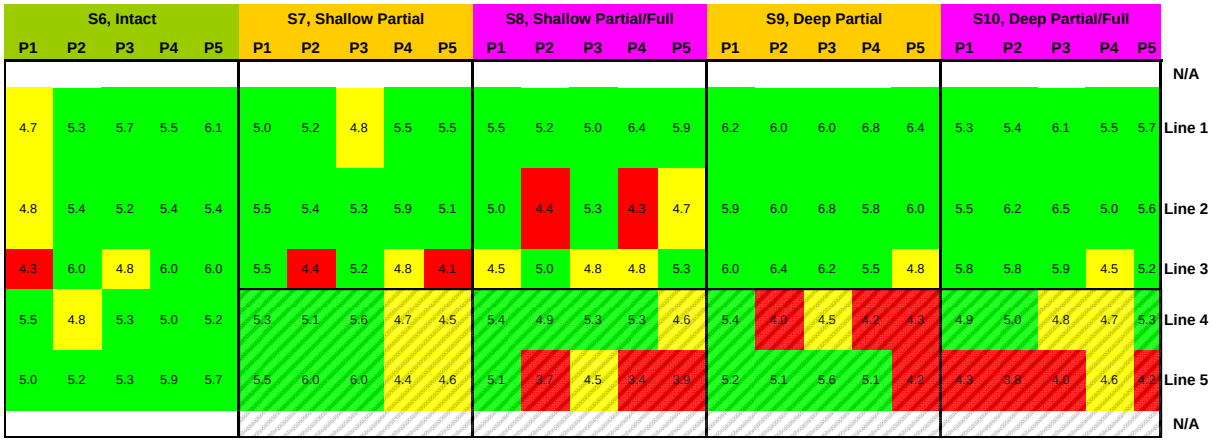

b) Sections 6 to 10

Figure 5.24 – Statistical Analysis of Voltage Amplitude Ratio of IR on Controlled Study

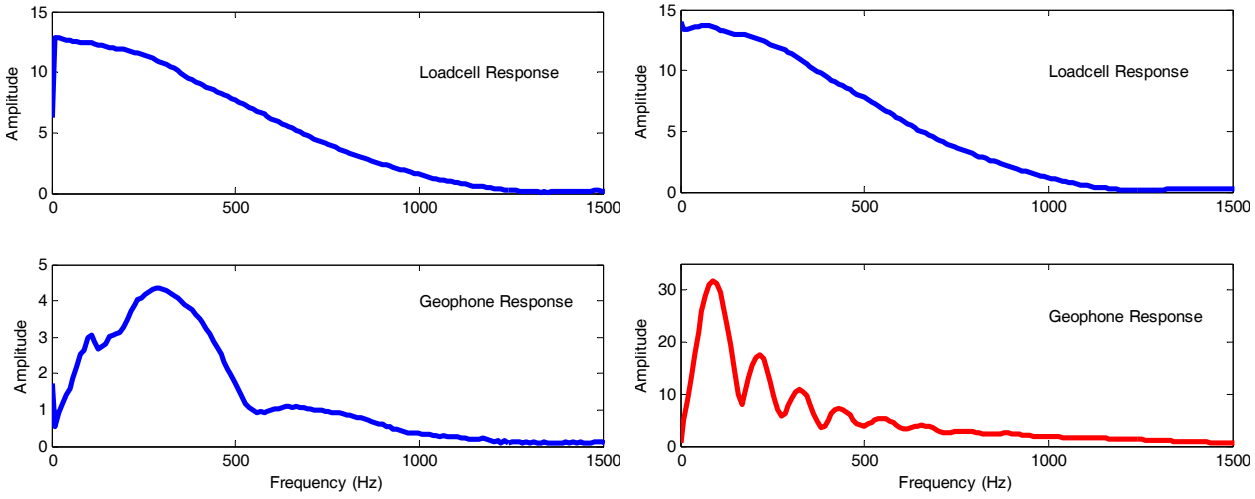

a) Intact **b) Severe Debonding**

Figure 5. 25 – FFT Results from IR Examples on Controlled Study

results as color-coded in Figure 5.26. In this case most of the fully debonded points were identified for both mixes. The partial debonding did not show as much sensitivity similar to the voltage ratio described earlier. Most of the intact locations were identified as intact. Once again, the IR method seems promising for the detection of debonding.

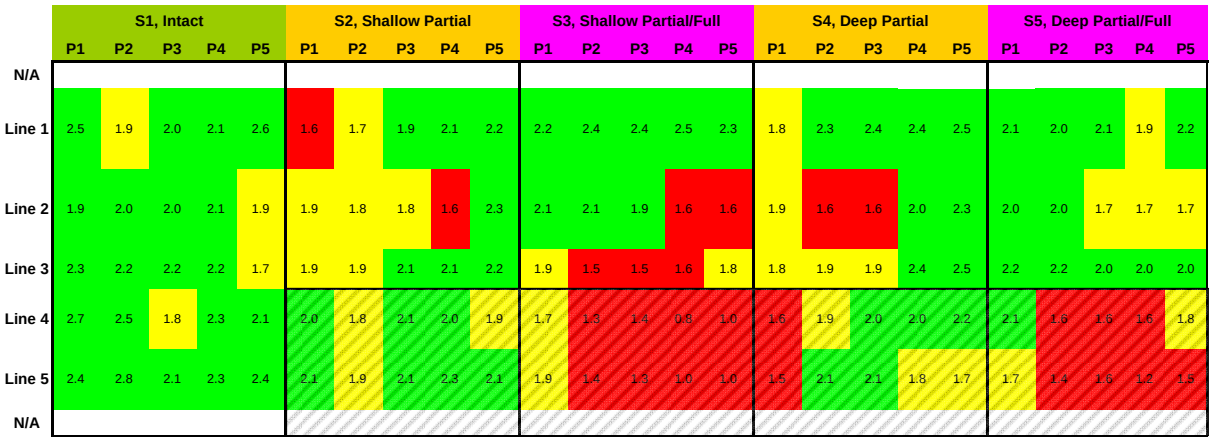

a) Sections 1 to 5

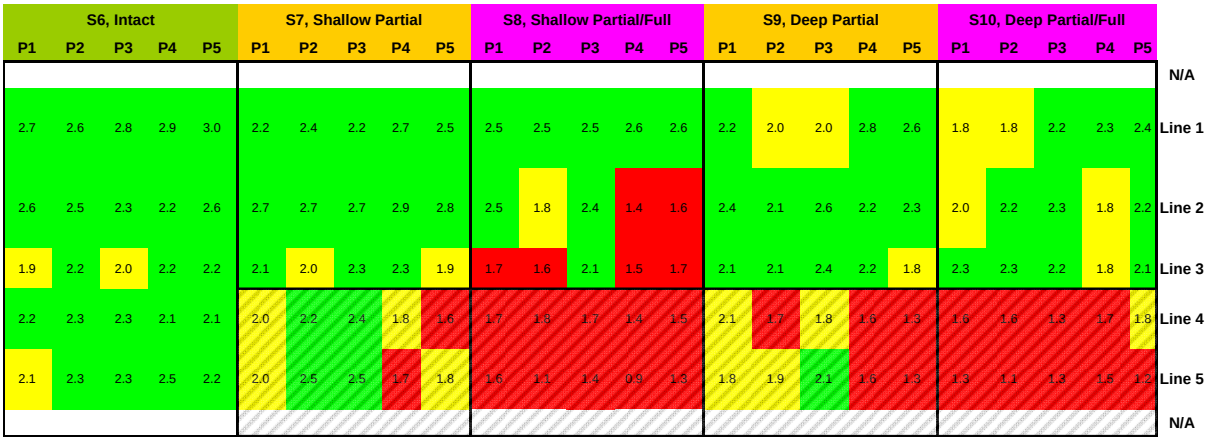

b) Sections 6 to 10

Figure 5.26 – Statistical Analysis of FFT Amplitude Ratio of IR on Controlled Study

Vibration Methods

Stiffness Gauge

The soil stiffness gauge (SSG) used in this study is depicted in Figure 5.27. The SSG is a 11 in. (280 mm) in diameter and 10 in. (250 mm) in height portable cylinder with a 4.5 in. (114 mm) outer diameter and 3.5 in. (89 mm) inner diameter ring-shaped foot extending from the

Figure 5.27 – Stiffness Gauge on Controlled Study

bottom of the device and it weighs approximately 22 lbs (100 N). The stiffness gauge vibrates the material in the range of frequencies of 100 Hz to 200 Hz using small load amplitudes. The variation in stiffness (displacement/load) with frequency (called stiffness spectrum) is used to measure the modulus of the material. To collect a point the SSG is carefully placed on the point of interest and the operator starts the sequence. The SSG typically requires one minute to carry out a measurement. Stiffness obtained on these points ranged from 99 to 420 klbf/in. (17 to 73 MN/m). The SGC stiffnesses for the ten sections are shown in Figure 5.28. Details can be found in Appendix D. The minimum value was obtained on the severe debonded area and the maximum was measured on the debonded area of Section 7 (shallow and full debonding). Similar to LWD, the SSG did not provide reasonable indication of the debonding areas.

High Frequency Sweep

This method uses a high-frequency, hand-held electromagnetic/piezoelectric shaker, which can be used to impart steady state swept vibration at high-frequencies and at high energy. The high-intensity, high-frequency vibration primarily excites the pavement layer. Such

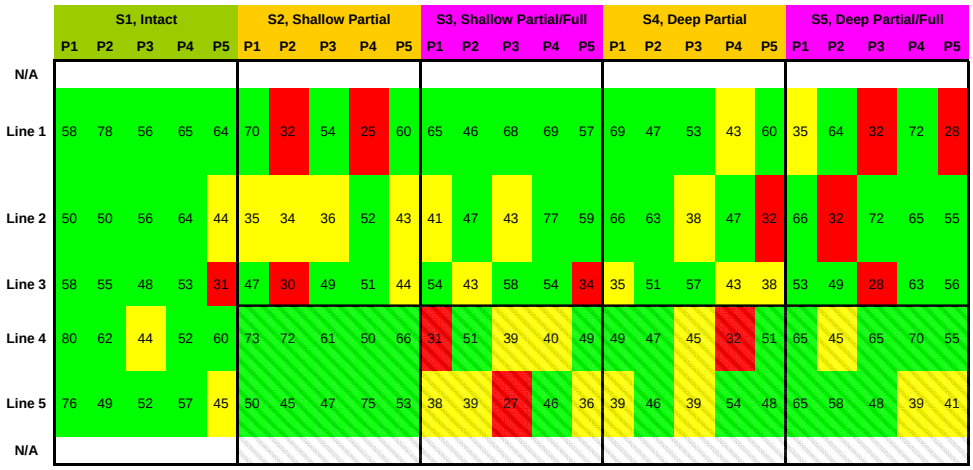

a) Sections 1 to 5

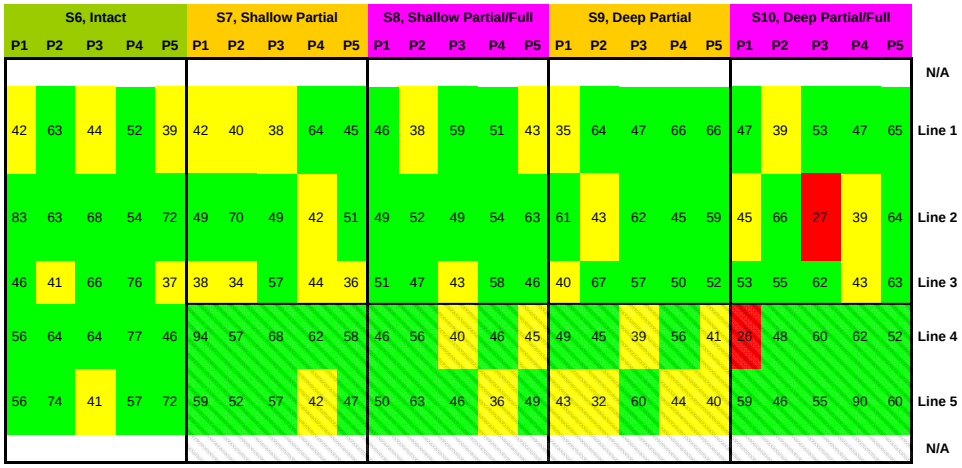

b) Sections 6 to 10

Figure 5.28 – Statistical Analysis of SSG Modulus on Controlled Study

vibrations can be detected by the built-in accelerometer of the shaker. The stiffness spectra from this device can be used to detect the delaminated layer similar to the IR method.

The setup used in this study is shown in Figure 5.29. A dynamic signal analyzer was used to generate a sweep from frequencies of 0 to 20 kHz. The signal was amplified with a signal amplifier and then sent to the shaker. The frequency response between the accelerometer and the load cell inside the shaker was measured and recorded with the analyzer. An example of two tests obtained on a sound and severely debonded areas are shown in Figure 5.30. The frequency corresponding to the maximum amplitude in both cases was similar and around 5 kHz.

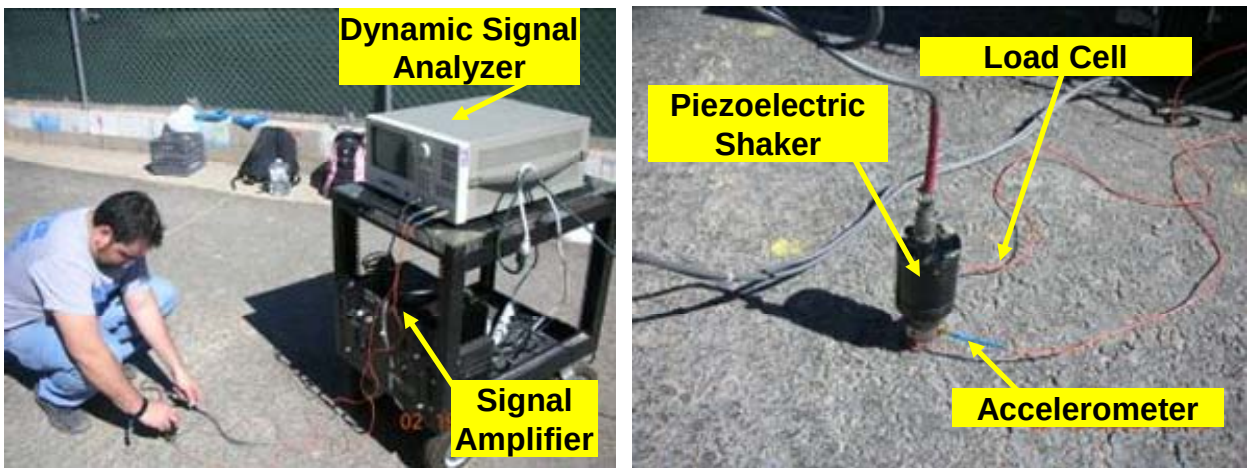

Figure 5.29 – High Frequency Sweep Test Setup

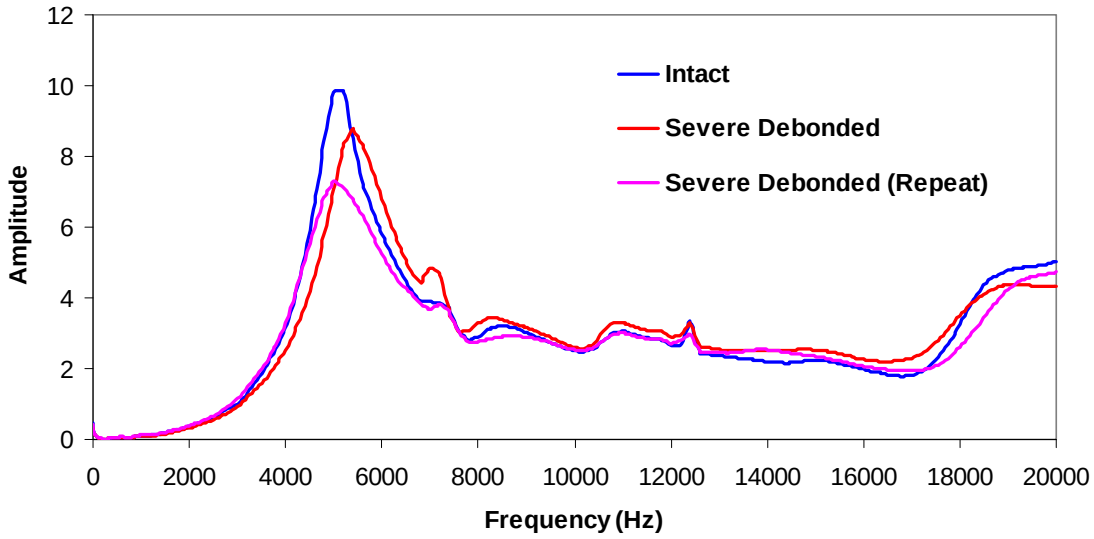

Figure 5.30 – High Frequency Sweep Examples on Controlled Study

Since the time to collect one point required around 5 minutes, only 3 points (P1, P3 and P5) of Line 5 on the first 5 slabs were initially collected. Results are summarized in Table 5.3. The frequencies at the maximum amplitude as well as the maximum amplitudes of the frequency response were very similar for all points and no significant differences among fully- and partially-debonded areas and bonded areas were found. This method also does not seem very feasible.

Table 5.3 – Frequency (KHz) at Maximum Amplitude Measured with High Frequency Sweep at Selected Locations of Controlled Study

Parameters Measured	Section 1			Section 2			Section 3			Section 4			Section 5		
	P1	P3	P5	P1	P3	P5	P1	P3	P5	P1	P3	P5	P1	P3	P5
Frequency at Max. Amplitude	5.1	5.0	5.0	5.1	5.3	5.6	4.7	5.2	5.7	5.1	5.1	5.1	5.0	4.9	5.3
Maximum Amplitude (Volts)	8.8	9.5	10.1	9.0	8.9	7.8	7.5	9.1	7.8	8.9	10.1	9.0	7.4	8.7	9.0

Thermal Methods

Infrared Camera

An InfraCAM™ SD from FLIR systems was used to evaluate the thermal method as shown in Figure 5.31. The camera collects thermal images of a surface area of approximately 2 ft by 2 ft (0.6 m by 0.6 mm) when the camera is used at a height of approximately 4 ft (1.2 m) from the surface. The camera operates on a range of temperatures from 14°F to 660°F (-10°C to 350°C). The operator aims a laser pointer to the surface of the pavement and collects and stores an image of 240x240 pixels. The time needed to collect and store an image is typically 20 seconds.

Figure 5.31 – Infrared Camera on Controlled Study

A combined image around the severely deboned area is shown in Figure 5.32. A passive source (sunlight) was used to create the temperature differentials on the surface of the HMA. The hotter areas (depicted in white) correspond to the area on top of the severe debonding. The same procedure was applied to collect the data on the 10 sections. A total of 25 pictures were obtained on each section at the predetermined locations. Results are presented in Figure 5.33. Only the severely debonded area within the transition zone was clearly detected by the infrared camera. The results of this method were not very encouraging. A more sensitive thermal camera may provide more reasonable results.

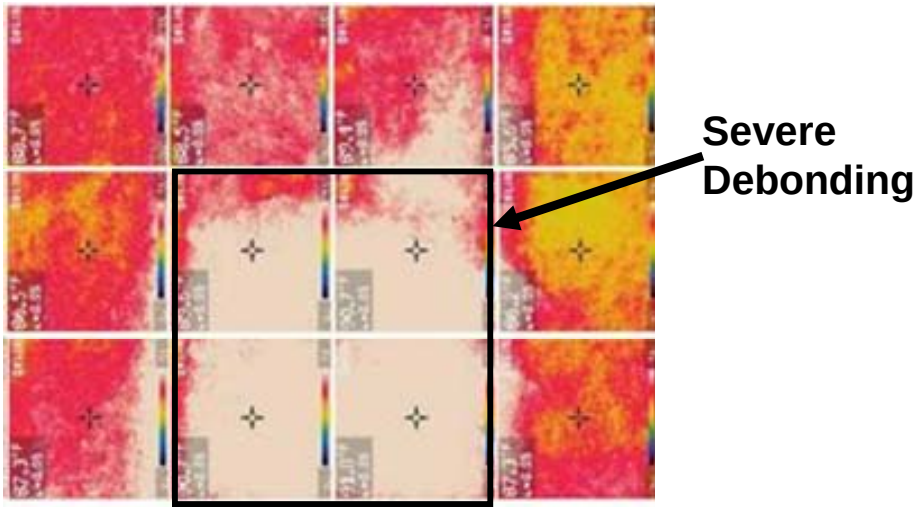

Figure 5.32 – Infrared Camera Results on Severe Debonded Area

Electromagnetic Methods

Ground Penetrating Radar (GPR) is a geophysical nondestructive technique that uses electromagnetic pulses to test, characterize, or detect subsurface materials based on changes in electromagnetic properties of the subsurface layers. Typical equipment setups for GPR surveys are shown in Figure 5.34 for air-launched and ground coupled systems.

GPR emits short electromagnetic pulses radiated through an antenna and receives the reflected signals from the pavement layers. These waveforms are digitized and interpreted by

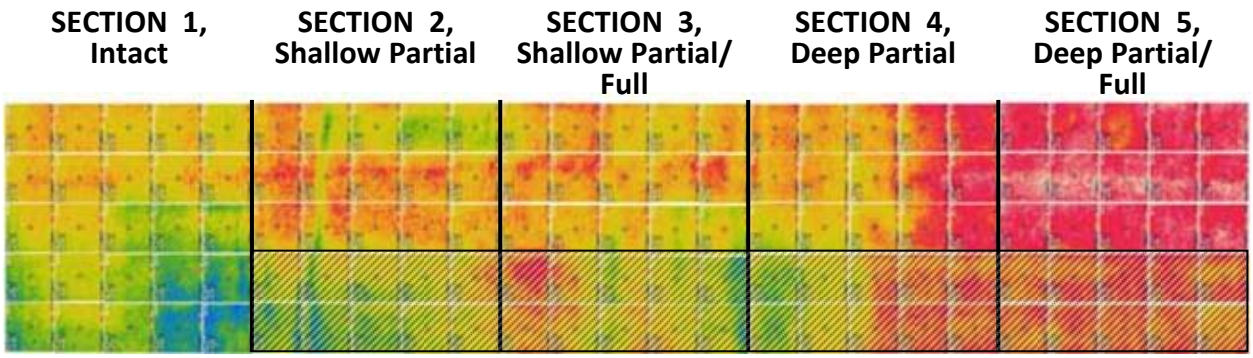

a) Sections 1 to 5

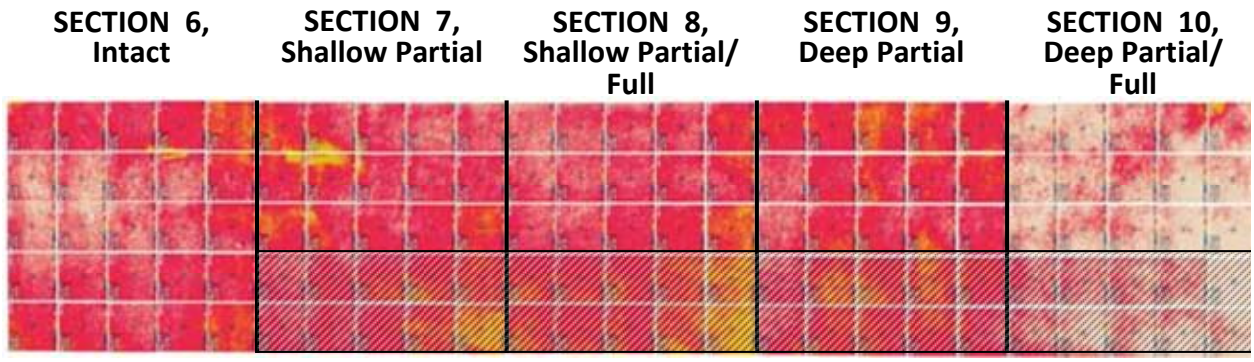

b) Sections 6 to 10

Figure 5.33 – Infrared Camera Results on Controlled Study

Figure 5.34 – Air Launched (Left) and Ground Coupled (Right) GPR Units

computing the amplitude and arrival times from each main reflection. The reflections of these waves at interfaces and objects within the material are analyzed to determine the location or depth of these interfaces.

The air-launched GPR used was a Geophysical Survey Systems Inc. (GSSI) SIR-20 (SIRveyor) 2-GHz antenna (Model 4105) mounted on a supporting beam retrofitted to the back of a van. The system comprised of two-channel data acquisition unit controlled by a laptop computer. The system was also connected to a survey wheel for measuring distance. Lines 1 to 5 were initially investigated with the air-launched system. On average five minutes were necessary to complete an entire line.

A typical raw linescan of an area around the severe debonding is shown in Figure 5.35. The horizontal axis relates to distance measured from the start point (ft) and the vertical axis indicates time measured (nanoseconds). The linescan comprises of different individual waveforms or O-scopes. Examples of typical O-scopes for an intact and a severely debonded area are shown in Figure 5.36. There is a small peak corresponding to the reflection from the debonding.

The linescans with the air-launched system along lines 1 to 5 are shown on Figure 5.37. Locations of the prepared debonding are also included in the figure and the approximate asphalt interfaces of the different layers are included as well for reference (see Figure 5.37a). These

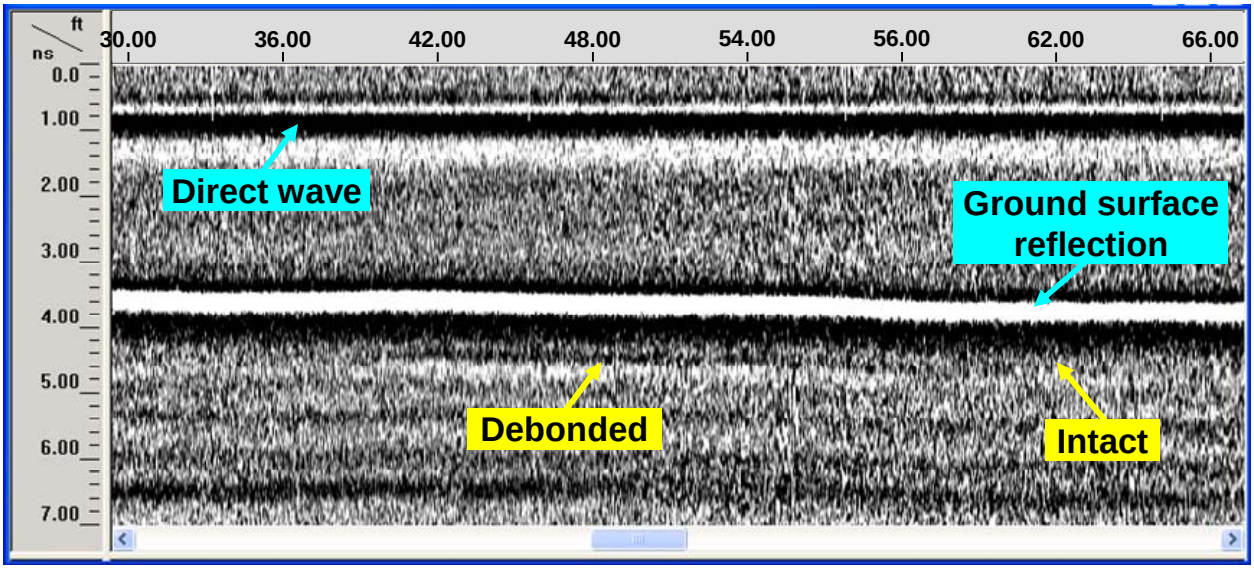

Figure 5.35 – Raw Linescan around the Severe Debonded Area with Air-launched GPR

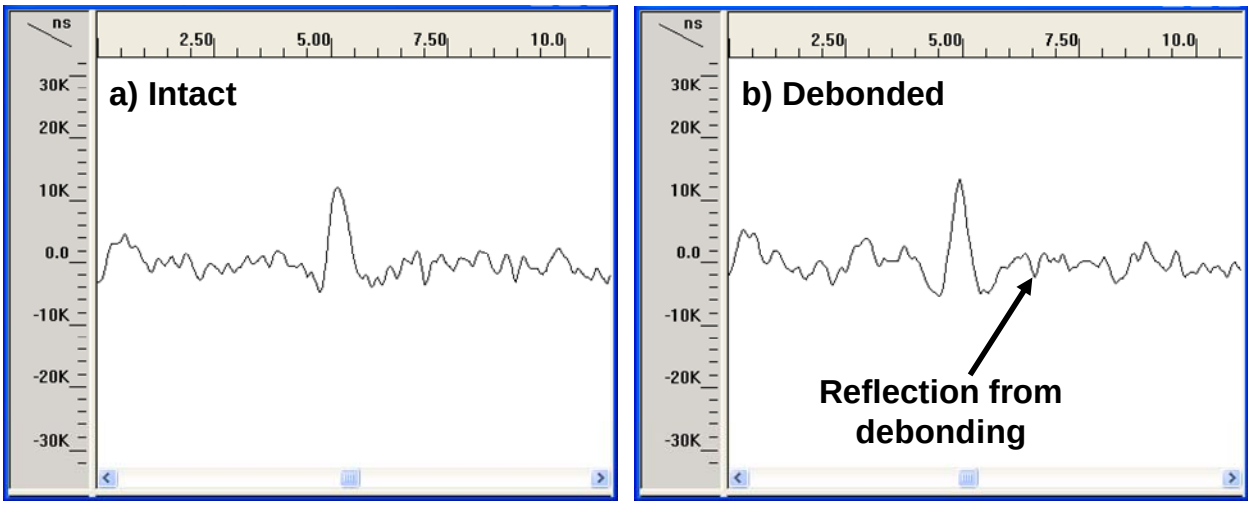

Figure 5.36 – O-scopes for Intact and Severe Debonded Locations with Air-launched GPR

linescans were processed with the GSSI RADAN 6.5 software to remove the direct wave, set the time-zero at the pavement surface and eliminate unwanted signals from the data.

Figure 5.37b shows the linescan for Line 2 at 4 ft from the west edge. Some of the debonded areas of 2 ft by 2ft (0.6 m by 0.6 m) were identified at depths of 2.5 in. (63 mm). Some indications of debonding are evident along the 4 ft by 9 ft (1.2 m by 2.7 m) areas in Figures 5.37c to 5.37e, but their manifestation is erratic. The debonded areas detected were primarily in the areas where the talcum powder and clay were used as debonding agents. The significant contrasts in the dielectric constants of these agents and HMA might have been the reason for detecting these areas.

The ground-coupled GPR system used consisted of a GSSI two-channel data acquisition unit controlled by a laptop computer, a 1.5 GHz ground-coupled antenna (GSSI Model 5103), and a survey wheel attached to the antenna. Similar to the air-launched GPR, Lines 1 through 5 were investigated. On average 10 minutes were necessary to complete a line. A typical scan of the severely-debonded area is shown in Figure 5.38. The O-scopes for intact and severely

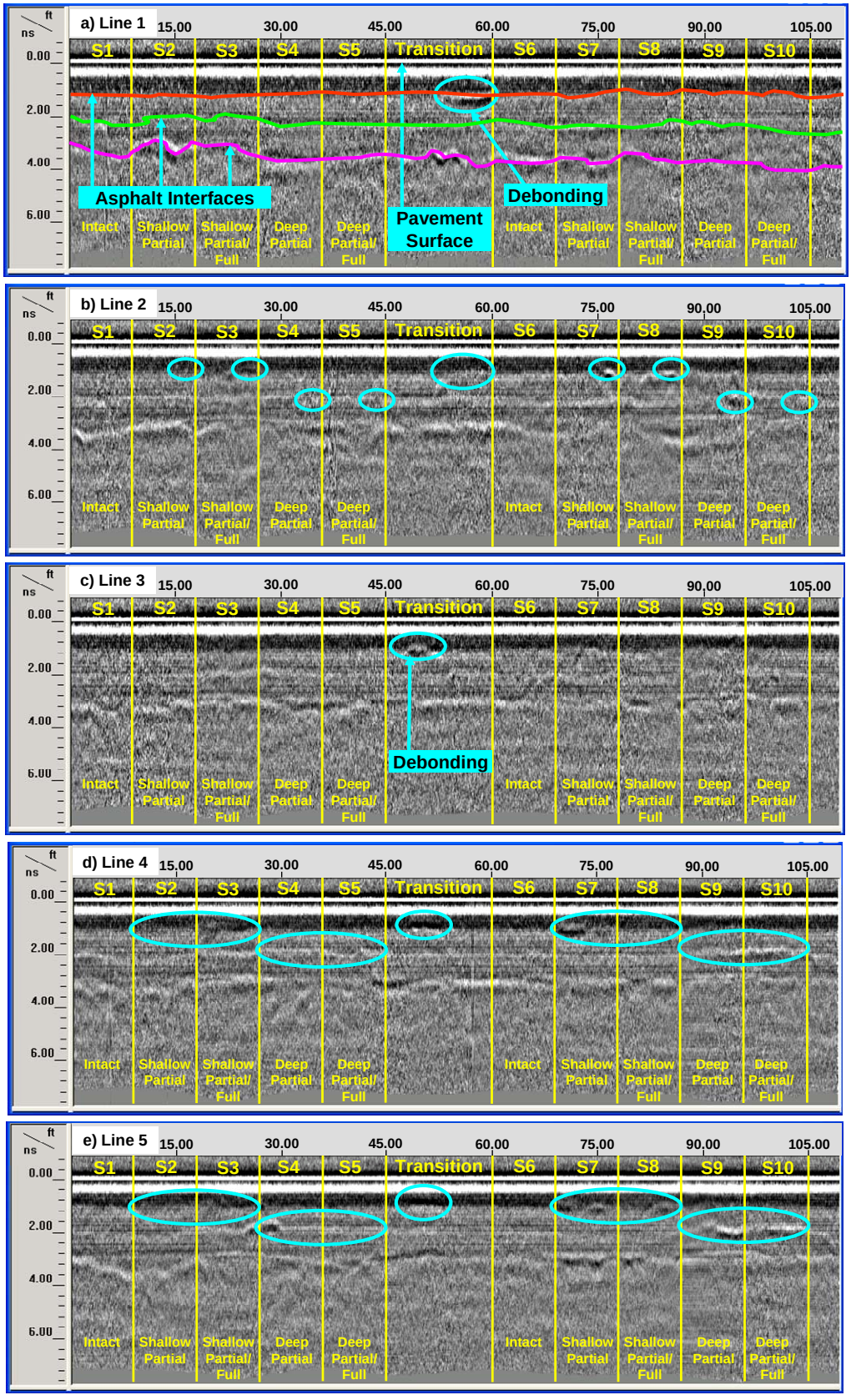

Figure 5.37 – Processed Linescans with Air-launched GPR on Controlled Study

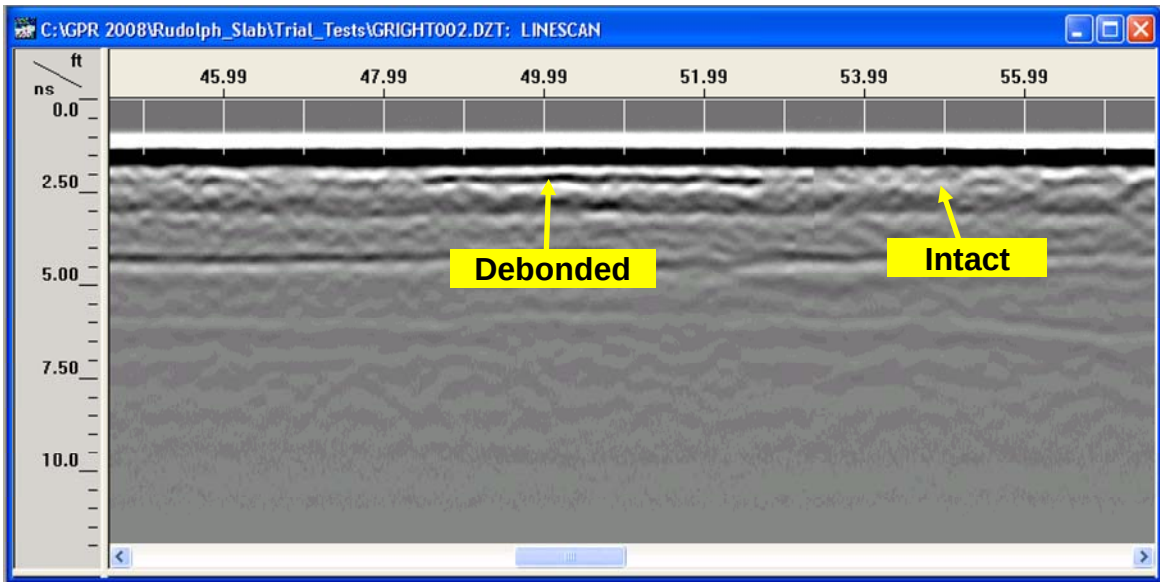

Figure 5.38 – Linescan around the Severe Debonded Area with Ground-coupled GPR

debonded locations are shown in Figure 5.39. The reflections from the severely debonded area can be more easily observed in this case because of the higher amplitude apparent on the O-scan. Complete post-processed linescans for all 5 lines are shown on Figure 5.40. The approximate asphalt interfaces of different layers are shown in Figure 5.40a. The following three analyses were performed to obtain these linescans:

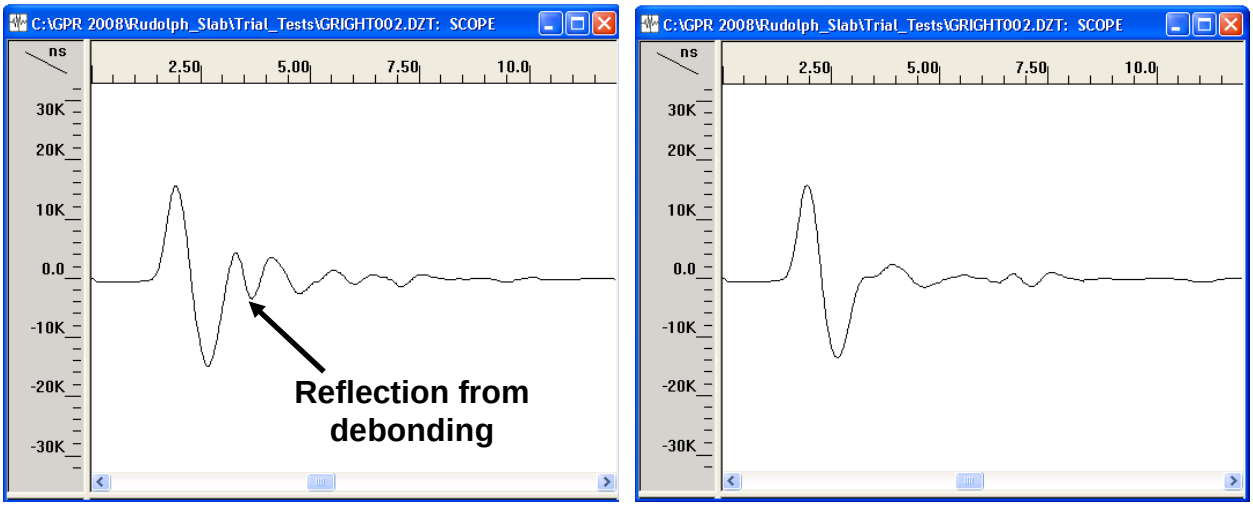

Figure 5.39 – O-scopes for Intact and Severe Debonded Locations with Ground-coupled

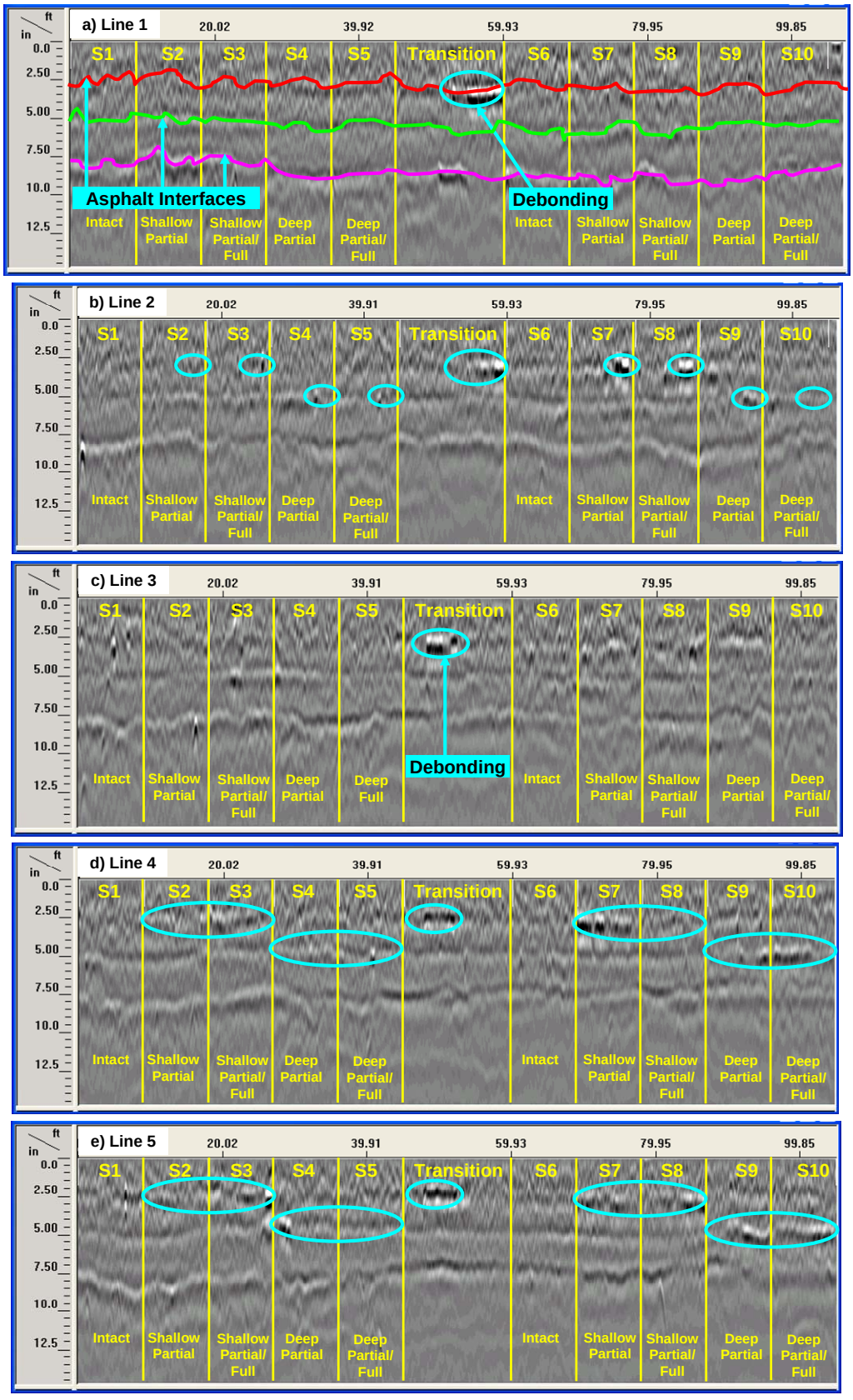

Figure 5.40 – Linescans with Ground-coupled GPR on Controlled Study

- Set Time-Zero (Position): shift the vertical scale so time zero is aligned with the surface reflection in each scan.
- Background Removal: a filter useful for removing horizontal banding.
- Stacking of signals from every 10 scans to accommodate the entire section in a single figure.

Similar to the air-launched GPR, the ground-coupled GPR detected the severely debonded area within the transition zone and some debonded areas primarily constructed on talcum powder or clay (see Figure 5.40).

Simulation of 3D Ground Penetrating Radar

GSSI RADAN 6.5 software is also equipped with a module for creating and analyzing three dimensional (3D) displays of GPR data. The transition zone that contained the severely debonded area and Sections 3 and 5 were investigated with a 3D GPR arrangement. To obtain a 3D representation of an area, a number of closely-spaced survey lines were obtained. GPR data were collected at 6 in. (150 mm) intervals in both longitudinal and transverse directions for the transition area and every 4 in. (100 mm) for Sections 3 and 5. The total time required to collect data at each section was about 1.5 hours. However, with commercially-available 3D GPR antennae, this time will be substantially less.

The images for approximate depths of 0 in. (surface), 2.5 in. (63 mm) and 5 in. (125 mm) extracted from the 3D image reconstruction in the transition area are represented in Figure 5.41a. The debonding agents placed at a depth of 2.5 in. (63 mm) were easy to identify (shown in white), while essentially no defects can be observed at a depth of 5 in. (125 mm). The intensity of the defect detected on the clay slurry is much higher than the thick cardboard. This may

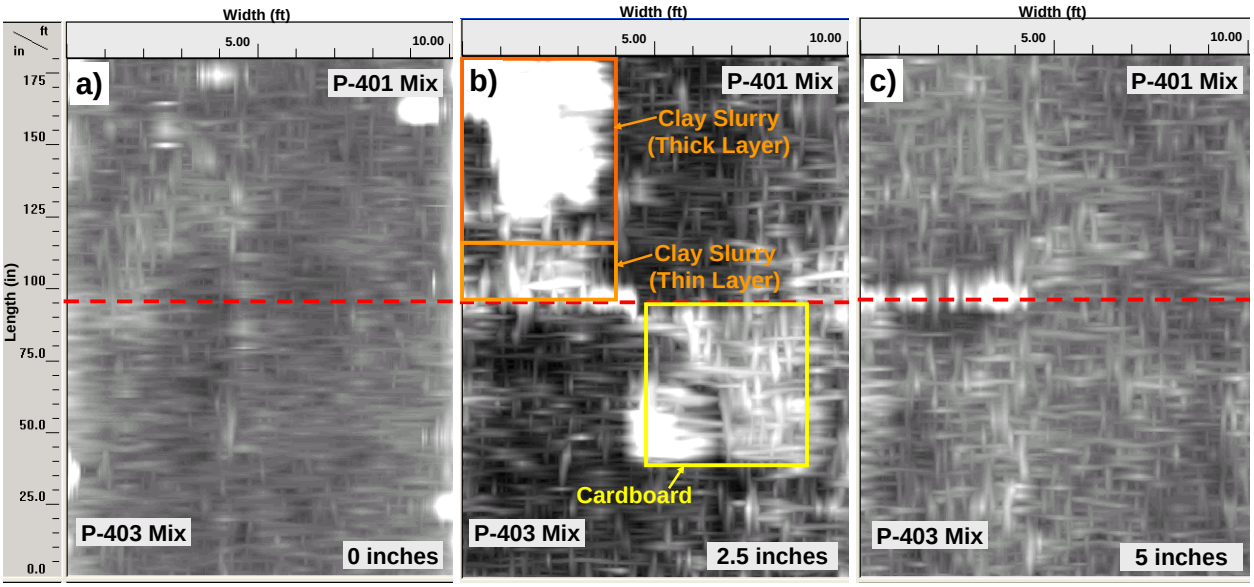

Figure 5.41 – 3D Displays of Transition Section at Different Depths

indicate that the significant differences in the dielectric constants of the clay and HMA might have attributed to its detection.

In actual debonded areas this agent will not exist. The results from testing of Section 3 (shallow debonding) are provided in Figure 5.42 and for Section 5 (deep debonding) in Figure 5.43 for the same depths of 0 in., 2.5 in.(63 mm) and 5 in. (125 mm). The debonding on the talcum powder (partial debonding) area in Section 3 is identified (see Figure 5.42b) but the debonding is not as clear on the paper with oil (fully- debonded). Also the debonded area of 1 ft by 1ft (0.3 m by 0.3 m) is evident, but the 2 by 2 ft (0.6 m by 0.6 m) and 0.5 by 0.5 ft (0.15 m by 0.15 m) are not apparent on the scan. For Section 5 with deep debonding, some indications of delamination appear on the 2 ft by 2 ft (0.6 m by 0.6 m) area but none on the larger area of 4 ft by 9 ft (1.2 m by 2.7 m, see Figure 5.43c).

Based on this study, GPR technology, especially the air-launched GPR, provides limited information about debonding despite its attractiveness as a continuous and rapid survey tool.

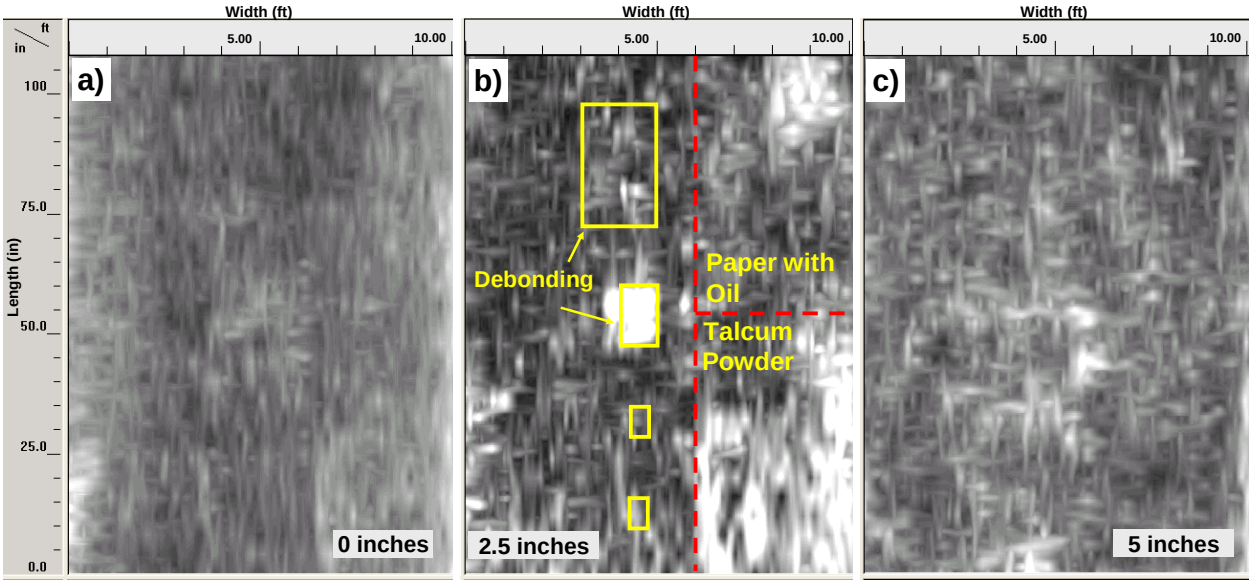

Figure 5.42 – 3D Displays of Section 3 at Different Depths

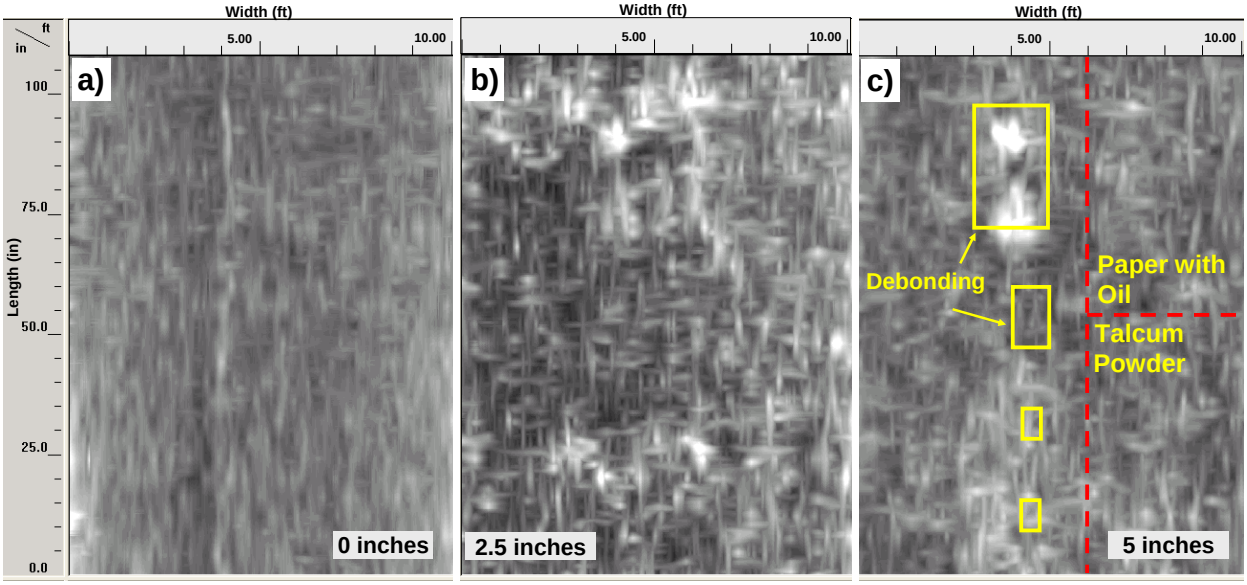

Figure 5.43 – 3D Displays of Section 5 at Different Depths

Coring Results

The goal of the coring operation was to estimate how well the full and partial debonding has been implemented in the filed. As reflected in Figure 5.1, two cores were extracted from each section. These cores were located about at 2.5 ft (0.75 m) from the right edge and at 2 ft (0.6 m) and 7 ft (2.1 m) from the start of each section, respectively. A diamond core system

(Figure 5.44a) was used to extract nominally 4 in. (100 mm) diameter cores (Figure 5.44b). As much as it was practical, the use of water was minimized during coring.

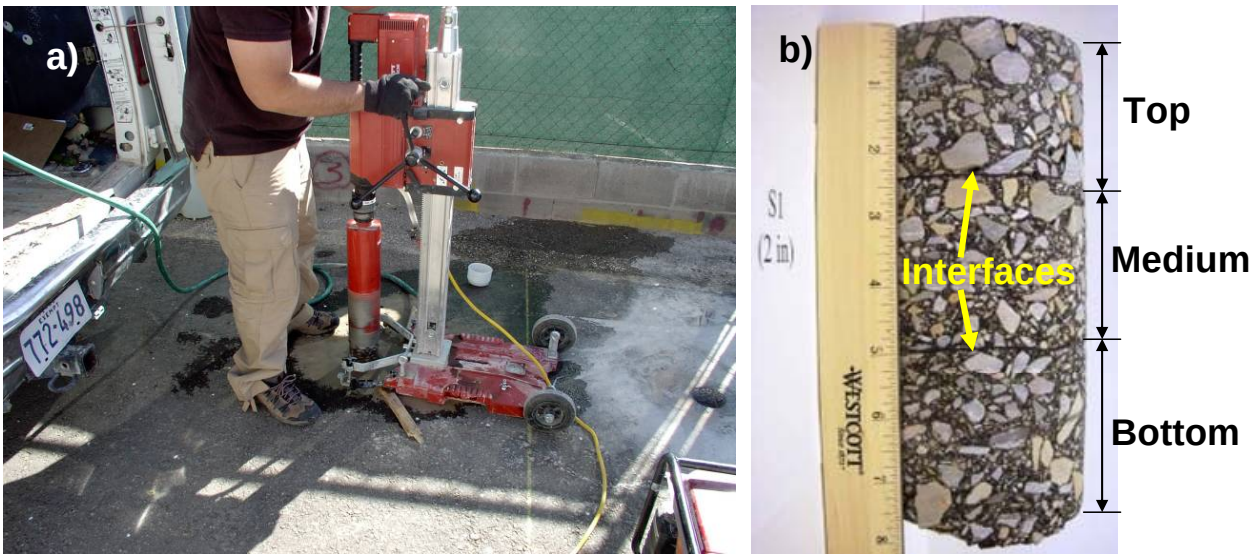

Figure 5.44 – Coring Operations on Controlled Study

Similar to prepared specimens in the lab, direct shear tests were performed to assess the bond strength on the cores. Average shear strengths measured at different layer interfaces are presented on Table 5.4. Detailed results for each core are included in Appendix D. Similar to the laboratory prepared specimens, the highest bond strengths were associated with the tack coat as the bonding agent. The average bond strength for the four specimens with grease as bonding agent was about 40% of the tack coat. However the other specimens, except one with clay slurry, separated after coring operations and were not suitable for testing. In most cases it was difficult to determine whether the coring operation washed the bonding agent or the cores were actually debonded. The bond strengths measured on retrieved intact cores were about twice as much as strengths from the prepared lab specimens (as detailed in Table 4.1). This can be attributed to different compaction methods and the possible negative impact of coring.

Table 5.4 – Summary of Shear Strength Results (psi) for Cores Retrieved

Parameter	Interface at 2.5 inches deep					Interface at 5 inches deep				
	Tack Coat	Grease	Clay Slurry	Talcum Powder	Paper Soaked in Oil	Tack Coat	Grease	Clay Slurry	Talcum Powder	Paper Soaked in Oil
Average	82	41	30	N/A[a]	N/A[a]	84	23	N/A[a]	N/A[a]	N/A[a]
COV, %	17	32	--	--	--	9	14	--	--	--

[a] *Specimens not feasible for shear testing*

CHAPTER 6

VERIFICATION TESTS OF SELECTED NDT METHODS ON CONTROLLED STUDY

Based on the preliminary results presented in Chapter 5, several of the NDT methods were selected for further study. The list of selected NDT methods is presented on Table 6.1. The more extensive study consisted of testing the sections more densely under different environmental conditions. In addition, some of the operational issues were considered. One such issue consisted of the impact of temperature variation on the results. To fulfill this objective, tests were carried out in cool weather when the average surface temperature of HMA ranged from 60ºF to 85ºF (16ºC to 29ºC) and in hot weather when the average HMA surface temperature ranged from 75ºF to 120ºF (24ºC to 49ºC). Even though it would have been desirable to carry out these tests in even colder weather, the climatic condition of El Paso in the previous year did not allow for that.

Table 6.1 – List of NDT Technologies Used on Extended Tests on Controlled Study

Electromagnetic	Impulse		Seismic/Sonic	Thermal
Ground Coupled GPR	FWD	Impulse Response	USW	Thermal Imaging

The other major issue that had to be addressed is the fact that in actual field evaluations, one may not be able to identify an area that is considered intact (like Sections 1 and 6 in our experiments). As such, the entire data set were considered when attempting to delineate the debonded areas.

Location of Test Points

As shown in Figure 6.1, 100 points were evaluated on every section, except for the transition section (between Sections 5 and 6) where 150 points were used. Due to the size of the FWD, every other point along five lines (a total of 25 points) was tested.

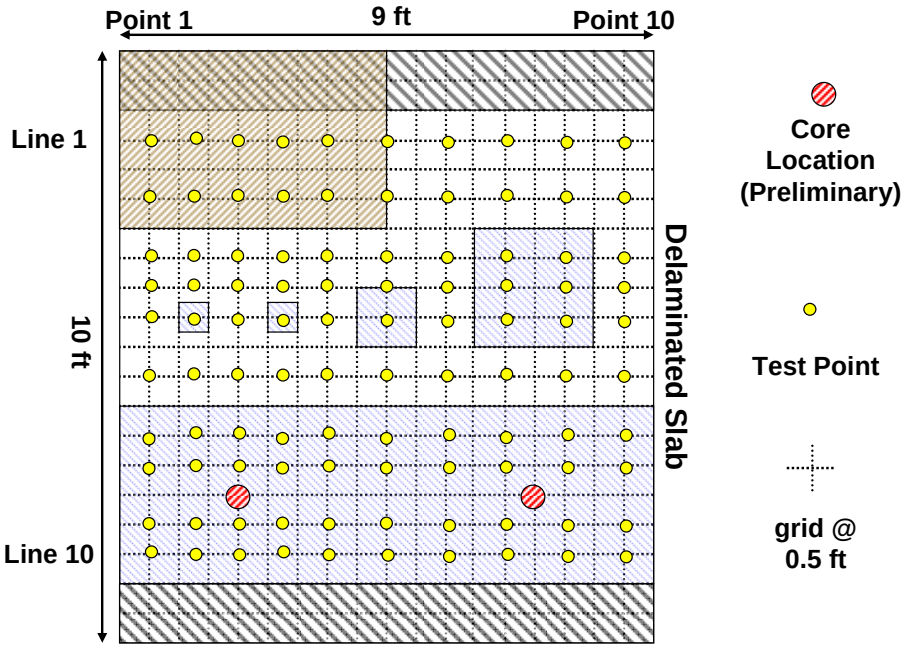

Figure 6.1 – Location of Test Points for a Given Section

Ultrasonic Surface Wave (USW) Method

PSPA was used to conduct USW tests in March (cool weather) and in June (hot weather). The variations in the average moduli for the three HMA lifts along the ten sections are shown in Figure 6.2 for the cool weather tests following the protocol described in Chapter 5. Sections 2 and 3 (shallow partial and low full debonding for the coarse surface mix) generally exhibited lower moduli as anticipated (see Figure 6.2a). Some parts of Section 4 (deep partial debonding) also presented lower moduli, but majority of Section 5 (deep full debonding), exhibited normal moduli. Similar trends are observed for the fine surface mix sections (Figure 6.2b). Most of the shallow and full debonded areas (Sections 7 and 8) exhibited lower moduli but only some on the deep debonded area (Sections 9 and 10). For the case of the small prepared debonded areas, some of the 2 by 2 ft (0.6 m by 0.6 m) areas were detected on the shallow debonded sections, except for Section 2. Almost none of the small deep debonded defects were detected for both mixes. The moduli of the severely debonded areas in the transition zone were substantially less than average as well.

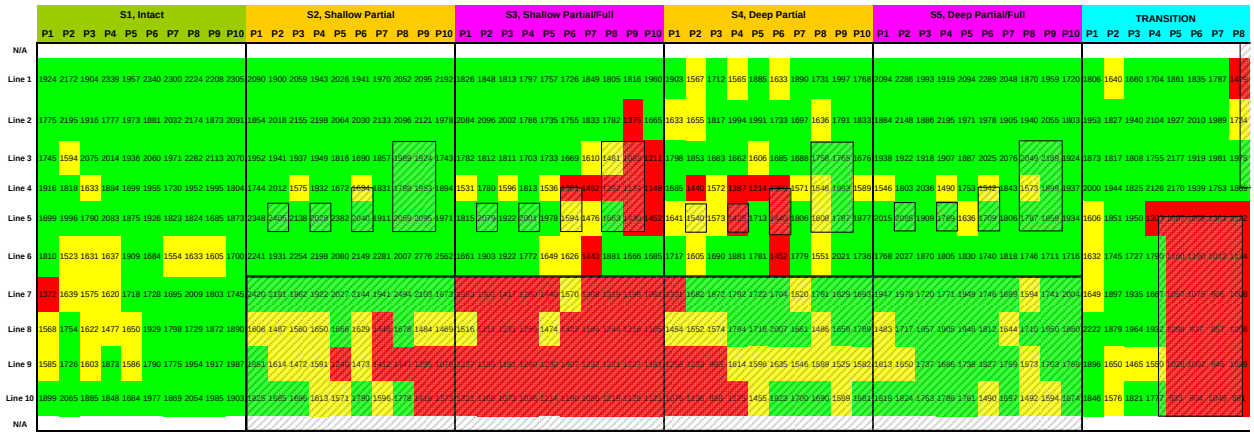

a) Sections 1 to 5

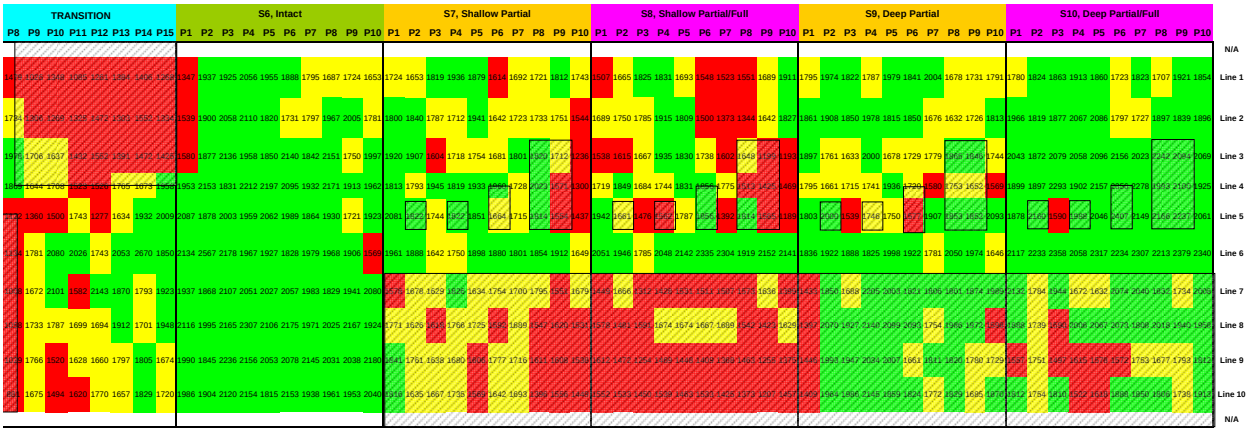

b) Sections 6 to 10

Figure 6.2 – Contour Maps of PSPA Modulus from Extended Tests in Cool Weather

The results from the hot weather tests on the same points as shown in Figure 6.3 are similar to the ones shown in Figure 6.2 for cool weather tests. However, the cool weather tests demonstrated slightly higher resolving power in terms of detecting the debonded areas. This occurs because perhaps during hot temperatures, the bonding agents may provide some additional bonding.

Due to the density of testing, tests started in early morning and continued until late afternoon for several days. To evaluate the impact of the daily temperature fluctuations of 25°F to 45°F (13°C to 25°C) on the seismic moduli of the different mixes, several points were tested repeatedly at different times corresponding to different temperatures. The variations in

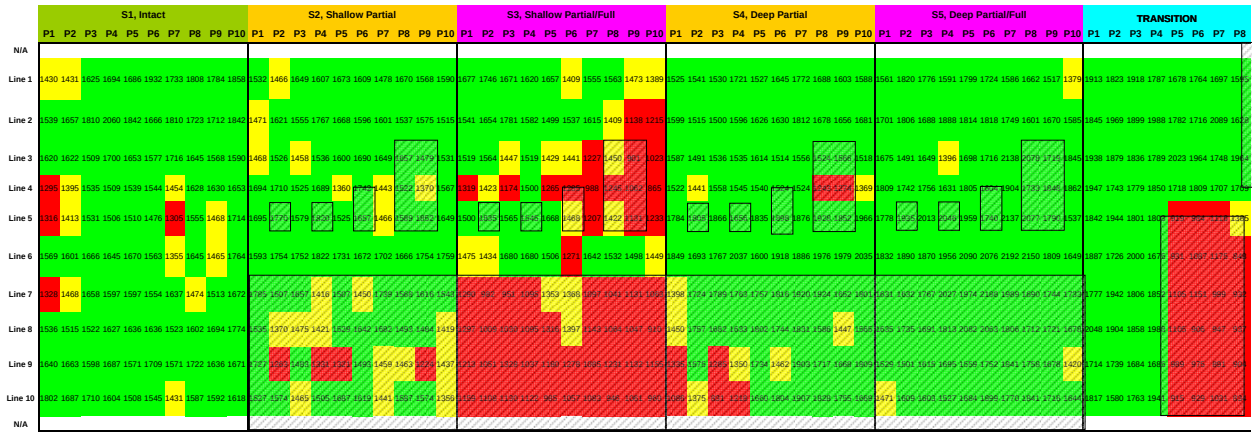

a) Sections 1 to 5

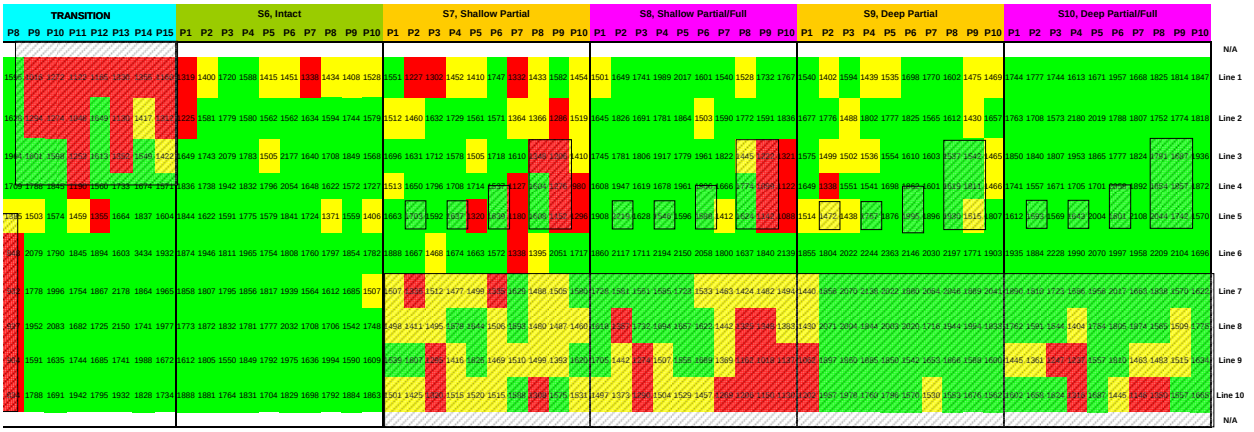

b) Sections 6 to 10

Figure 6.3 – Contour Maps of PSPA Modulus from Extended Tests in Hot Weather

normalized modulus at 77ºF (25ºC) with temperature for Sections 1 and 6 are presented in Figure 6.4. Linear relationships between normalized modulus and temperature were obtained for both sections with reasonably high R^2 values. The general equations to adjust seismic modulus for temperature were:

$$E_{77°F} = \frac{E_{T°F}}{-0.0085 \cdot T + 1.651}, \text{ for surface coarse mixes} \quad (6.1)$$

$$E_{77°F} = \frac{E_{T°F}}{-0.0107 \cdot T + 1.823}, \text{ for surface fine mixes} \quad (6.2)$$

where T is the surface temperature (in ºF) at the time of PSPA tests. These relationships provided slightly greater adjustment to the moduli than Equation 4.1.

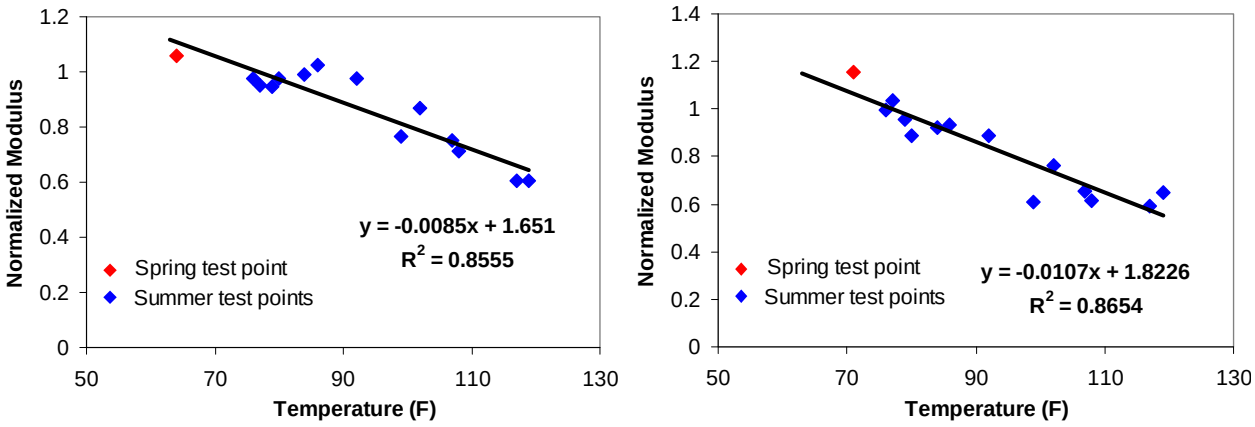

a) Coarse Surface Mix **b) Fine Surface Mix**

Figure 6.4 – Temperature Influence of PSPA Modulus

The results after temperature adjustments with Equations 6.1 and 6.2 are shown in Figures 6.5 and 6.6. The outcomes are in general similar to those in Figures 6.2 and 6.3. For the cool weather data (Figure 6.5), the resolving power for the fine mixes improved for Sections 9 and 10 (corresponding to the deep debonding). On the other hand, the manifestations of the shallow partial debonding are not obvious for Section 7 after temperature adjustment in hot weather testing (Figure 6.6). This activity indicates that the default temperature adjustment in Equation 4.1 is adequate and that the lack of detection of debonding on some of the sections is related to the shortcomings of the method. Also, the development of a temperature-modulus adjustment relationship as part of the protocol for PSPA tests may be desirable.

So far, the evaluation of debonding was based on the average and standard deviation of the control sections (Sections 1 and 6). In the actual field studies, finding control sections may not be practical. To account for this, a revised protocol was considered to account for the variability and uncertainties that may be encountered in actual field sections. The average and standard deviation were again used to delineate the bonded and debonded sections. However, due to significant differences between the properties of the bonded and debonded areas, the level

a) Sections 1 to 5

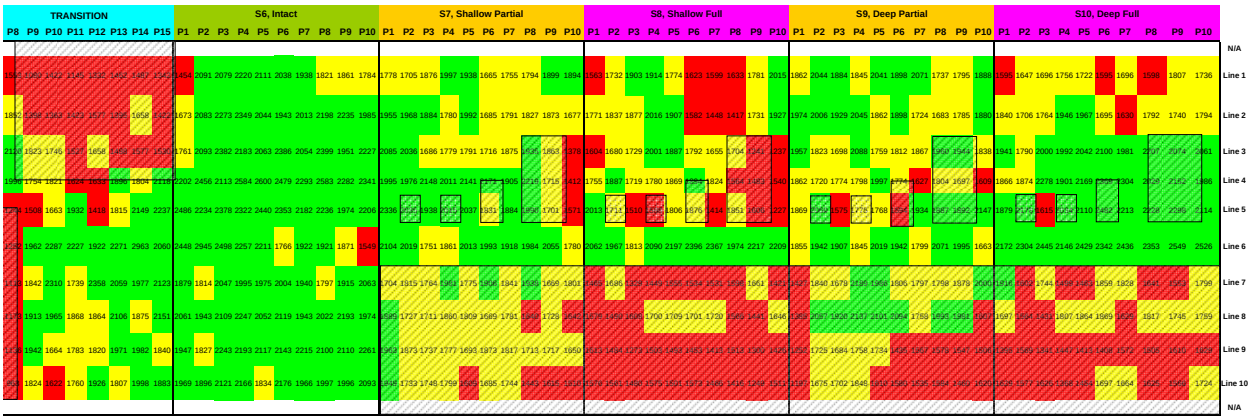

b) Sections 6 to 10

Figure 6.5 – Temperature-Adjusted Contour Maps of PSPA Modulus in Cool Weather

of uncertainty was increased as reflected in Table 6.2. In the revised protocol, one-half and one standard deviation (instead of one and two standard deviations in Table 5.1) were used to evaluate the results.

Based on the revised criteria, color-coded moduli are presented in Figure 6.7 and 6.8. These results are comparable to those in Figures 6.5 and 6.6. From this point forward, the revised criteria will be applied for presenting the results.

The contour plot of average moduli of the top lift (top 2.5 in., 63 mm) for the ten sections tested in cool weather is shown in Figure 6.9. Reduced moduli were observed particularly for Sections 3 and 8 (shallow and full debonding). Sections with shallow and partial debonding also

a) Sections 1 to 5

b) Sections 6 to 10

Figure 6.6 – Temperature-Adjusted Contour Maps of PSPA Modulus in Hot Weather

showed some reduction in moduli. This pattern indicates that the quality of the HMA layer (in terms of stiffness) may be compromised when the two adjacent layers are not bonded.

Table 6.2 – Revised Criteria Used to Analyze Moduli

Color Code	Modulus Value	Interpretation
Green	$E > E_{control} - \frac{1}{2}\,\sigma_{control}$	Measured modulus is similar or higher than modulus from control section
Yellow	$E_{control} - \frac{1}{2}\,\sigma_{control} > E > E_{control} - \sigma_{control}$	Measured modulus is somewhat less than control modulus
Red	$E < E_{control} - \sigma_{control}$	Measured modulus is substantially less than control modulus

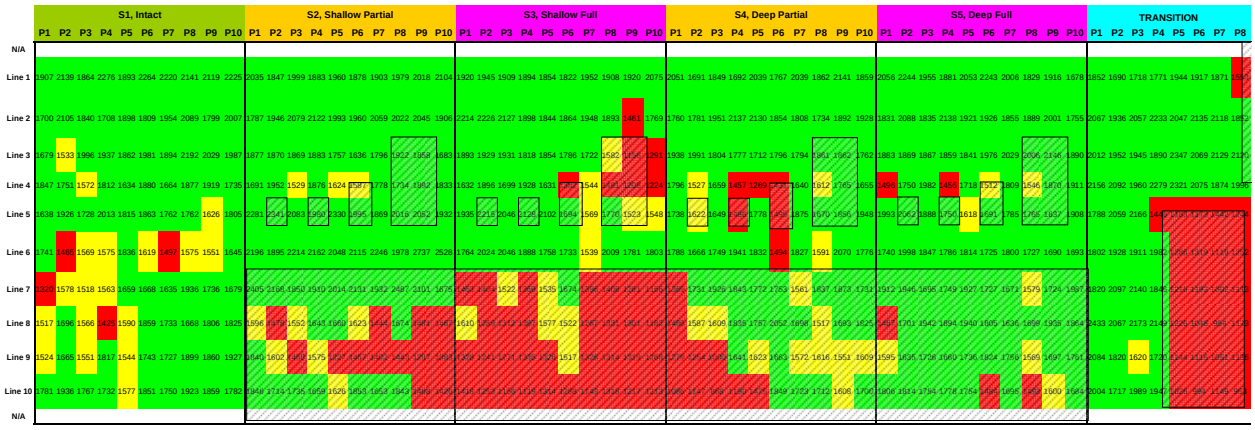

a) Sections 1 to 5

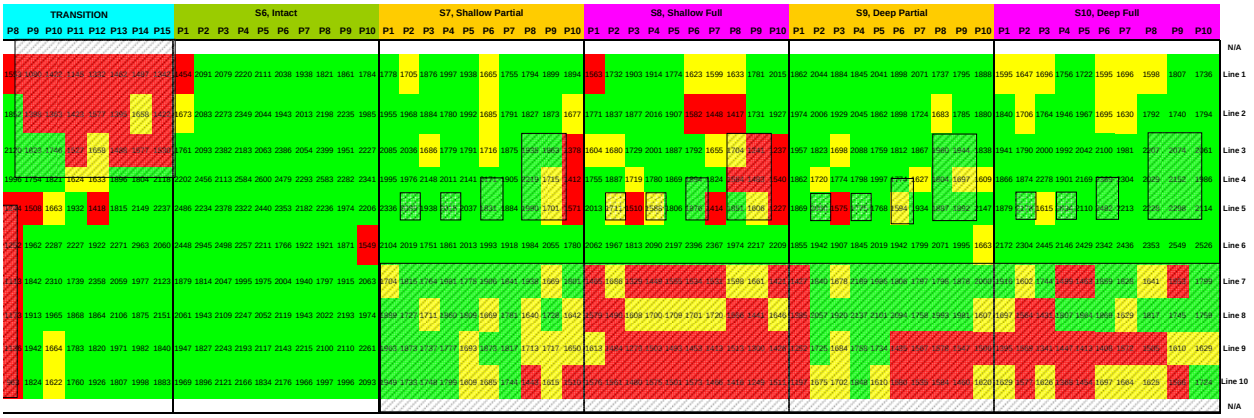

b) Sections 6 to 10

Figure 6.7 – Temperature-Adjusted Contour Maps of PSPA Modulus in Cool Weather based on Revised Statistical Criteria

Contour plots of the dispersion curves (analogous to the variation in modulus with depth) are included in Figure 6.10 for the ten lines tested along all sections during the cool weather. The depths and the extent of the debonding areas are also depicted in the figures, where solid lines correspond to full debonding and the dashed lines to partial debonding. Please note that not all cross-sections contained debonded areas. A reduction in modulus can be observed in most debonded sections at or below the depth of defects, confirming the usefulness of the USW method in identifying at least the fully debonded areas. One complicating (but perhaps beneficial) aspect of the dispersion curve is that a low-quality but bonded lift may exhibit the same patterns in a dispersion curve than a partially debonded interface. Once again, similar conclusions can be drawn from data collected during the hot weather as detailed in Appendix E.

a) Sections 1 to 5

b) Sections 6 to 10

Figure 6 8 – Temperature-Adjusted Contour Maps of PSPA Modulus in hot Weather based on Revised Statistical Criteria

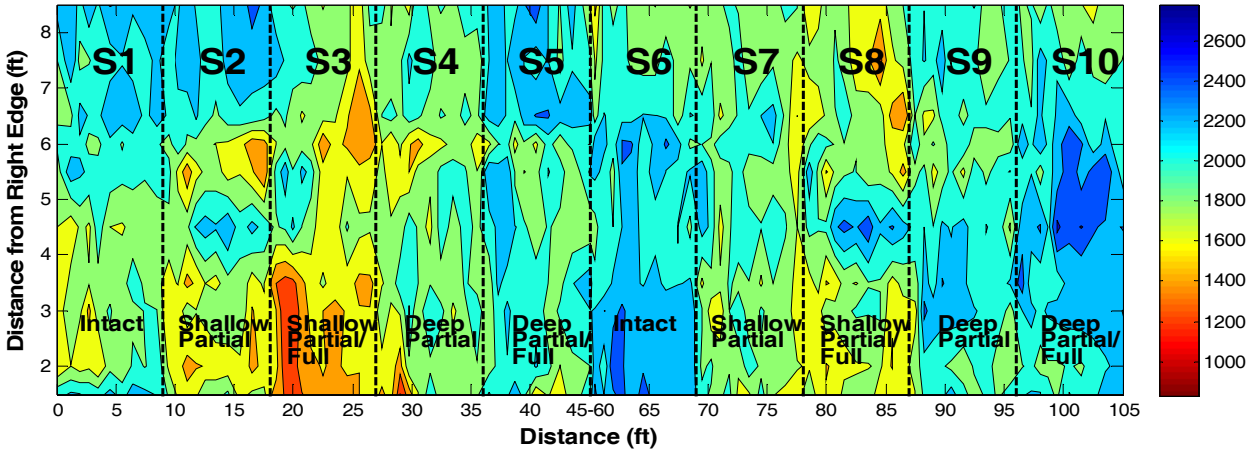

Figure 6.9 – Modulus Contour Plot of Top 2.5 in. from Cool Weather Tests

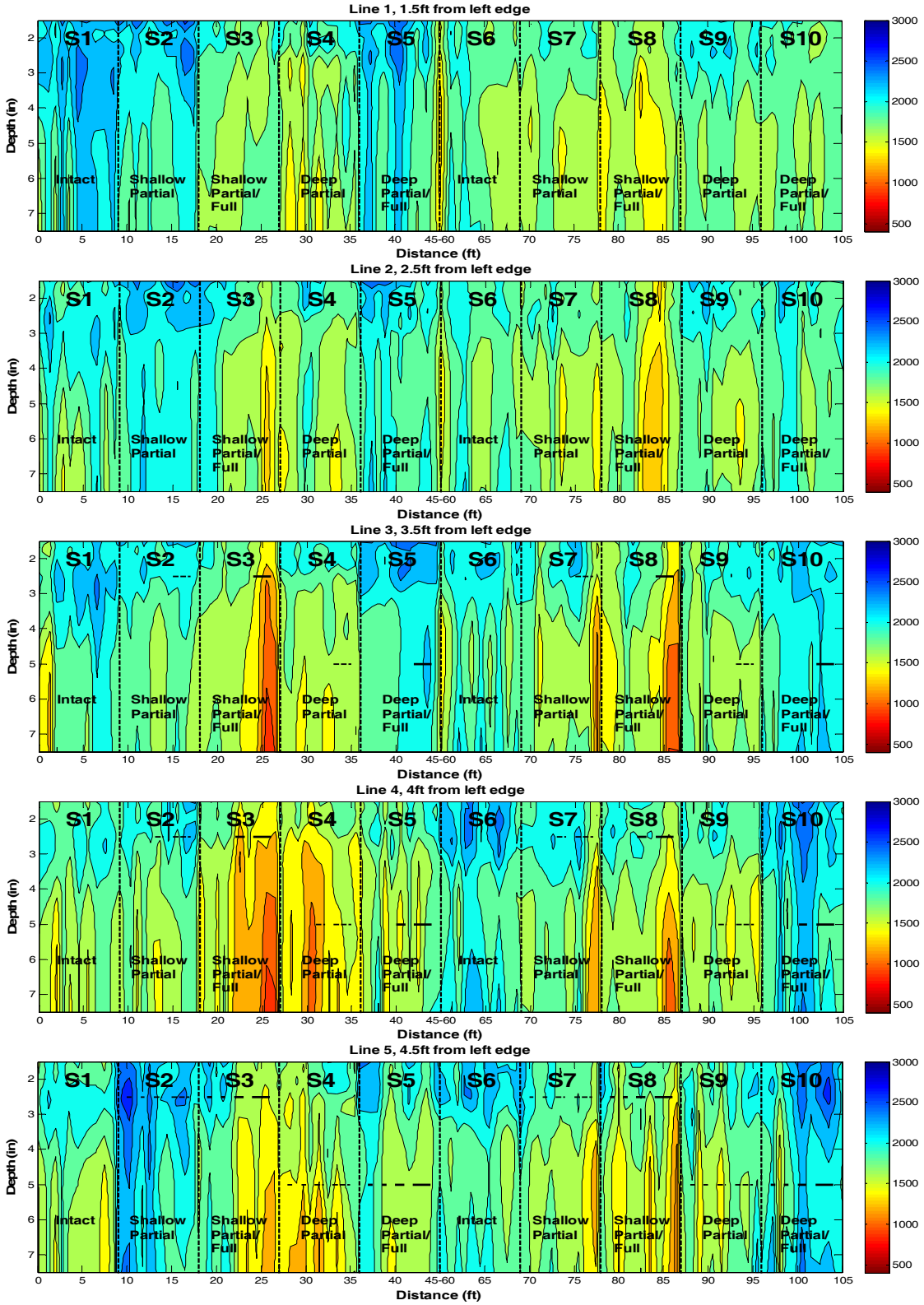

Figure 6.10 – Dispersion Curve Contour Plots for Cool Weather

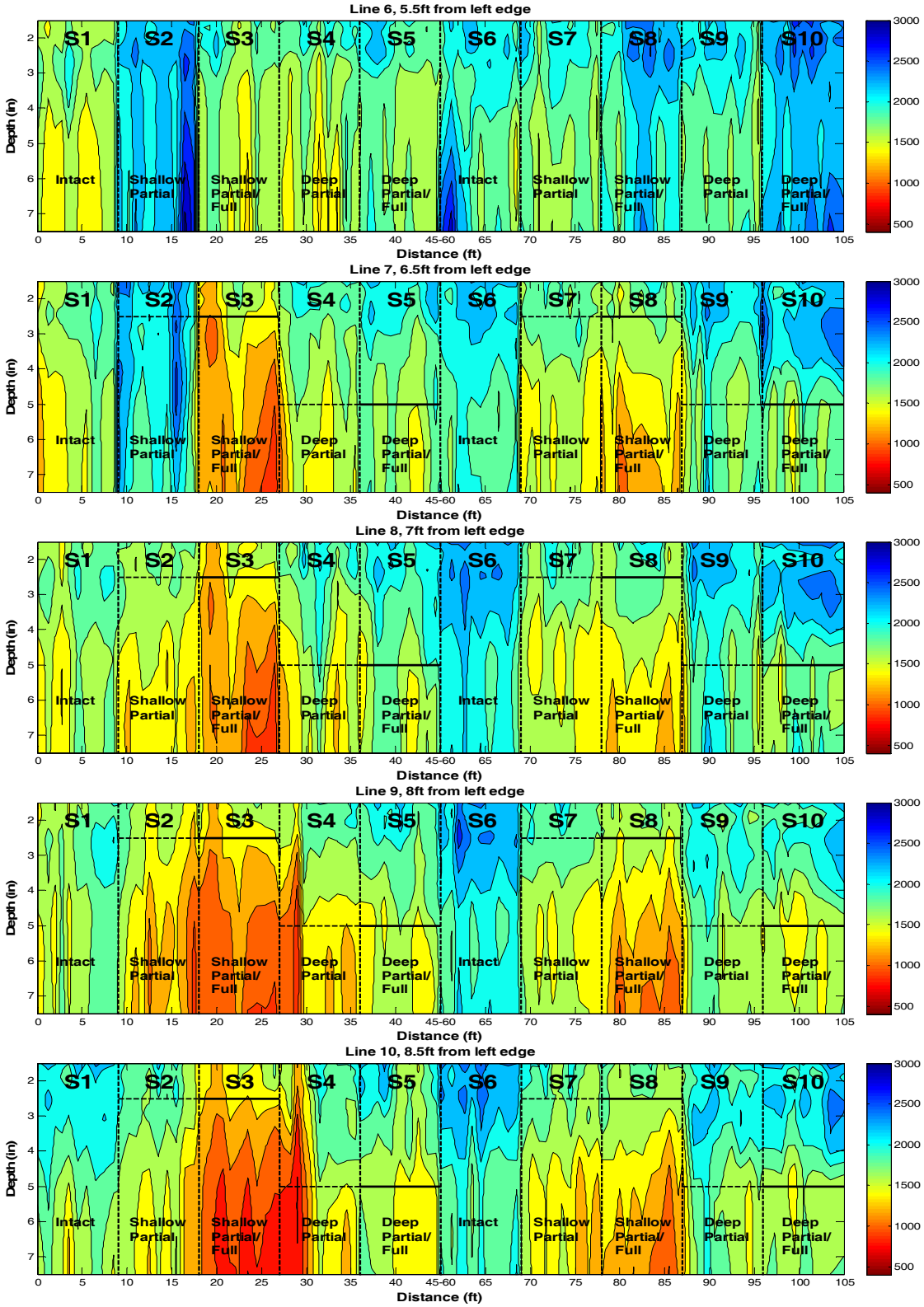

Figure 6.10 Contd. – Dispersion Curve Contour Plots for Cool Weather

Falling Weight Deflectometer (FWD)

The FWD tests were carried out on 25 points on each section (40 on the transition) again in the cool and hot temperatures. The variation in the deflections along the ten sections is shown in Figure 6.11 for the cool weather testing. As a reminder, the criteria presented in Table 6.2 were used to color code the graphs. Almost all of the shallow fully-debonded locations are detected as they exhibited higher than average deflections. Most shallow partially-debonded locations are also detected. However, almost all deep debonded areas exhibit similar deflections to the intact areas. One of the concerns with these results is that some areas in the intact sections are categorized as debonded, and the severely debonded area in the transition is not detected.

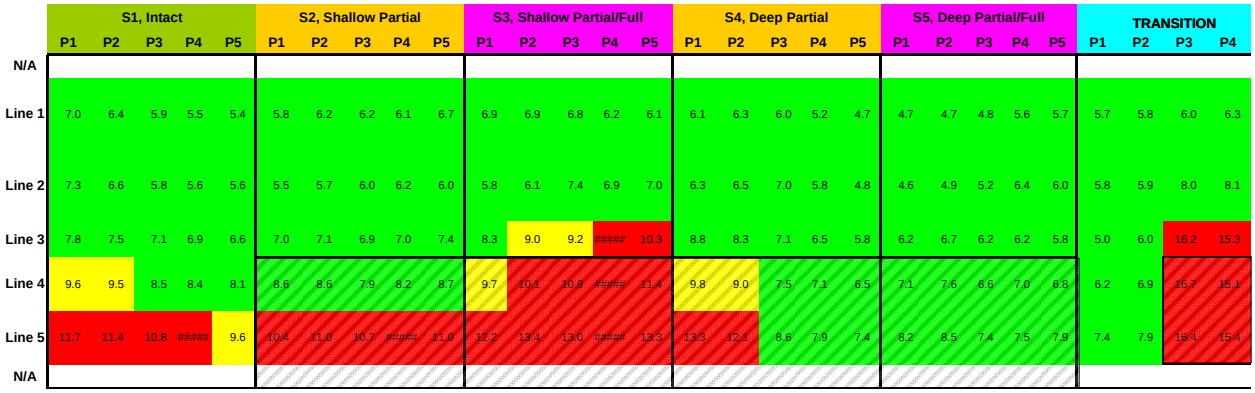

a) Sections 1 to 5

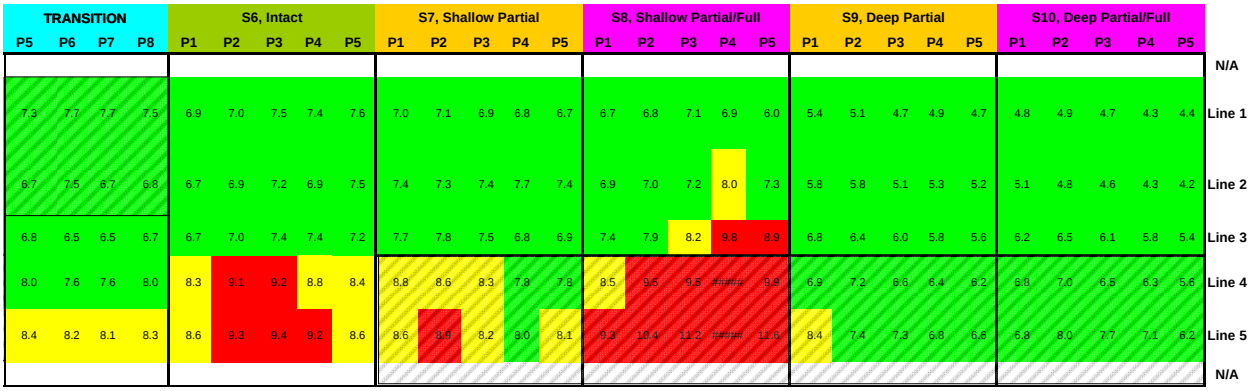

a) Sections 6 to 10

Figure 6.11 – Contour Maps of FWD Deflection in Cool Weather based on Revised Statistical Criteria

The outcomes from the hot weather testing (Figure 6.12) are rather different. The resolving power of the method in detecting debonding is diminished for most debonded sections, while the debonding in Sections 9 and 10 is now apparent. The false positive results (exhibiting the sign of debonding on an intact point) in the intact sections are less severe, but they now show up in Sections 2, 3, 7 and 8.

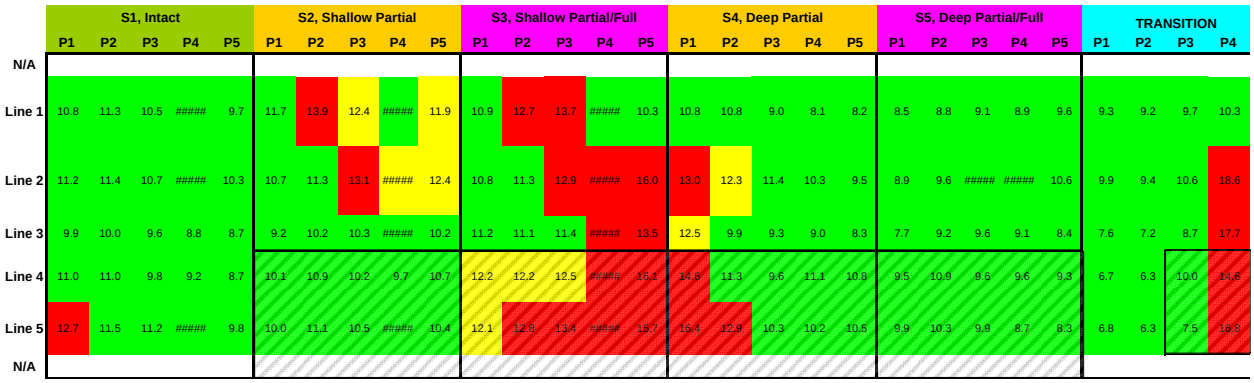

a) Sections 1 to 5

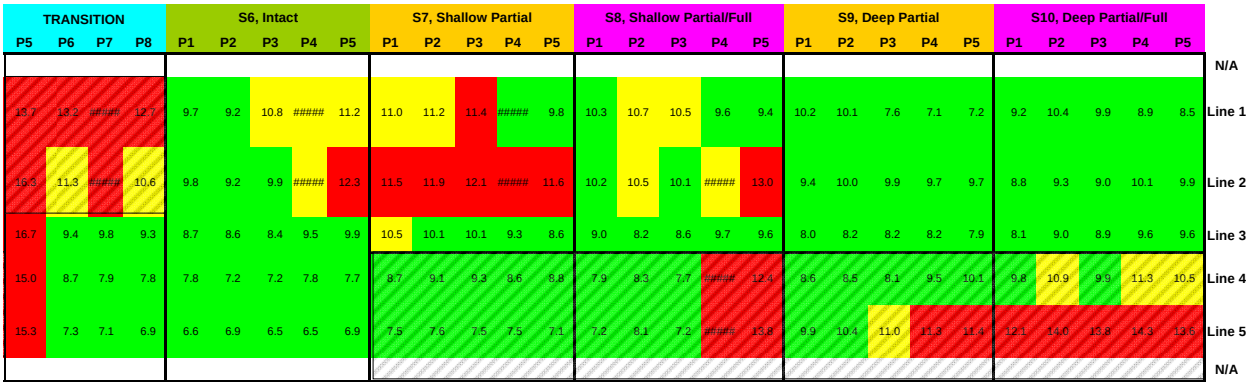

a) Sections 6 to 10

Figure 6.12 – Contour Maps of FWD Deflection in Hot Weather based on Revised Statistical Criteria

One possible explanation for the trends observed with the FWD deflections can be the lack of temperature adjustment. Similar to the USW tests, several points were tested repeatedly at different times corresponding to different temperatures. The variations in normalized deflections at 77ºF (25ºC) with temperature for Sections 1 and 6 are presented in Figure 6.13 and the general equations to adjust deflections are presented in the following equations:

$$D_{77°F} = \frac{D_{T°F}}{0.0062 \cdot T + 0.5018}, \text{ for surface coarse mixes} \quad (6.3)$$

$$D_{77°F} = \frac{D_{T°F}}{0.0073 \cdot T + 0.4127}, \text{ for surface fine mixes} \quad (6.4)$$

where D denotes deflection and T is the temperature (in ºF) at the time of FWD tests. The slopes of the lines are rather flat indicating that the change in deflection with temperature is small. This pattern is anticipated since the majority of the deflection measured with the FWD comes from the deformation of the subgrade.

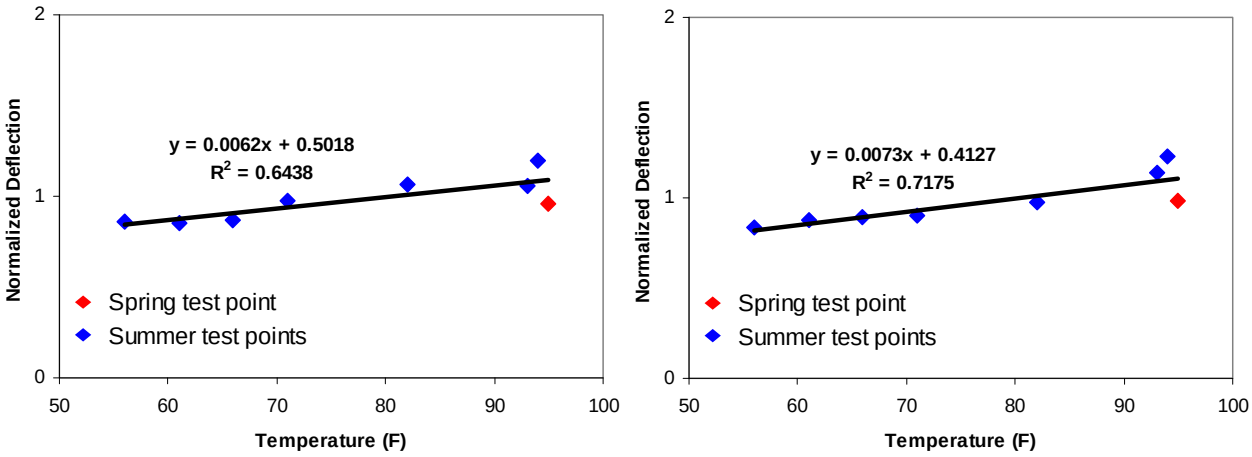

a) Coarse Surface Mix **b) Fine Surface Mix**

Figure 6.13 – Temperature Influence on FWD Deflection

The results after temperature adjustments with Equations 6.3 and 6.4 are shown in Figures 6.14 and 6.15 for the cool and hot weather tests. The patterns in the variations in deflections in these figures are quite similar to the corresponding ones before temperature adjustments (Figures 6.11 and 6.12).

Since the FWD deflections are strongly influenced by the modulus of the subgrade, the next step was to test the variation in the HMA modulus as a means of detecting debonded areas. HMA moduli were backcalculated using MODULUS 6.0 software (Liu and Scullion, 2001). To

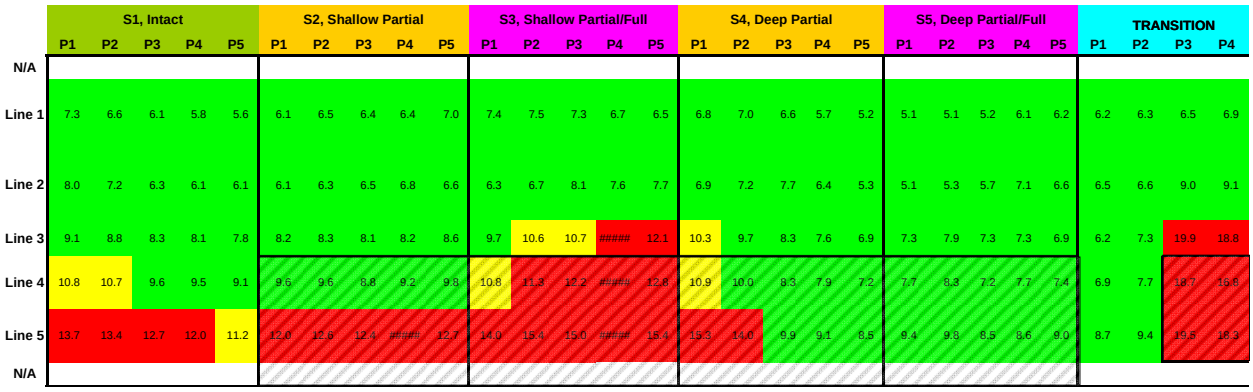

a) Sections 1 to 5

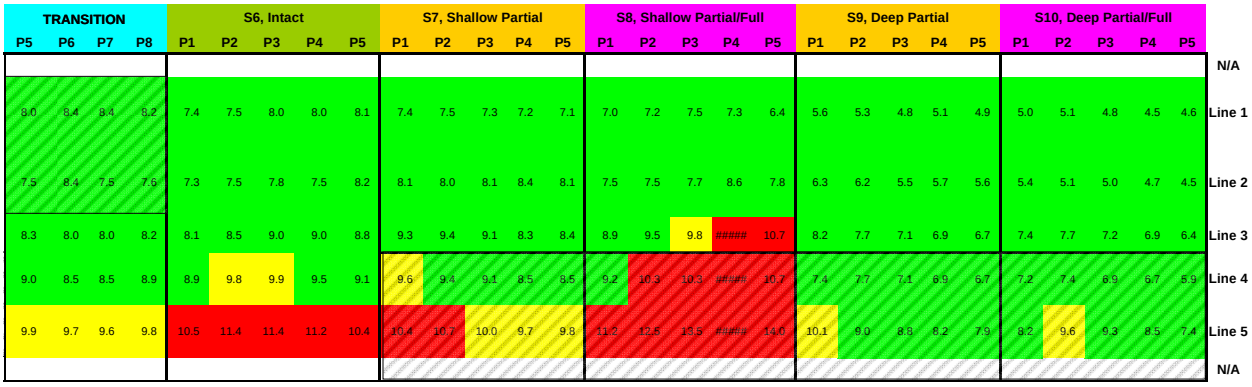

a) Sections 6 to 10

Figure 6.14 – Temperature-Adjusted Contour Maps of FWD Deflection in Cool Weather based on Revised Statistical Criteria

minimize the uncertainty in the backcalculation process, a 2-layer analysis that considered the entire HMA thickness (8 in., 200 mm) as one layer over a subgrade was used. Asphalt moduli before temperature adjustments are shown in Figures 6.16 and Figure 6.17 for the cool and hot weather testing, respectively. For the cool weather testing (Figure 6.16), the two intact sections (Sections 1 and 6) now exhibit normal moduli, and the resolving power of the method for detecting the debonded areas is somewhat improved. These improvements are not evident for the hot weather testing as reflected in Figure 6.17.

The variations in normalized modulus at 77ºF (25ºC) with temperature for Sections 1 and 6 are presented in Figure 6.18. The general equations to adjust moduli are:

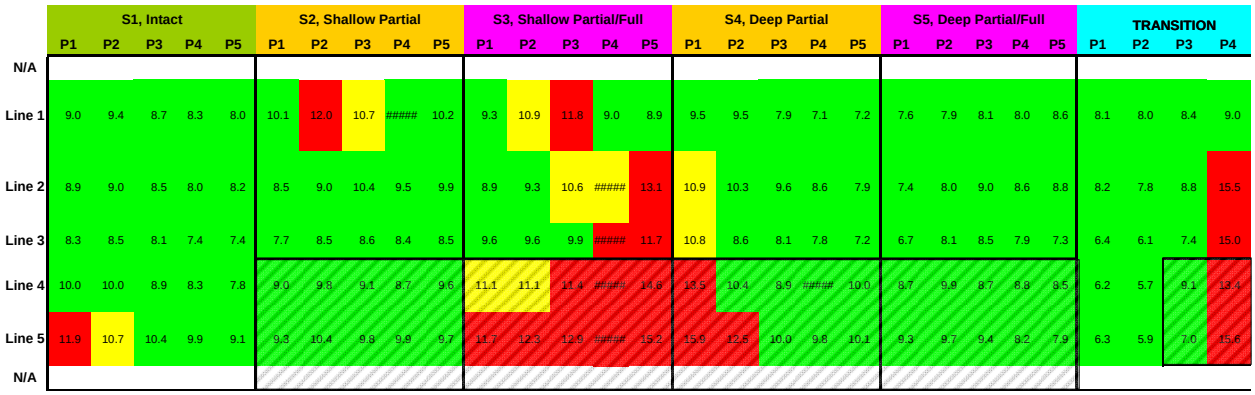

a) Sections 1 to 5

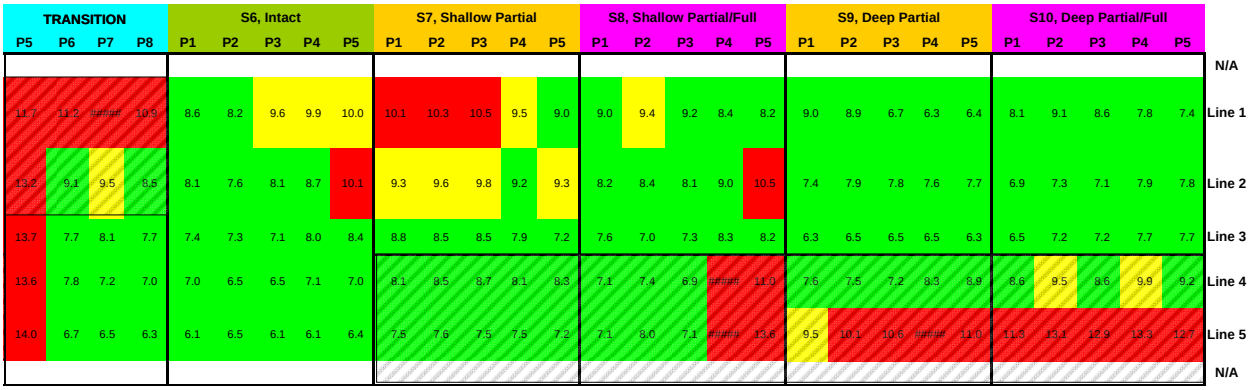

a) Sections 6 to 10

Figure 6.15 – Temperature-Adjusted Contour Maps of FWD Deflection in Hot Weather based on Revised Statistical Criteria

$$E_{77^\circ F} = \frac{E_{T^\circ F}}{-1.8144 \cdot Ln(T) + 8.8812}, \text{ for surface coarse mixes} \quad (6.5)$$

$$E_{77^\circ F} = \frac{E_{T^\circ F}}{-1.8218 \cdot Ln(T) + 8.9098}, \text{ for surface fine mixes} \quad (6.6)$$

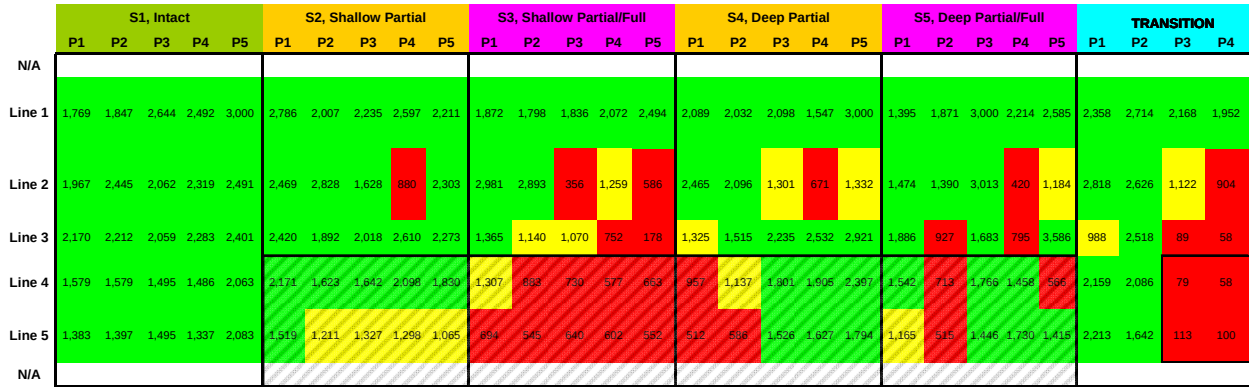

a) Sections 1 to 5

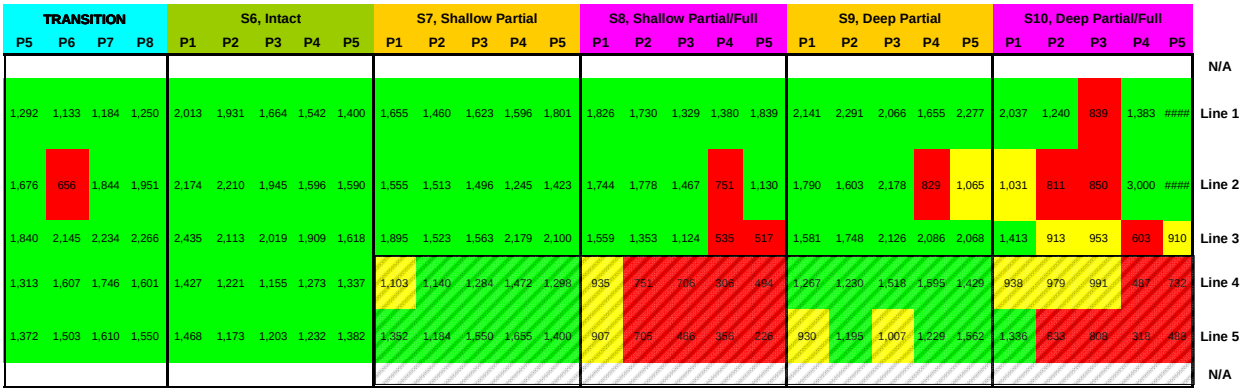

a) Sections 6 to 10

Figure 6.16 – Contour Maps of FWD Moduli in Cool Weather based on Revised Statistical Criteria

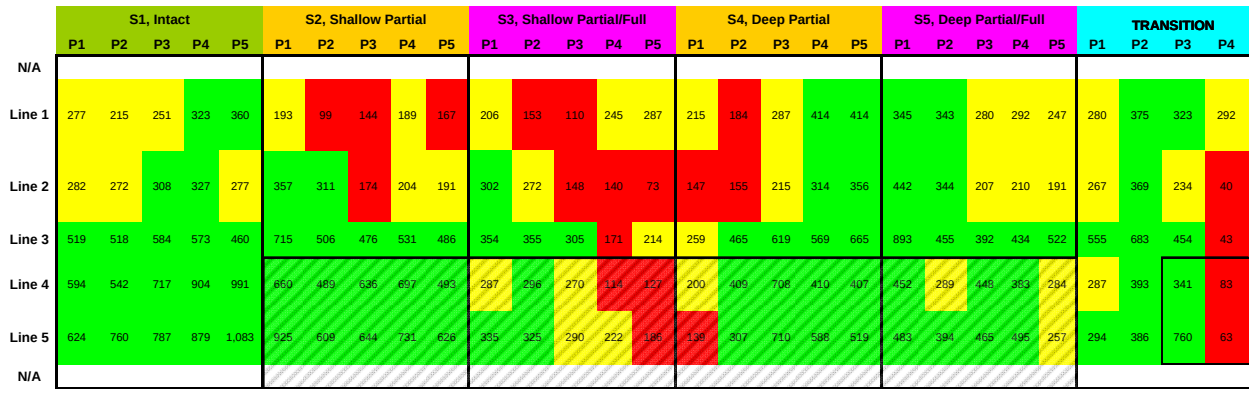

a) Sections 1 to 5

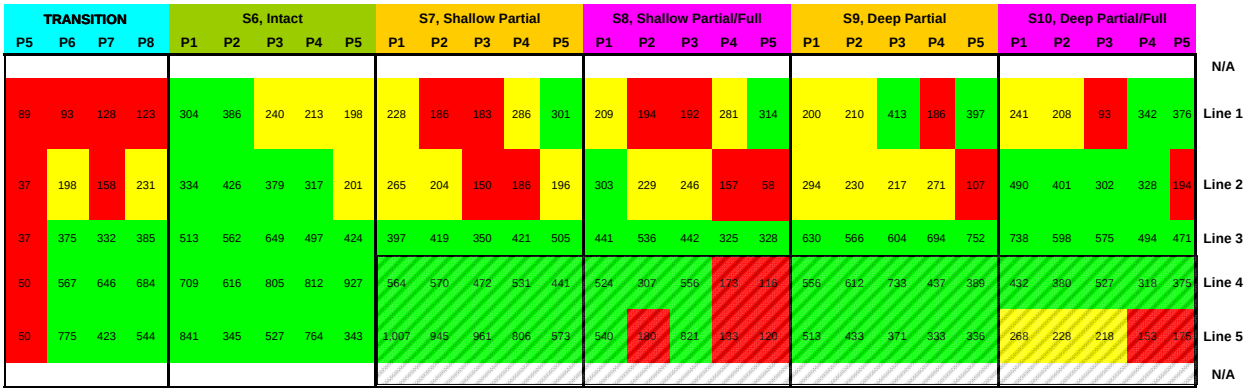

a) Sections 6 to 10

Figure 6.17 – Contour Maps of FWD Moduli in Hot Weather based on Revised Statistical Criteria

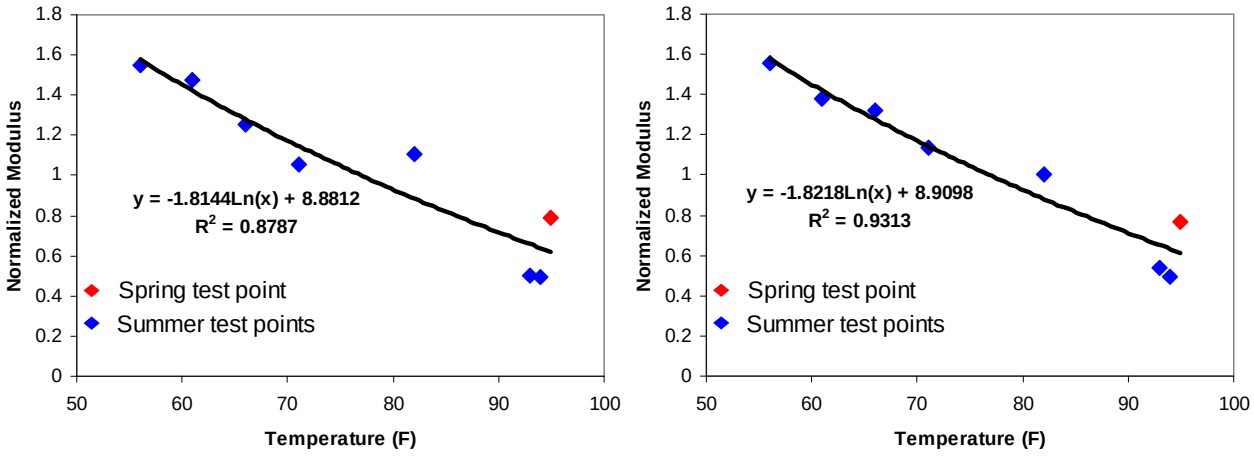

a) Coarse Surface Mix b) Fine Surface Mix

Figure 6.18 – Temperature Influence of FWD Modulus on Controlled Study

The temperature adjusted modulus contour maps are shown in Figures 6.19 and 6.20. Slight improvements in delineating debonded area are observed due to temperature adjustment. However, the number of false positive readings increased, especially for the hot weather tests.

Based on this study, the FWD may be used for detecting the shallow fully-debonded area, and with less certainty partially-debonded area. Similar to the USW method, the FWD is more effective in the cool weather testing than the hot weather testing. One concern with the FWD is the number of false positive readings (estimating low modulus for intact point) especially during the hot temperature testing. This pattern was not observed in the initial testing reported in Chapter 5.

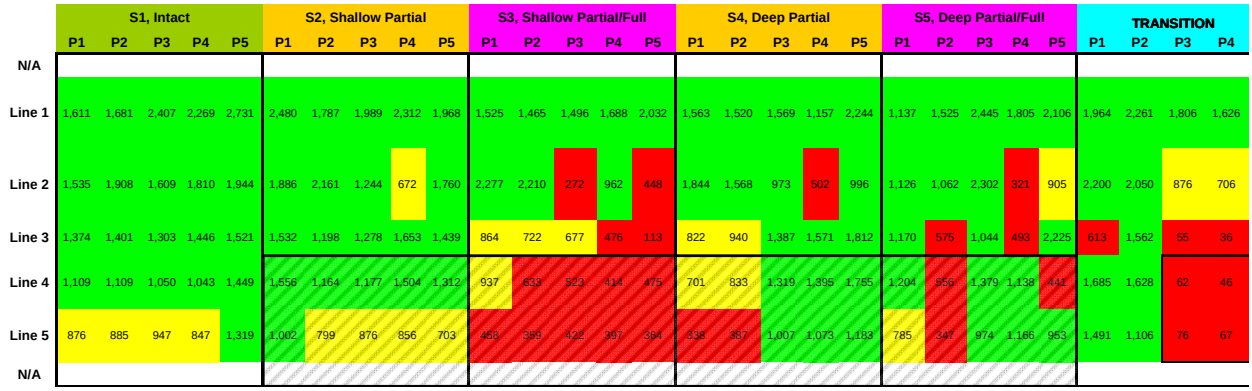

a) Sections 1 to 5

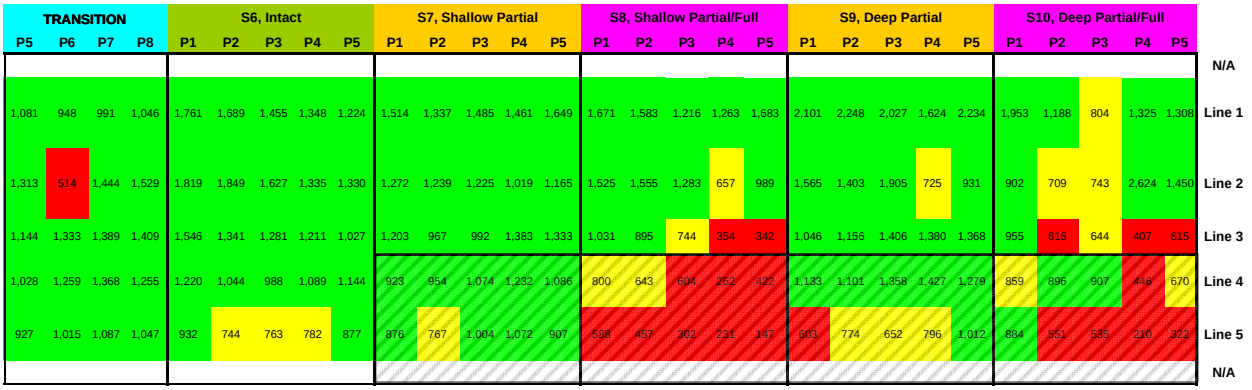

a) Sections 6 to 10

Figure 6.19 – Temperature-Adjusted Contour Maps of FWD Moduli in Cool Weather based on Revised Statistical Criteria

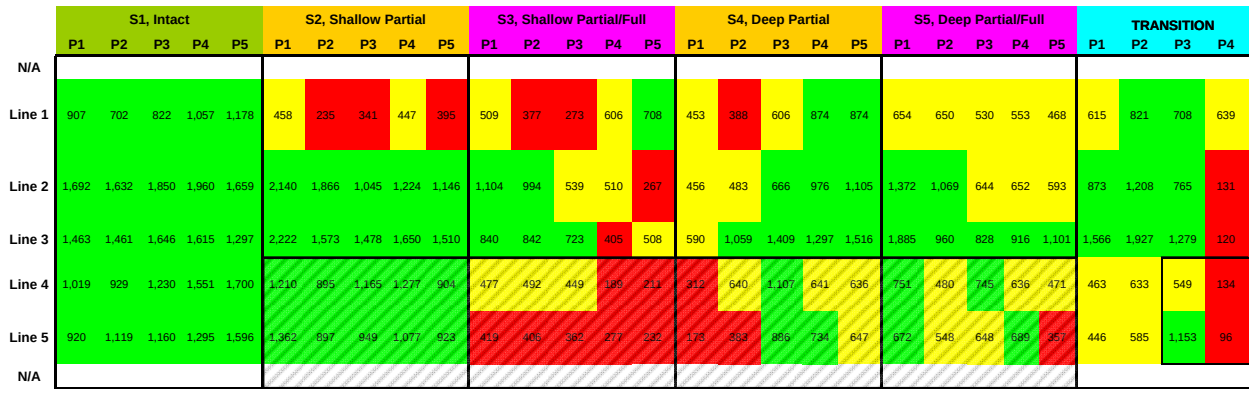

a) Sections 1 to 5

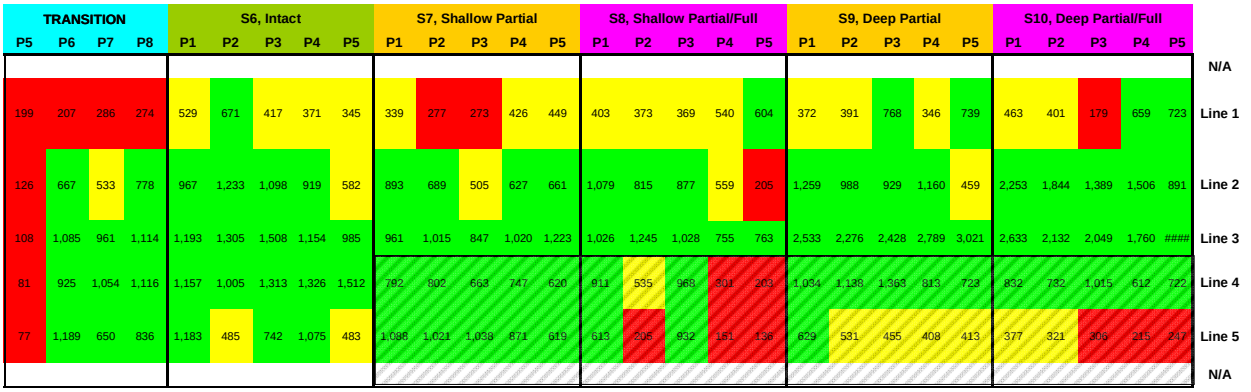

a) Sections 6 to 10

Figure 6.20 – Temperature-Adjusted Contour Maps of FWD Moduli in Hot Weather based on Revised Statistical Criteria

Impulse Response

The results from the IR tests for the cool weather testing are summarized in Figure 6.21. Most of the shallow fully-debonded areas on Sections 3 and 8 were identified, but not all of the deep fully-debonded points are picked up. Interestingly, the shallow partially-debonded areas exhibit normal values, whereas the majority of the deep partially-debonded points are either marginally or significantly less stiff. Also, even though all the points in the control Section 1 are categorized as intact, a majority of test points on control Section 6 exhibit false positive results.

For hot weather tests, as shown in Figure 6.22, most defects are identified except those in Sections 5 and 7. Similar to FWD, a number of false positive points are apparent (i.e., a number intact points exhibited flexibility that are higher than average).

Hoping that considering the impact of temperature may assist in improving the interpretation of the results, the temperature adjustments shown in Figure 6.23 were developed similar to the other methods. The general equations for this purpose are the following:

$$FFT_{77°F} = \frac{FFT_{T°F}}{-0.009 \cdot T + 1.6958}, \text{ for surface coarse mixes} \tag{6.7}$$

$$FFT_{77°F} = \frac{FFT_{T°F}}{-0.009 \cdot T + 1.6876}, \text{ for surface fine mixes} \tag{6.8}$$

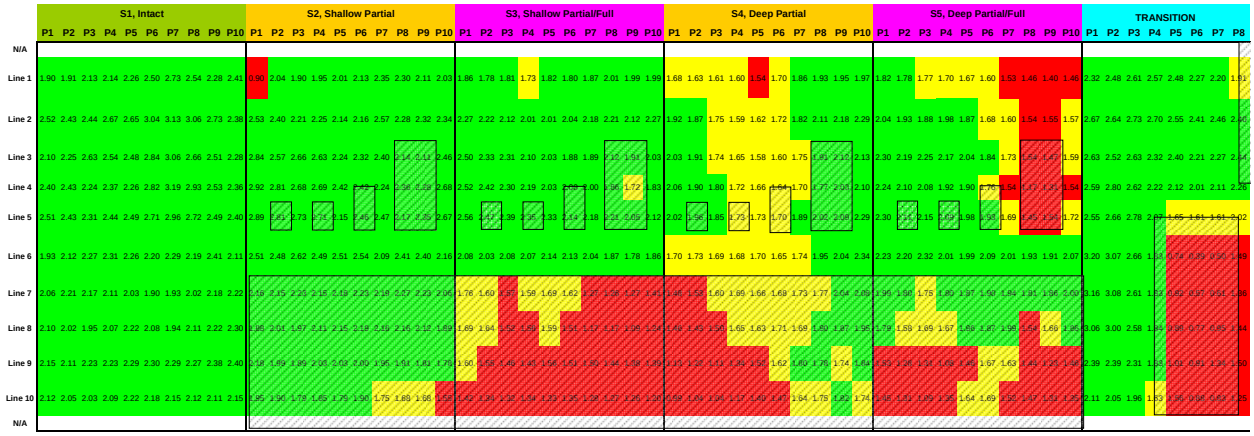

a) Sections 1 to 5

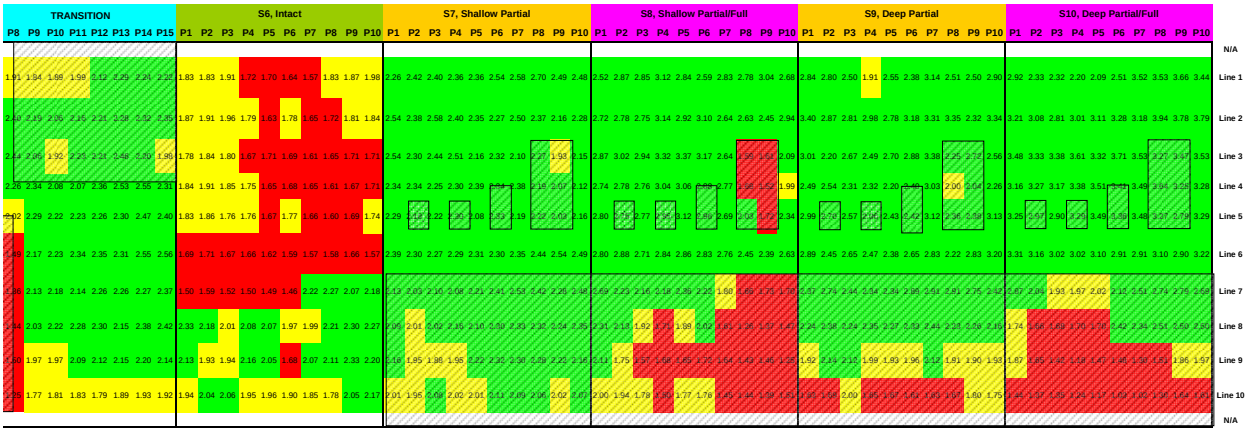

a) Sections 6 to 10

Figure 6.21 – Contour Maps of IR Flexibility in Cool Weather based on Revised Statistical Criteria

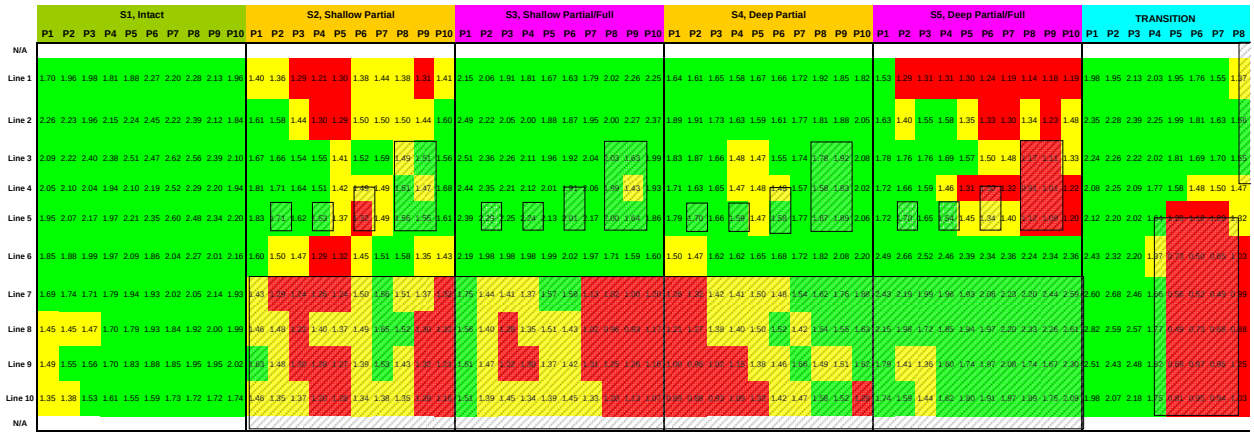

a) Sections 1 to 5

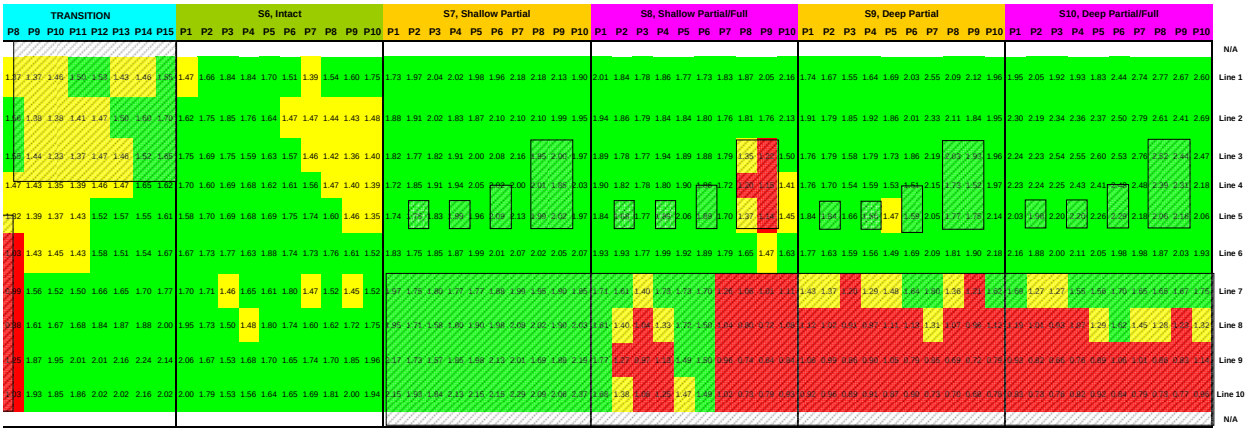

a) Sections 6 to 10

Figure 6.22 – Contour Maps of IR Flexibility in Hot Weather based on Revised Statistical Criteria

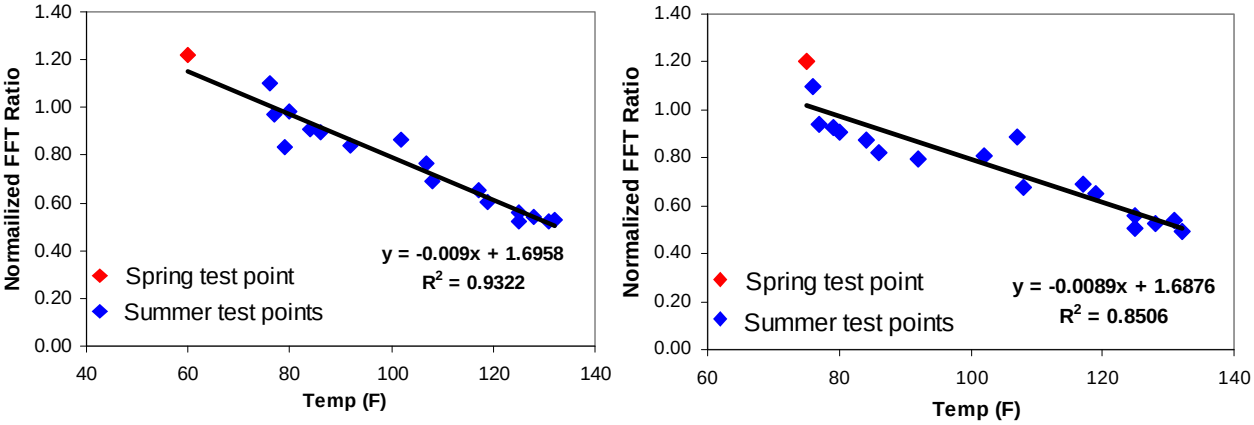

a) Coarse Surface Mix **b) Fine Surface Mix**

Figure 6.23 – Influence of Temperature on IR Flexibility

As reflected in Figure 6.24, the temperature adjustment of the results for cool weather tests marginally improved the predictive power of the method and significantly reduced the number of false positive points. Similar conclusions can be drawn for the hot weather tests (Figure 6.25).

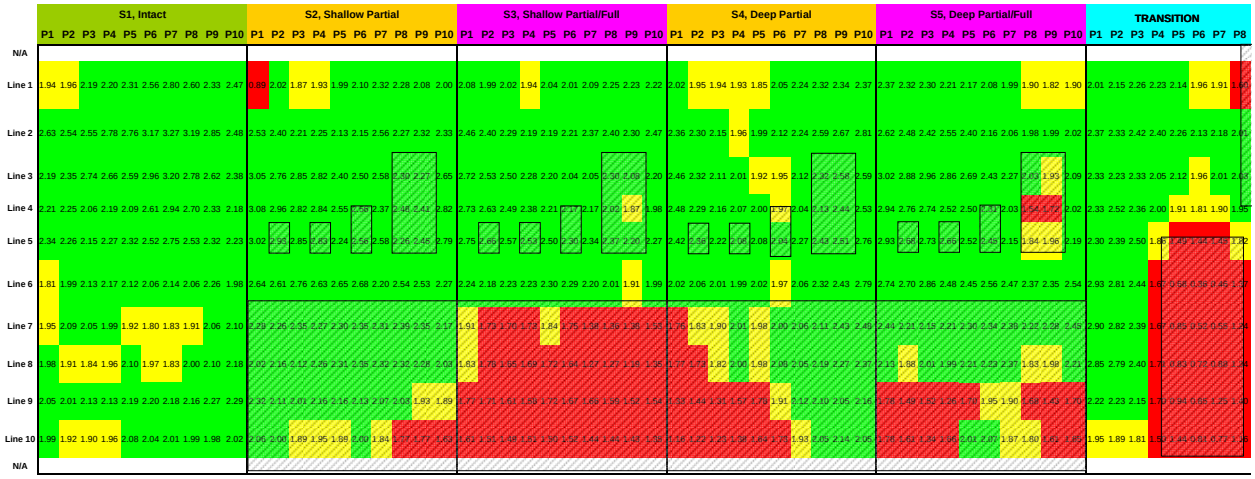

a) Sections 1 to 5

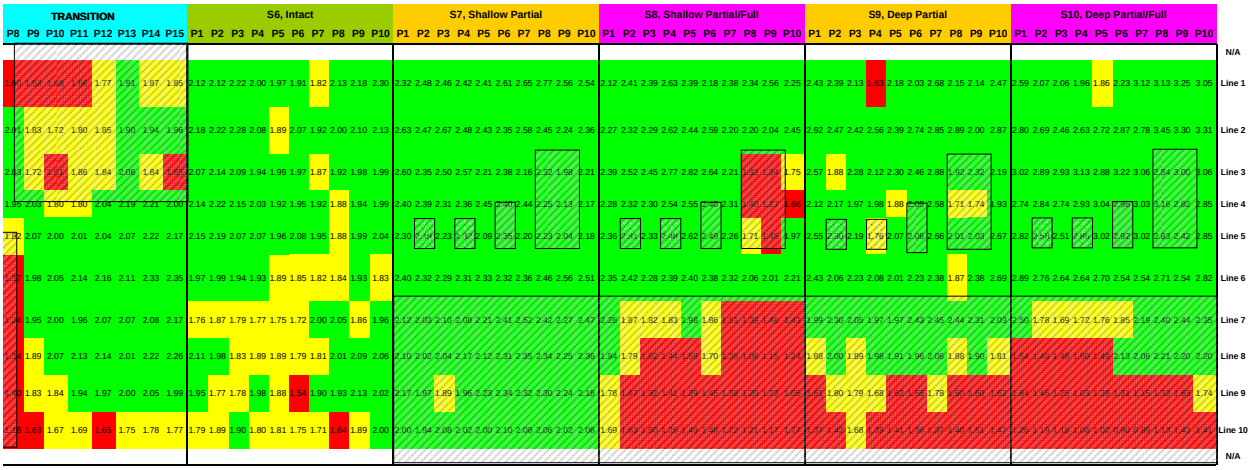

a) Sections 6 to 10

Figure 6.24 – Temperature-Adjusted Contour Maps of IR Flexibility in Cool Weather based on Revised Statistical Criteria

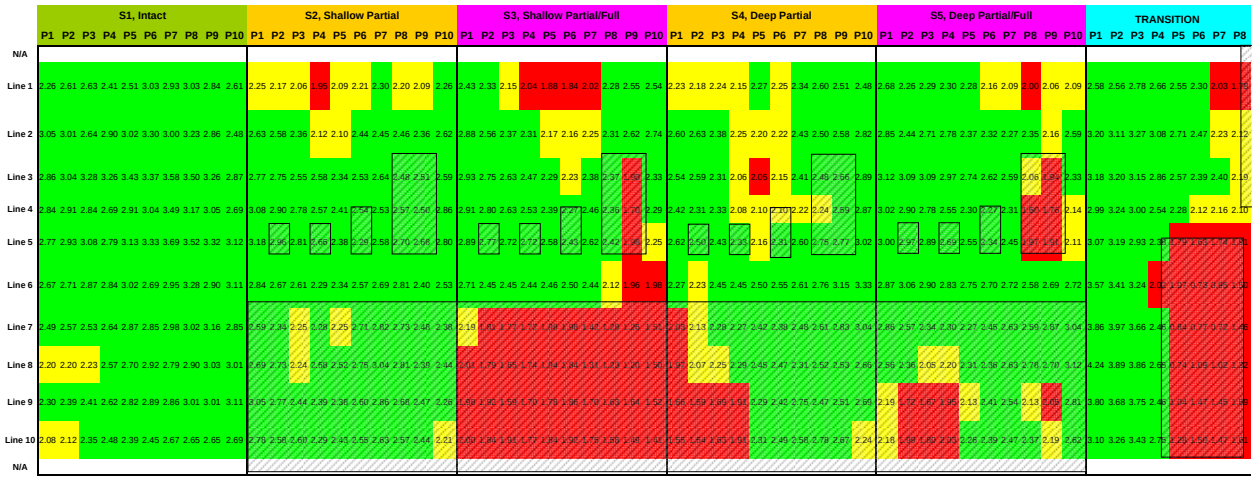

a) Sections 1 to 5

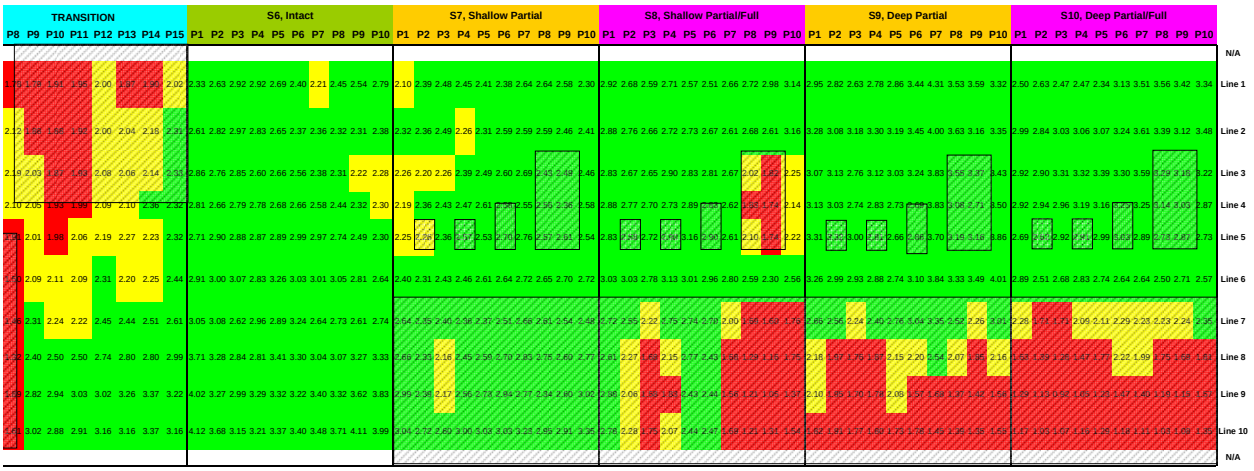

a) Sections 6 to 10

Figure 6.25 – Temperature-Adjusted Contour Maps of IR Flexibility in Cool Weather based on Revised Statistical Criteria

Thermal Methods

The thermal imaging was not deemed successful in Chapter 5. One concern with the earlier survey was the resolution of the camera. A more sensitive camera (a ToughCam Pro from Infrared Cameras Inc.) was acquired and used to reevaluate the thermal method as shown in Figure 6.26. A study was conducted on the transition section to evaluate the feasibility of the more sensitive camera. A total of 120 pictures were obtained, each one covering an area of 1by 1 ft approximately. The combination of all the pictures is presented in Figure 6.27. Areas of

Figure 6.26 – Infrared Camera on Controlled Study

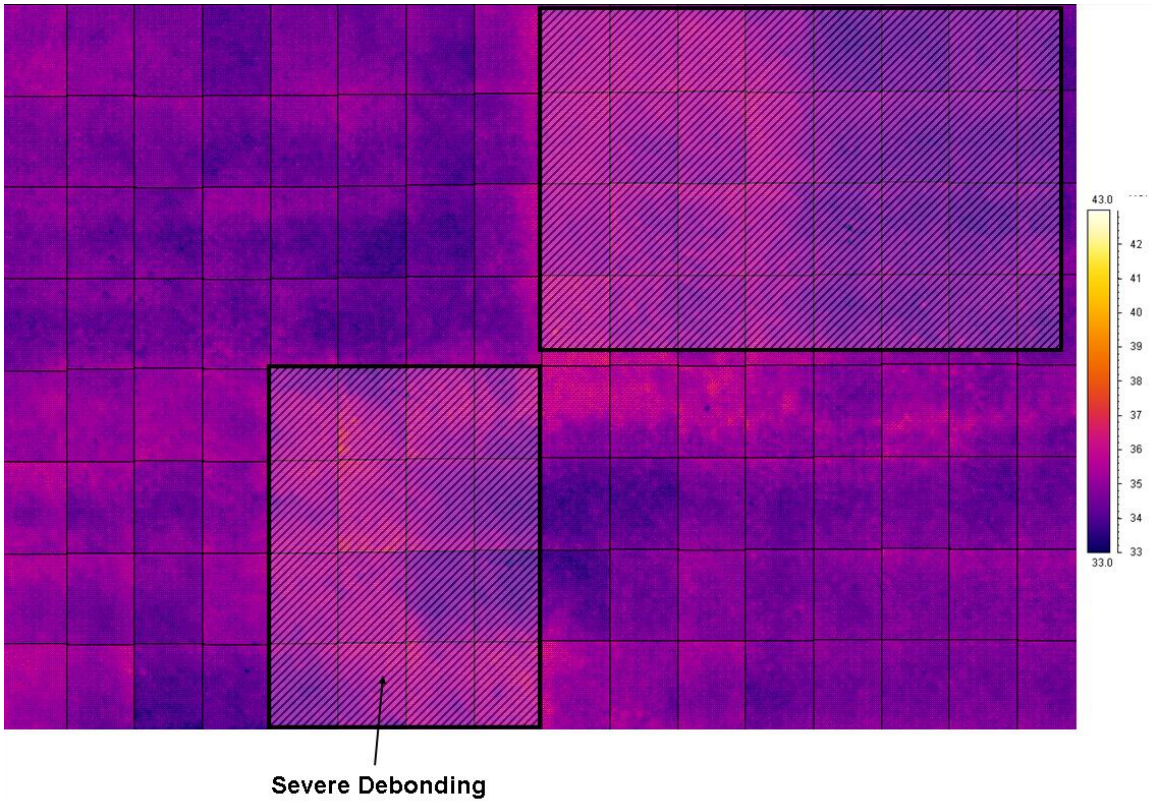

Figure 6.27 – Infrared Camera Results on Transition Area

severe debonding showed marginal change in temperature and other defects could not be detected. As such, the thermographical imaging considered as not a practical method in this

study. Maybe with further advancements in camera or active heating of pavement this method can be of greater utility.

Ground Coupled GPR

The processed linescans obtained with the ground-coupled GPR system along Lines 1 to 10 are shown in Figure 6.28. Locations of the prepared debonding are also included in the figure. The results from this experiment essentially confirmed the results from the preliminary study in Chapter 5. The ground-coupled GPR can clearly detect the severely-debonded areas in the transition zone, but the fully- and partially debonded areas could be sometimes detected, especially when the debonding agents were clay or talcum powder.

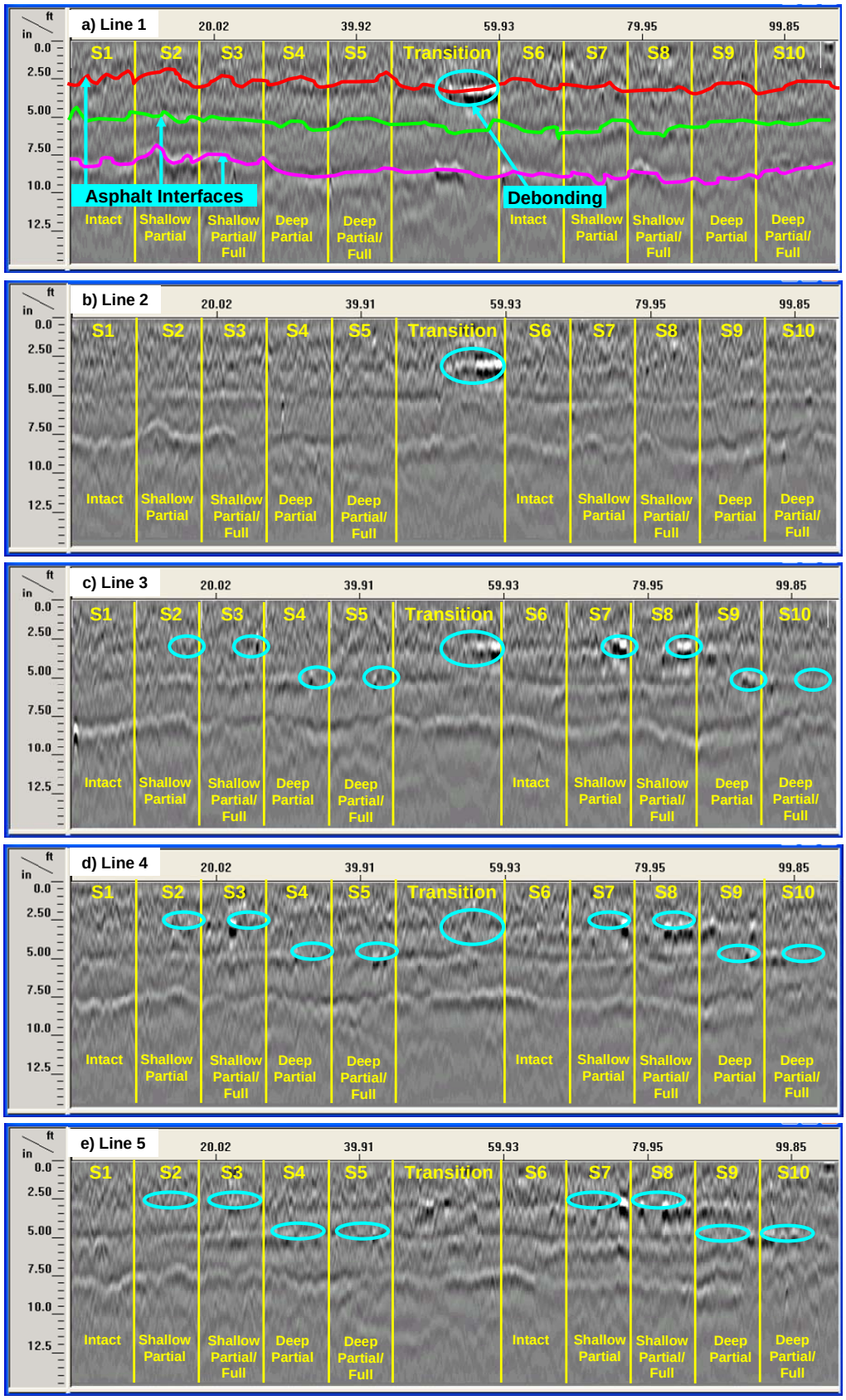

Figure 6.28 – Processed Linescans with Ground-Coupled GPR from Extended Tests

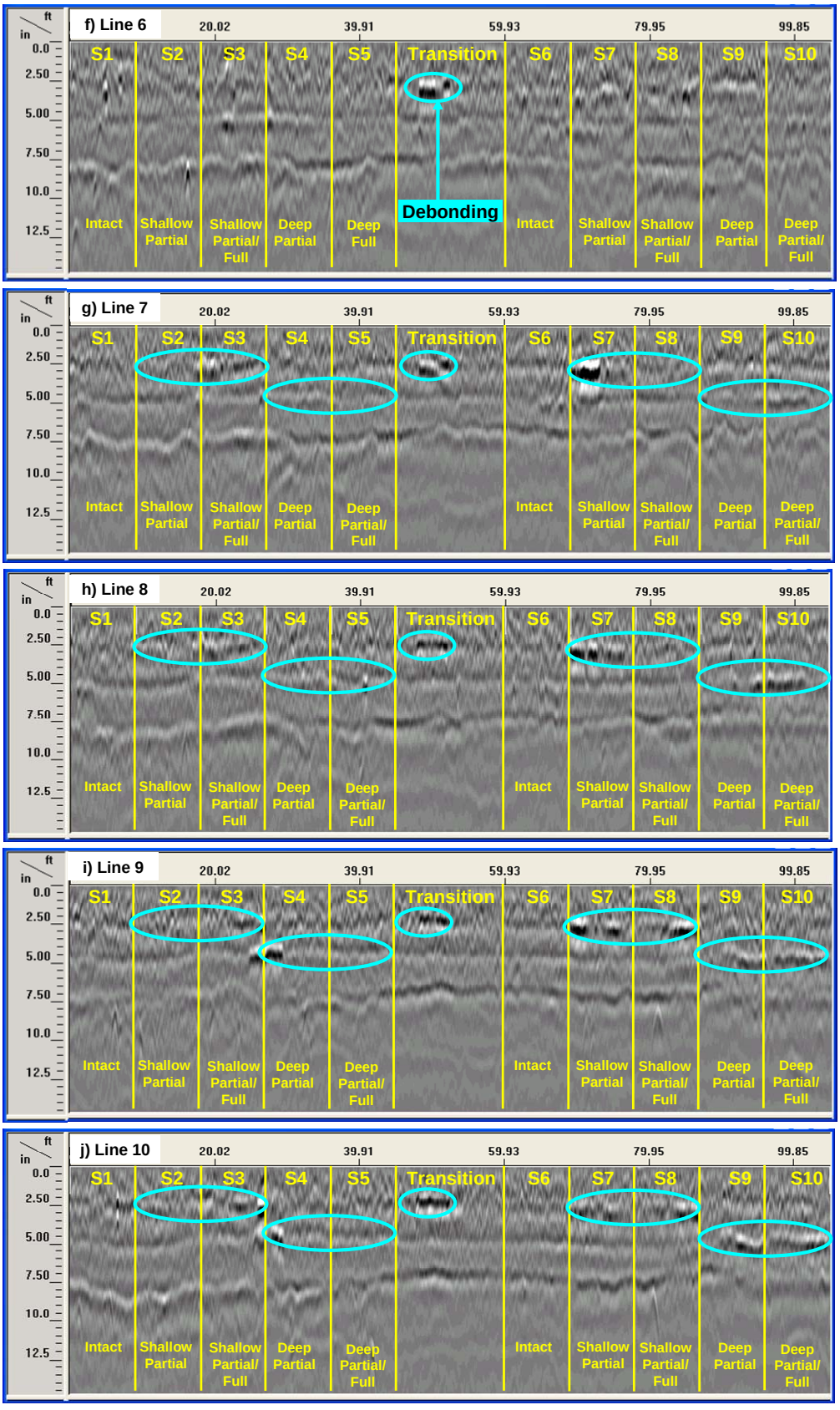

Figure 6.28 Contd. – Processed Linescans with Ground-Coupled GPR from Extended Tests

CHAPTER 7

FIELD INVESTIGATION OF SELECTED NDT METHODS

Selected NDT methods and test protocols were evaluated on several features of Portland International Airport (PDX) and Boston Logan International Airport (BOS). The primary goal of the field study was to ensure that the methods are reasonable under actual field conditions. Results obtained at PDX and BOS are presented next.

Portland International Airport Site

Several areas of PDX presented low to medium severity longitudinal cracking. The cracking pattern appeared to indicate that the upper lift of the pavement might be debonded. Several areas of PDX that presented these problems or were suspect of being debonded were selected in consultation with PDX staff as shown in Figure 7.1.

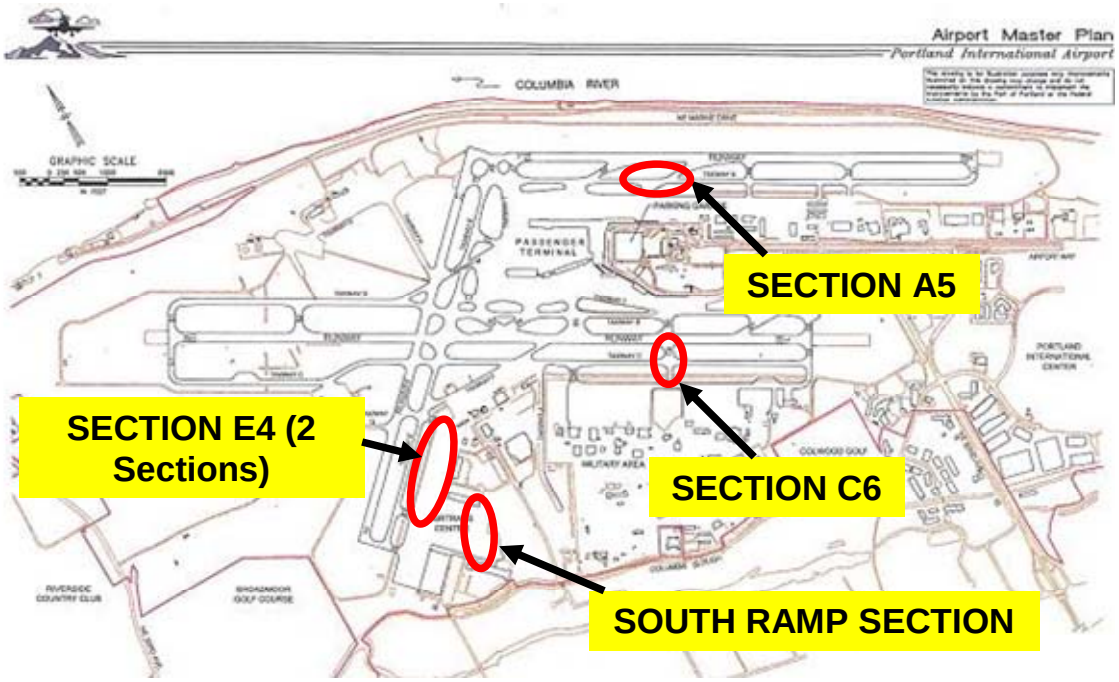

Figure 7.1 – Schematic of PDX and Location of Test Sections

The suspect areas corresponded to sections of Taxiways A, C and E, and the South Ramp. Section A5 was located on Taxiway A, parallel to Runway 10L/28R near Taxiway A5 (Figure 7.2). Taxiway A showed longitudinal cracking. Based on cores extracted by PDX staff, cracking was mostly confined to the top asphalt overlay. According to PDX staff, the overlay in some instances was not tightly bonded to the underlying asphalt lifts, and there was some indication of striping.

Section C6 was located on Taxiway C6 as shown in Figure 7.3. Similar to Taxiway A, there were some indications that the upper lift of pavement was not bonded. However, these problematic areas were already repaired. A section adjacent to the repaired area was tested.

The location of the South Ramp Section is shown in Figure 7.4. Some areas of this section presented advanced stages of longitudinal and transverse cracking that developed into alligator cracking and some areas of rutting (Figure 7.5a), while other areas did not exhibited surface distress (Figure 7.5b).

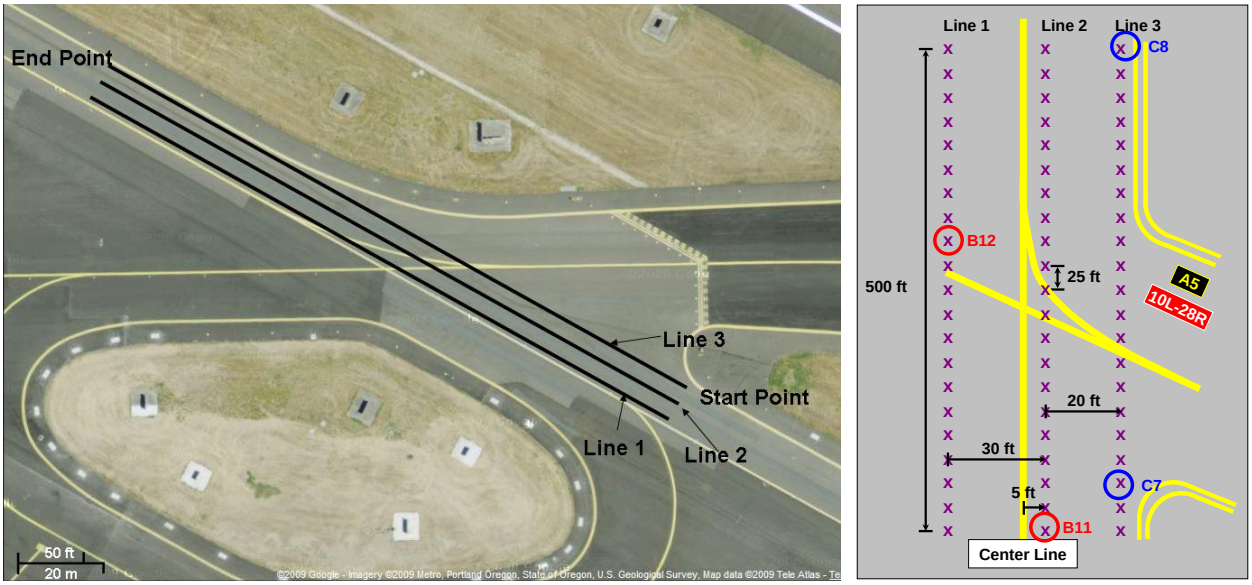

Figure 7.2 – Location of Section A5 and Test Layout

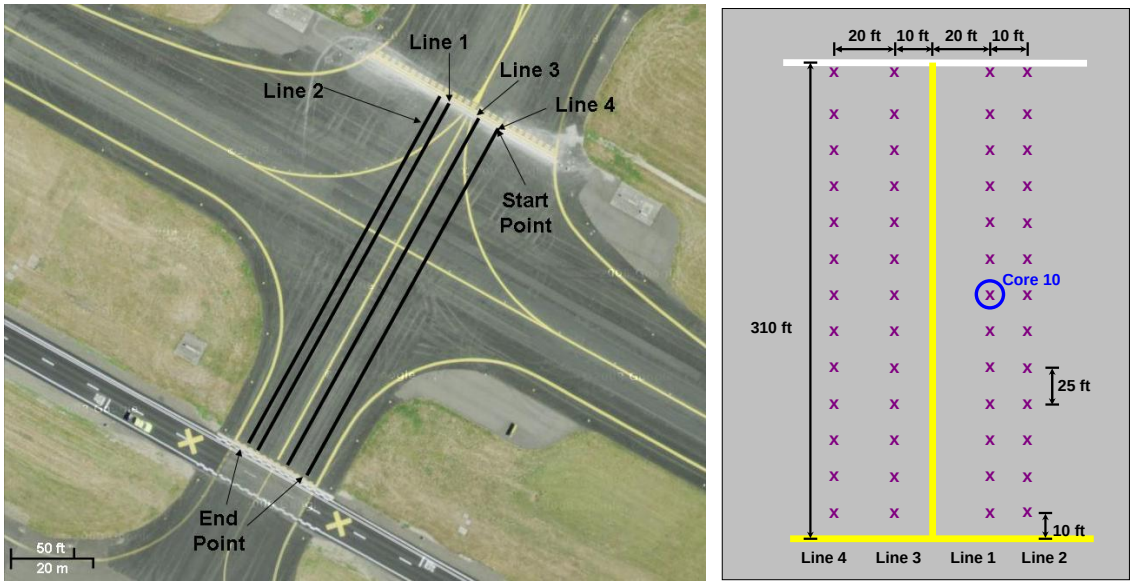

Figure 7.3 – Location of Section C6 and Test Layout

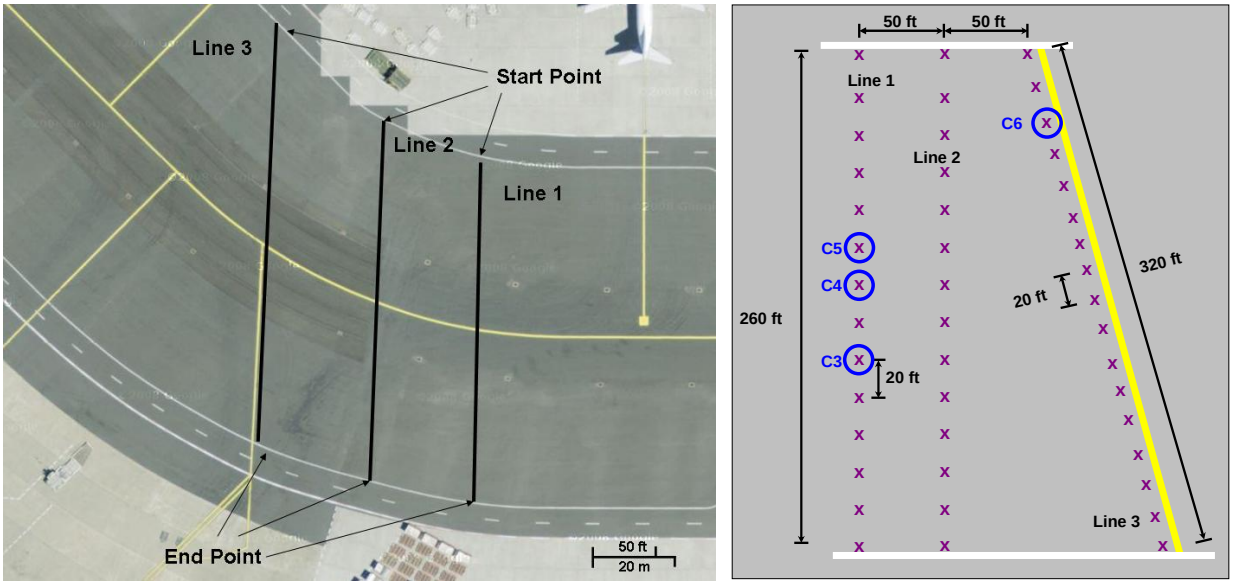

Figure 7.4 – Location of South Ramp Section and Test Layout

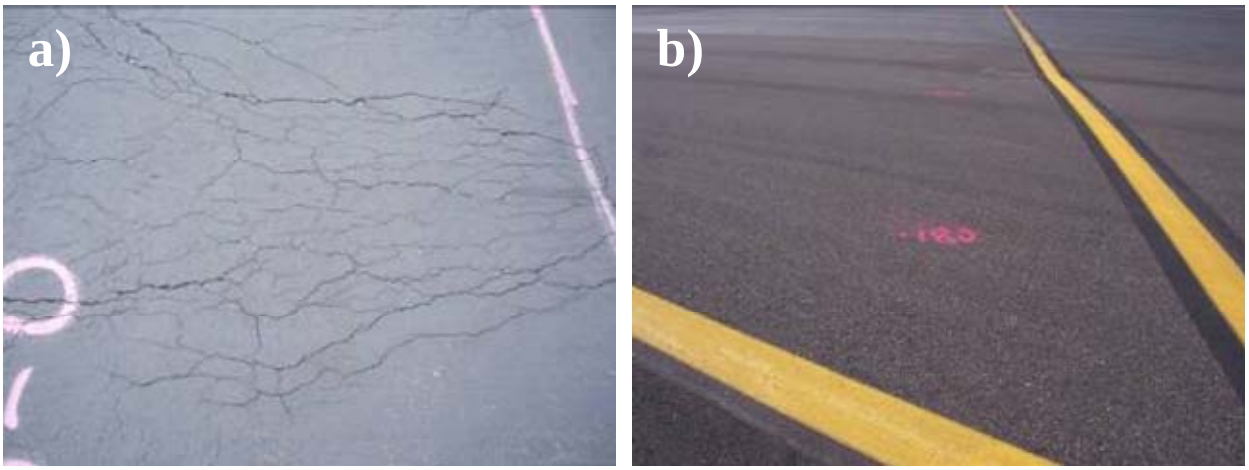

Figure 7.5 – Damaged and Intact Areas on South Ramp Section

Two adjacent sections were investigated next to Taxiway E4 as shown in Figure 7.6. No visual distress was observed throughout the entire section. Section 1 was recently repaired while Section 2 had not been repaired except for the first 30 ft.

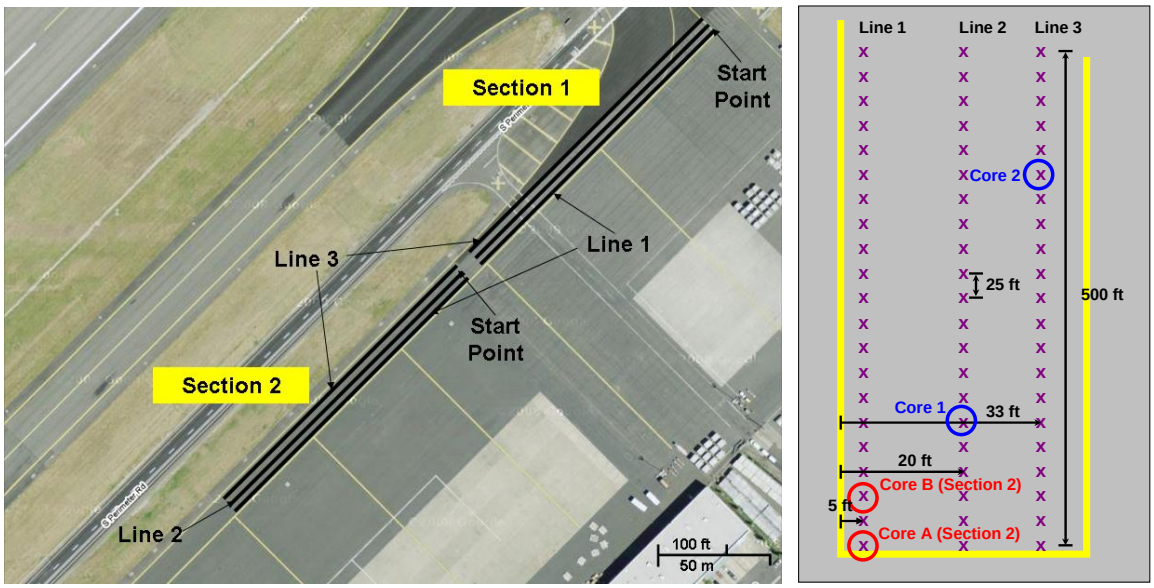

Figure 7.6 – Location of Sections 1 and 2 of E4 and Test Layout

Ultrasonic surface waves, impulse response, ground-coupled GPR and FWD were used to test these sections. The test schemes for each section are also shown in Figures 7.2 through 7.6. Three or four 200- to 500-ft long lines were selected at each site. The GPR tests were carried out along these lines. The other tests were carried out at discrete points between 20 ft to 50 ft apart.

Test Results

Section A5

Post-processed GPR linescans along the three lines at this section are shown on Figure 7.7. Several HMA layer interfaces are marked. Some of these interfaces showed stronger reflections that might indicate the presence of trapped moisture or the existence of stripping or debonding, particularly for the first 200 ft of Line 3. The results from the other methods are illustrated in Figure 7.8. The data were processed and presented in the same format as Chapter 6 for consistency. All methods and analyses point to problems along Line 3.

Table 7.1 contains the results of the four confirmatory cores extracted from this section. The results from the three mechanical tests are similar for cores B11 and B12 and point to intact sections. Even though the mechanical tests for the other two cores indicate damaged cores, the cores were reasonably intact but the quality of HMA was in question.

Table 7.1 – Comparison of Core Condition with NDT Results on Section A5

Core #	Location	GPR	PSPA	IR	FWD	Condition/Comments
B11	Line 2 @0 ft	Intact	Intact	Intact	Intact	Intact
B12	Line 1 @250 ft	Suspect	Intact	Intact	Intact	Intact
C7	Line 3 @0 ft	Suspect	Damaged	Damaged	Damaged	Low quality HMA, Core broken at 9.5 in.
C8	Line 3 @500 ft	Intact	Damaged	Damaged	Damaged	Low quality HMA, Intact

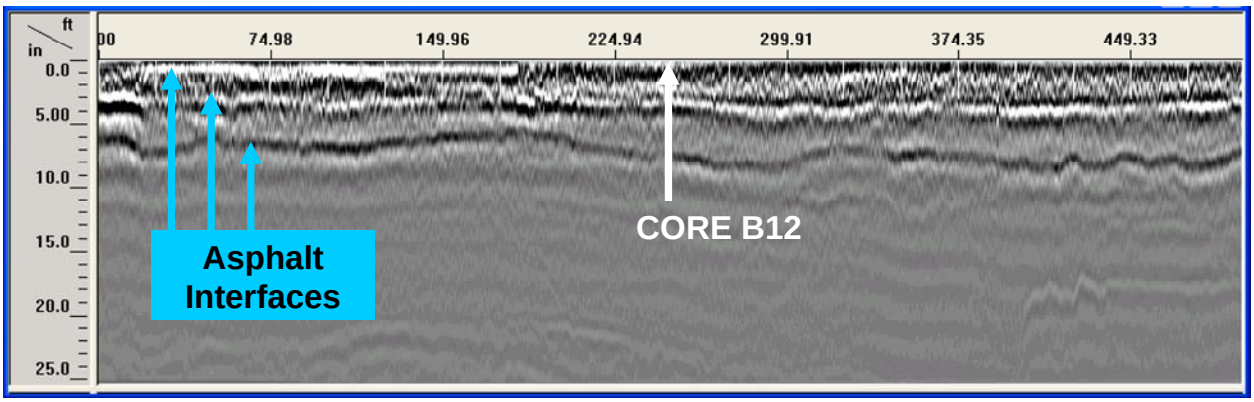

a) Line 1

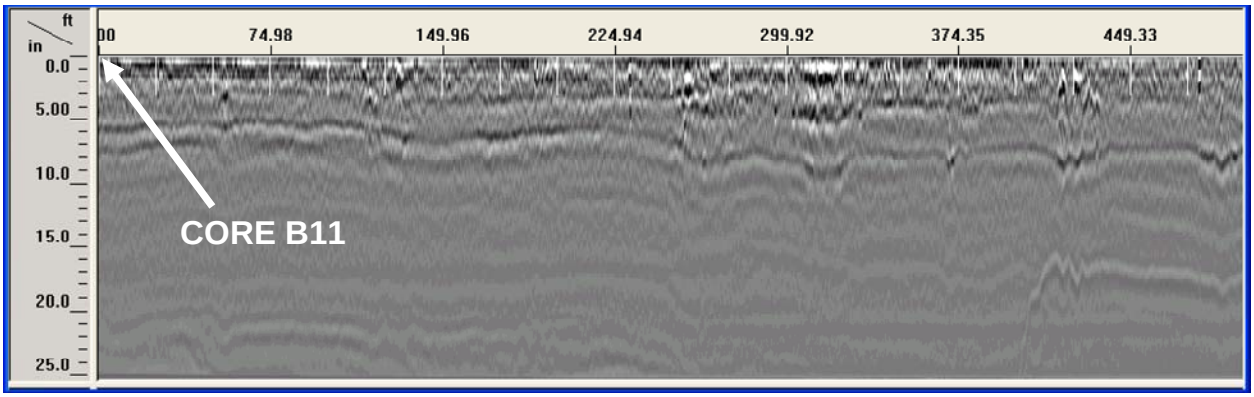

b) Line 2

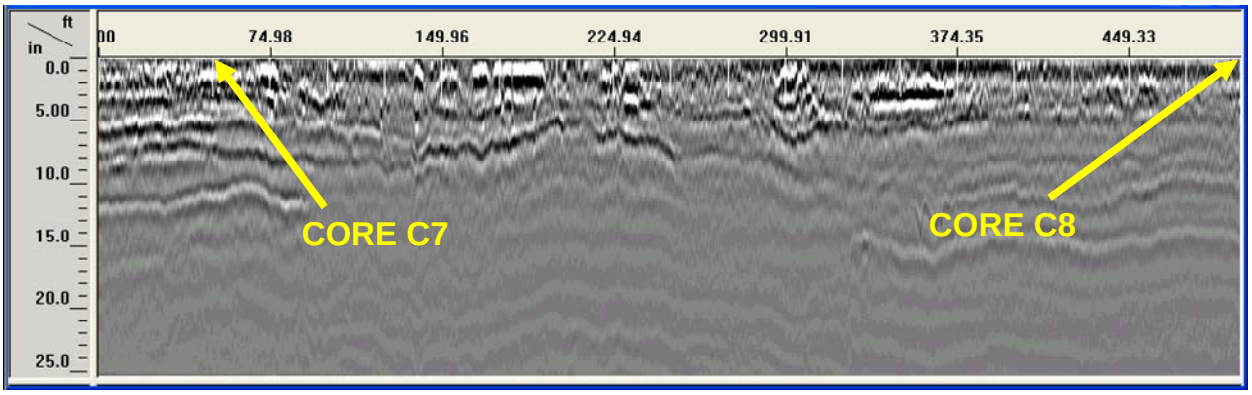

c) Line 3

Figure 7.7 – Post-processed GPR Linescans on Section A5

	Distance from Start Point (ft)																				
	0	25	50	75	100	125	150	175	200	225	250	275	300	325	350	375	400	425	450	475	481	500
Line 1	1905	1715	2017	1678	1785	1669	2082	1567	1984	1868	2116	1748	1857	1864	1804	1755	1766	1819	2014	1984	N/A	2026
Line 2	2432	2105	1879	2028	2143	2483	1891	1748	2112	2032	2171	1876	2034	1350	2330	1651	2372	1350	2330	2086	2211	1318
Line 3	1120	1220	1150	1383	1960	1730	1210	1319	1439	1049	1558	1665	1772	1314	1688	1879	1765	2063	1714	1627	N/A	1259

a) PSPA Modulus (ksi)

	Distance from Start Point (ft)																				
	0	25	50	75	100	125	150	175	200	225	250	275	300	325	350	375	400	425	450	475	481	500
Line 1	6.8	12.3	11.0	10.0	7.6	9.5	10.9	11.1	9.8	6.9	9.1	5.7	9.3	10.7	6.4	6.6	4.6	5.5	5.5	5.5	N/A	6.1
Line 2	9.8	8.7	9.0	11.6	6.7	11.4	12.5	8.1	7.5	7.7	9.0	5.9	11.0	12.1	13.9	6.3	7.7	3.9	6.5	7.4	6.8	8.4
Line 3	2.6	2.0	2.0	2.2	7.4	9.7	8.4	4.1	5.3	6.0	3.5	8.4	6.0	9.9	5.0	4.1	4.2	4.2	3.5	3.4	N/A	4.0

b) IR Results (FFT Ratios)

	Distance from Start (ft)										
	0	50	100	150	200	250	300	350	400	450	500
Line 1	10.2	9.4	9.5	9.5	8.8	8.9	9.2	9.9	9.6	13.6	14.4
Line 2	11.3	10.3	8.9	8.6	8.7	9.7	8.8	7.2	9.7	13.2	12.7
Line 3	20.9	29.0	9.9	10.4	9.7	8.4	9.5	15.5	16.3	16.1	15.9

c) FWD Deflections (mils)

	Distance from Start (ft)										
	0	50	100	150	200	250	300	350	400	450	500
Line 1	172	187	185	186	199	198	189	177	181	129	122
Line 2	156	170	198	203	199	181	199	245	181	132	139
Line 3	83	60	176	169	181	211	183	112	107	108	110

d) FWD Modulus (ksi)

Figure 7.8 – NDT Results on Section A5

Section C6

Linescan for Line 1 of this section is shown in Figure 7.9 and for all lines in Appendix F. Strong reflections are detected at depths of about 2 and 5 in. along the first 150 ft of the section.

PSPA, IR and FWD results along Section C6 are included in Figure 7.10. Dispersion curves from USW are presented in Appendix F for all lines. Most data points seem to indicate an intact section. The only confirmatory core (Core 10) obtained at this section was on Line 1 as shown in Figure 7.11. As summarized in Table 7.2, the core location was designated as damaged with PSPA and IR, and intact with GPR and FWD. Core C10 was stripped at 5 in. depth as shown in Figure 7.11.

Table 7.2 – Comparison of Core Condition with NDT Results on Section C6

Core #	Location	GPR	PSPA	IR	FWD Deflection	Condition/Comments
C10	L1 @160 ft from start	Intact	Damaged	Damaged	Intact	Stripping between top and middle layer

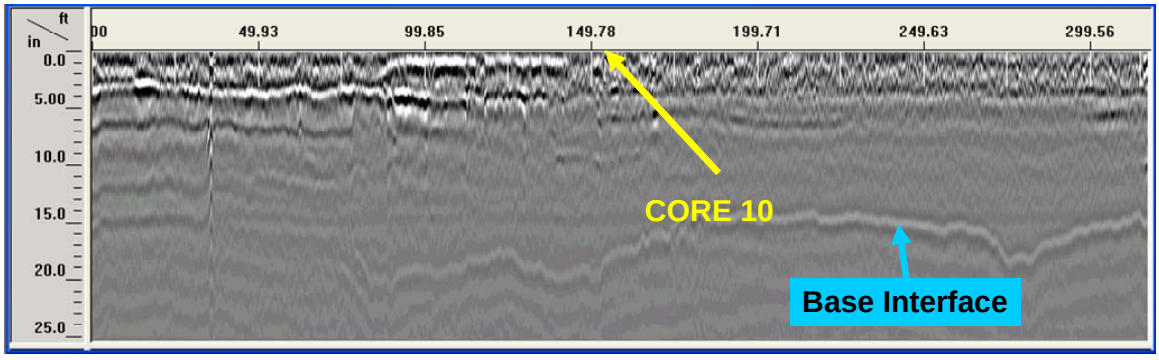

Figure 7.9 – Post-processed GPR Linescans of Line 1 on Section C6

	Distance from Start Point (ft)												
	10	35	60	85	110	135	160	185	210	235	260	285	310
Line 4	2097	2013	1719	1925	1115	1527	1290	1789	1545	1413	1458	1439	1951
Line 3	2225	1376	1849	1830	1390	1513	1705	1710	1409	1635	1761	1516	1905
Line 1	2022	1626	1839	1655	1633	1413	1372	1646	1127	1971	1753	1478	1420
Line 2	2009	1646	1856	1883	1757	1541	1909	1454	1368	1525	1692	1596	1501

a) PSPA Modulus (ksi)

	Distance from Satrt (ft)												
	10	35	60	85	110	135	160	185	210	235	260	285	310
Line 4	7.5	5.1	6.1	9.1	8.6	7.9	6.2	7.3	7.7	7.8	7.2	7.3	7.7
Line 3	5.5	5.9	5.8	12.2	9.8	9.0	9.4	6.9	8.2	8.1	5.9	6.6	6.4
Line 1	7.4	5.2	5.7	10.9	6.9	7.6	3.7	6.6	4.6	5.2	8.0	6.3	4.4
Line 2	5.8	7.0	7.4	7.8	6.8	9.9	6.9	5.9	5.3	7.2	8.7	8.3	8.1

b) IR Results (stiffness)

	Distance from Start (ft)												
	10	35	60	85	110	135	160	185	210	235	260	285	310
Line 4	20.1	25.0	20.7	14.9	17.5	18.1	19.7	21.9	22.2	23.5	23.0	21.8	20.7
Line 3	28.1	25.0	25.5	14.7	16.4	18.0	20.0	21.8	23.0	23.5	25.2	23.3	21.8
Line 1	23.5	28.9	22.6	14.6	18.3	18.1	18.9	24.0	27.0	24.5	21.7	19.1	22.0
Line 2	19.2	21.4	18.4	16.0	17.1	16.6	18.8	24.0	26.8	21.3	19.9	17.5	20.8

c) FWD Deflections (mils)

	Distance from Start (ft)												
	10	35	60	85	110	135	160	185	210	235	260	285	310
Line 4	86	69	84	118	100	96	89	80	79	74	76	80	84
Line 3	62	70	68	119	106	96	87	80	75	74	69	75	80
Line 1	74	60	77	119	95	96	92	72	64	71	81	91	79
Line 2	91	81	94	109	101	104	93	72	65	82	88	100	84

d) FWD Modulus (ksi)

Figure 7.10 – NDT Results on Section C6

Figure 7.11 – Core C10 Stripped at 5 inches from Section C6

South Ramp Section

The results from all methods at this section are shown in Figures 7.12 and 7.13, and in Appendix F. The PSPA indicates less of a problem at this section than the IR and FWD, especially along Line 1. For that reason, three of the four validation cores were obtained along Line 1 as shown in Figure 7.14. The conditions of these cores with the interpretations of the NDT devices are summarized in Table 7.3. PSPA and FWD detected Core 3 as intact, where IR showed marginal condition. Cores 4 and 5 were categorized as damaged with both IR and FWD and PSPA showed intact condition. For the case of GPR, a strong reflection close to the surface was evident for Core 6.

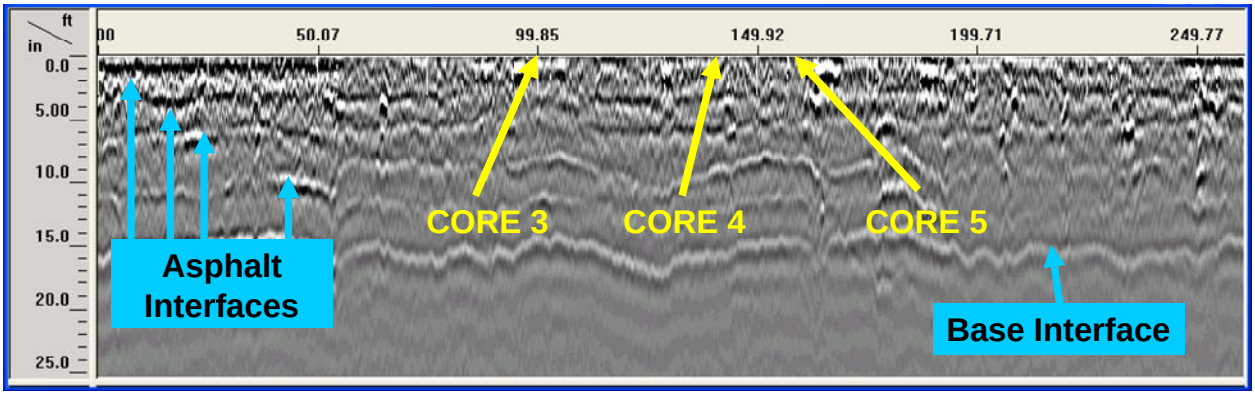

Figure 7.12 – Post-processed GPR Linescans of Line 1 on South Ramp Section

	Distance from Start (ft)																
	-60	-40	-20	0	20	40	60	80	100	120	140	160	180	200	220	240	260
Line 1				2180	2073	2146	1967	1919	1917	1906	2128	2361	1928	1913	1925	1906	1803
Line 2				1981	2122	2112	1469	1966	1868	2135	2138	1530	1516	1954	1983	2053	1380
Line 3	1957	1569	2145	2475	2004	1996	1949	2150	1703	1534	1912	1721	2147	1063	552	2177	1782

a) PSPA Modulus (ksi)

	Distance from Satrt (ft)																
	-60	-40	-20	0	20	40	60	80	100	120	140	160	180	200	220	240	260
Line 1				7.7	6.6	5.1	4.1	4.0	4.7	4.6	3.1	3.6	3.2	5.8	4.7	7.2	7.2
Line 2				9.7	7.0	8.7	3.2	8.4	6.7	6.1	6.6	3.9	4.2	2.9	5.1	6.7	3.9
Line 3	7.2	6.1	9.6	8.6	8.1	6.0	9.0	8.4	6.0	6.5	8.8	4.9	7.3	3.8	2.8	6.8	9.1

b) IR Results (FFT Ratios)

	Distance from Start (ft)																
	-60	-40	-20	0	20	40	60	80	100	120	140	160	180	200	220	240	260
Line 1				N/A	20.3	20.3	23.0	18.8	23.6	19.9	26.4	31.5	30.7	28.6	22.4	20.7	17.6
Line 2				N/A	18.4	18.2	29.5	18.1	22.0	22.9	22.6	29.0	30.2	38.3	25.7	22.5	28.7
Line 3	N/A	26.2	17.5	18.1	18.4	19.4	17.9	21.3	20.1	20.7	18.9	28.2	24.4	31.7	34.5	29.3	21.0

c) FWD Deflections (mils)

	Distance from Start (ft)																
	-60	-40	-20	0	20	40	60	80	100	120	140	160	180	200	220	240	260
Line 1				N/A	86	86	76	93	74	87	66	55	56	61	78	84	99
Line 2				N/A	95	96	59	97	79	76	77	59	57	45	67	77	60
Line 3	N/A	66	100	96	96	90	98	81	87	84	92	61	71	55	50	59	83

d) FWD Modulus (ksi)

Figure 7.13 – NDT Results on South Ramp Section

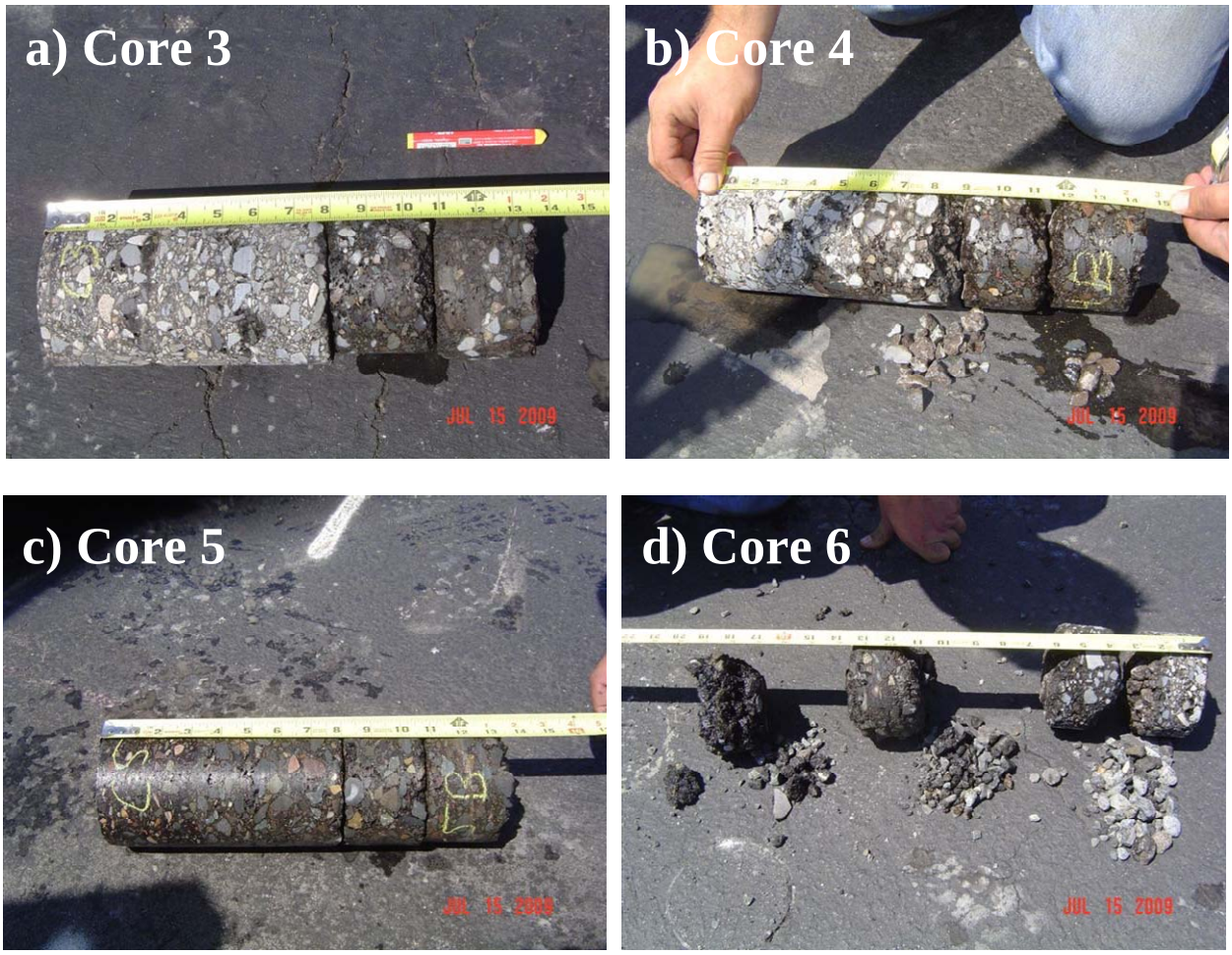

Figure 7.14 – Cores Retrieved from South Ramp Section

Table 7.3 – Comparison of Core Condition with NDT Results on South Ramp Section

Core #	Location	GPR	PSPA	IR	FWD Deflection	Condition/Comments
C3	L1 @100 ft from start	Intact	Intact	Marginal	Intact	Intact.
C4	L1 @140 ft from start	Intact	Intact	Damaged	Damaged	Some stripping at 9 in.
C5	L1 @160 ft from start	Intact	Intact	Damaged	Damaged	Intact
C6	L3 @280 ft from start	Damaged	Damaged	Damaged	Damaged	Severe stripping between each lift

Sections E4

The results from the four tests along the two sections are shown in Figures 7.15 through 7.19 and Appendix F. For Section 1, Line 3 of GPR exhibited two distinctive interfaces at 4 in. and 10 in., while for Section 2, four different interfaces were identified on all lines. However, the strong reflections obtained along the first 75 ft of Section 2 indicate the presence of moisture or possible existence of stripping or debonding.

There are some similarities and differences in the damaged areas identified by different methods. PSPA dispersion curves showed stronger reduction in modulus for points along Lines 2 and 3 from Section 1 and less significant reduction for points of Section 2 (see Appendix F).

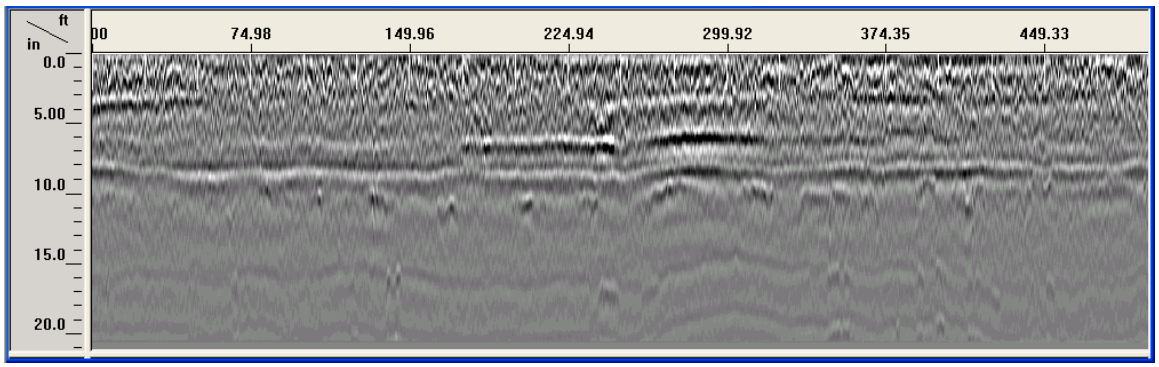

a) Line 1 of Section 1

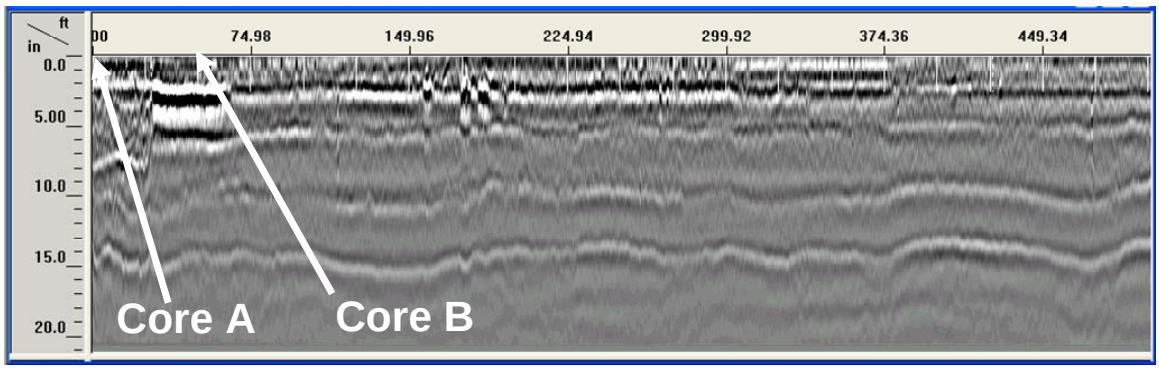

b) Line 1 of Section 2

Figure 7.15 – Post-processed GPR Linescans on Line 1 of Sections 1 and 2 of E4

	Distance from Start Point (ft)																				
	0	25	50	75	100	125	150	175	200	225	250	275	300	325	350	375	400	425	450	475	500
Line 1	1805	1927	1627	1816	1819	1823	1579	2026	2107	2055	2237	2235	2330	2251	2066	2469	2423	2236	1913	2152	1653
Line 2	1718	2439	1382	1868	1641	2038	1305	1527	1723	1515	2022	1604	1689	1848	1831	2107	1561	1456	1641	1933	1990
Line 3	1880	1613	1868	1766	1740	1694	1499	2031	2367	1564	1785	1653	1507	1775	1608	1544	1775	1831	2074	1985	1640

a) Section 1

	Distance from Start Point (ft)																				
	0	25	50	75	100	125	150	175	200	225	250	275	300	325	350	375	400	425	450	475	500
Line 1	1777	1727	2045	2124	2164	2411	2010	2062	1756	2212	1289	1999	2158	2067	1992	2091	2039	2219	2156	2790	2189
Line 2	1657	2017	2140	1973	2188	1806	2051	2126	2237	2212	2212	2172	2319	1923	2193	2383	1872	2049	2365	2320	2148
Line 3	2192	2037	2081	2249	2211	2128	2000	1889	2113	1745	1960	1894	2320	2250	2254	2096	2153	2096	2496	2057	1986

b) Section 2

Figure 7.16 – PSPA Modulus (ksi) on Sections 1 and 2 of E4

	Distance from Start Point (ft)																				
	0	25	50	75	100	125	150	175	200	225	250	275	300	325	350	375	400	425	450	475	500
Line 1	13.0	10.7	12.5	13.1	9.3	13.1	9.4	9.4	10.3	9.8	8.6	9.3	10.7	13.2	12.8	9.6	9.1	15.7	11.3	11.0	10.9
Line 2	10.6	11.4	11.5	10.5	9.6	11.0	9.5	10.2	12.1	10.3	11.6	9.0	11.5	11.1	11.4	10.1	10.8	13.1	15.1	9.0	10.5
Line 3	13.5	11.3	11.5	17.1	15.6	9.4	11.3	11.5	10.1	12.2	8.9	9.2	10.6	13.7	11.0	8.1	7.4	10.1	11.9	11.4	10.8

a) Section 1

	Distance from Start Point (ft)																				
	0	25	50	75	100	125	150	175	200	225	250	275	300	325	350	375	400	425	450	475	500
Line 1	4.4	6.7	6.9	8.3	8.0	7.2	8.5	6.4	6.9	6.9	7.3	8.4	7.6	8.2	7.8	7.3	6.4	6.3	7.1	7.0	6.7
Line 2	4.5	6.8	6.9	7.5	8.7	7.8	7.1	7.7	9.5	7.8	7.6	6.7	7.2	8.1	7.8	7.0	7.1	6.6	6.8	7.2	6.8
Line 3	4.4	6.0	6.9	6.9	7.4	8.0	7.2	6.7	7.8	6.8	6.8	6.5	6.5	6.3	6.6	7.7	7.3	6.7	6.7	6.8	6.7

b) Section 2

Figure 7.17 – IR Results (FFT Ratios) on Sections 1 and 2 of E4

	Distance from Start Point (ft)																				
	0	25	50	75	100	125	150	175	200	225	250	275	300	325	350	375	400	425	450	475	500
Line 1	11.5	11.4	11.9	11.1	12.5	11.5	11.4	11.4	11.0	10.2	11.0	11.4	11.5	10.9	10.9	11.6	11.6	12.2	11.9	12.3	12.5
Line 2	11.2	11.1	11.8	12.2	12.0	12.2	11.7	11.7	11.5	11.3	11.4	11.5	11.4	11.0	11.2	11.3	11.3	11.6	11.9	12.7	12.6
Line 3	11.2	10.5	11.6	11.8	12.6	11.9	12.0	12.2	13.0	13.9	13.1	12.2	13.2	12.0	12.1	12.7	12.6	12.6	12.4	12.6	13.0

a) Section 1

	Distance from Start Point (ft)																				
	0	25	50	75	100	125	150	175	200	225	250	275	300	325	350	375	400	425	450	475	500
Line 1	20.3	17.1	16.8	15.6	15.3	14.4	14.5	15.1	15.6	15.6	16.1	15.1	15.6	15.0	15.3	15.3	16.9	16.9	15.9	15.1	17.0
Line 2	18.4	20.8	16.5	17.0	16.4	16.3	15.6	15.4	15.3	15.9	16.4	17.5	16.5	15.7	17.5	16.5	17.7	18.0	17.5	16.4	18.0
Line 3	19.8	19.7	16.3	16.1	15.9	14.9	15.6	15.3	15.6	16.6	17.1	16.0	15.5	16.2	16.7	15.4	14.9	15.2	15.6	14.9	16.4

b) Section 2

Figure 7.18 – FWD Deflection Results (mils) on Sections 1 and 2 of E4

	Distance from Start Point (ft)																				
	0	25	50	75	100	125	150	175	200	225	250	275	300	325	350	375	400	425	450	475	500
Line 1	152	154	147	158	139	152	155	153	159	171	160	154	152	161	161	151	151	143	147	142	140
Line 2	156	158	148	144	146	143	149	149	152	155	154	152	153	159	155	155	155	150	147	137	138
Line 3	156	167	150	149	139	147	146	143	134	126	134	143	132	146	145	138	139	139	142	139	134

a) Section 1

	Distance from Start Point (ft)																				
	0	25	50	75	100	125	150	175	200	225	250	275	300	325	350	375	400	425	450	475	500
Line 1	85	102	104	112	115	122	121	115	112	112	109	117	112	118	115	115	104	104	110	117	103
Line 2	95	84	106	103	107	108	112	114	115	110	107	100	106	112	100	106	99	97	101	107	98
Line 3	88	88	108	109	111	118	112	115	113	105	102	110	113	108	104	114	118	115	112	118	108

b) Section 2

Figure 7.19 – FWD Modulus Results (ksi) on Sections 1 and 2 of E4

Two cores were extracted from Section 1 and two from Section 2 as summarized in Table 7.4. Cores 1 and 2 were separated at a depth of about 10 in. as shown in Figure 7.20. Core 1 was interpreted as marginal or damaged by the IR and PSPA and intact by the others. Core 2 was identified as damaged with all NDT methods. Aside from the lower quality HMA at depths of about 4 in. to 7 in., the reason for this discrepancy is unknown. For cores from Section 2, Core A was categorized as damaged and Core B as intact by all NDT methods (except GPR). It seems that all mechanical tests have a difficulty delineating between low-quality HMA and debonding.

Table 7.4 – Comparison of Core Condition with NDT Results on Sections 1 and 2 of E4

Core #	Location	GPR	PSPA	IR	FWD Deflection	Condition/Comments
Core 1	L2 @ 150 ft from start of Section 1	Intact	Damaged	Marginal	Intact	Intact
Core 2	L3 @ 375 ft from start of Section 1	Damaged	Damaged	Damaged	Damaged	Intact/Low quality HMA
Core A	L1 @0 ft from start of Section 2	Damaged	Damaged	Damaged	Damaged	Intact/Low quality HMA
Core B	L1 @50 ft from start of Section 2	Damaged	Intact	Intact	Intact	Intact Core. Sample length 14½“

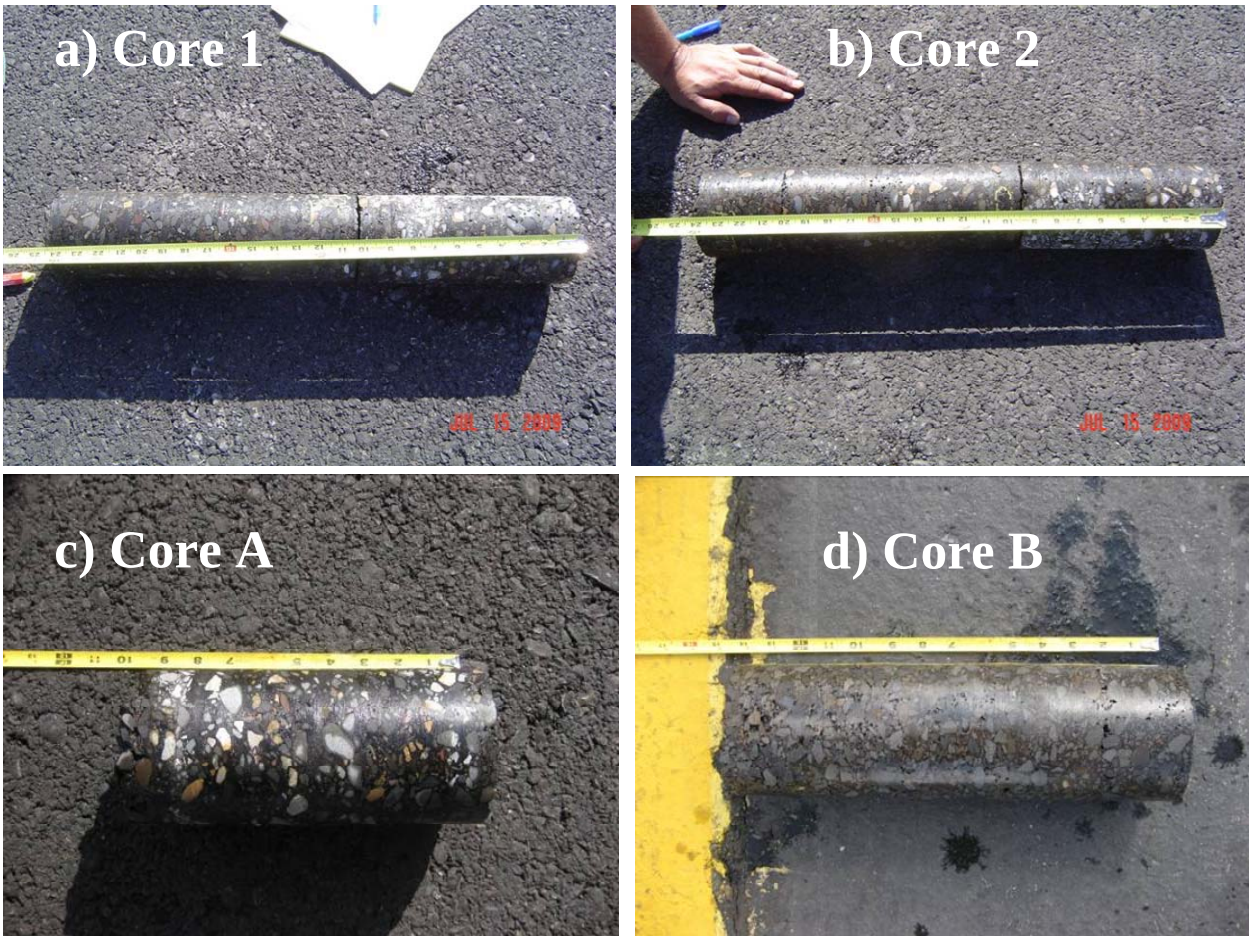

Figure 7.20 – Cores Retrieved from Sections 1 and 2 of E4

Boston Logan International Airport Site

A stretch of Runway 9-27 was tested with several NDT methods concurrent with its rehabilitation in July 2009. Based on previous studies conducted on Runway 9-27 in January 2009, several areas exhibited debonding of the top lift, and in occasions, areas of extreme stripping. Two sections were selected for field testing. Section 1 was located between Taxiways E and C and Section 2 between Runway 15/33 and Taxiway D as illustrated on Figure 7.21.

The test scheme on Section 1 is shown in Figure 7.22a. Seven 700-ft long lines, one located along the centerline and the others 25 ft, 37.5 ft and 50 ft from the centerline on each side, were considered. A total of 29 stations, with a spacing of 25 ft, were investigated on each line. In addition, five core locations previously retrieved were evaluated with some of the NDT methods.

Figure 7.21 – Schematic of BOS and Location of Test Sections

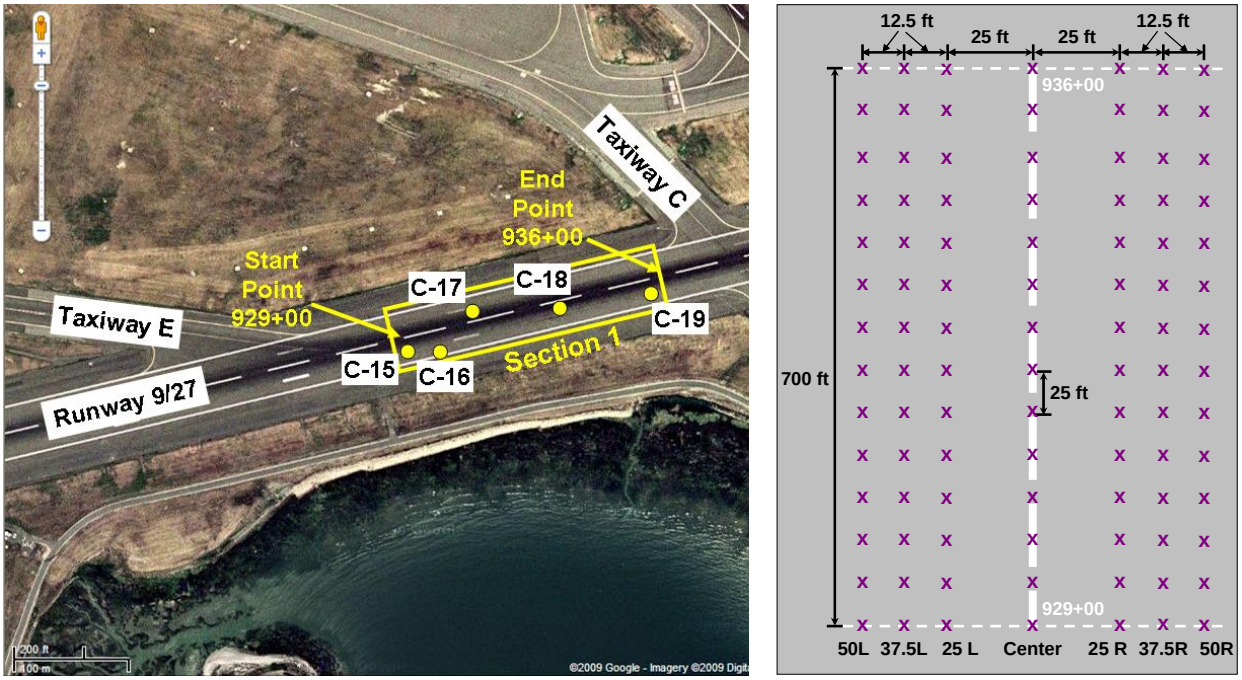

Figure 7.22 – Location of Section 1 and Test Layout

The approximate locations of these cores are also included in Figure 7.22. Some areas of this section exhibited cracking (Figure 7.23a). In addition, the middle 70 ft of the runaway had been rehabilitated a few years before showing different asphalt characteristics on the surface mat (see Figure 7.23b).

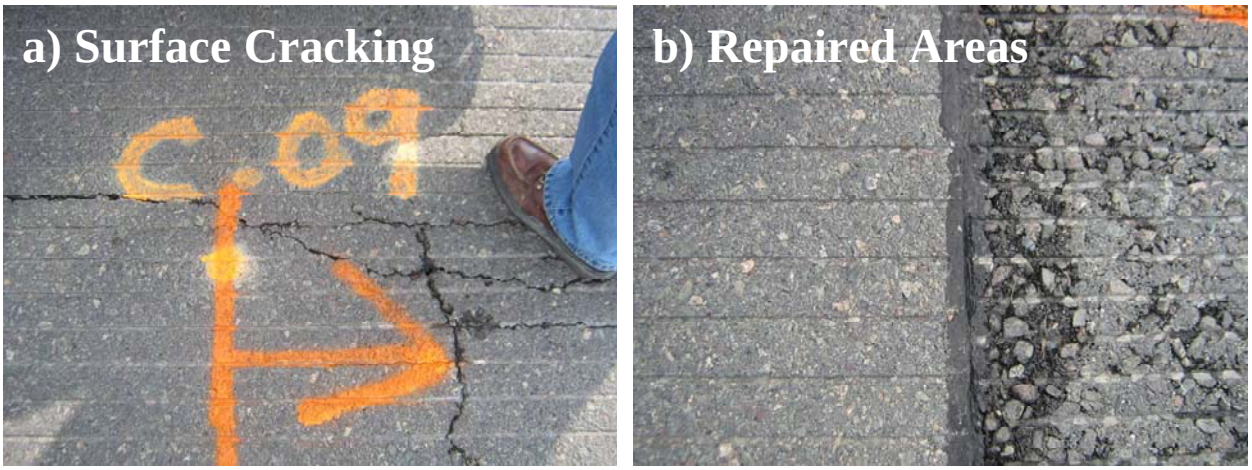

Figure 7.23 – Surface Cracking and Areas with Different Surface Pavement on Section 1

Because of time constraint during field testing and weather condition, only fifteen core locations in Section 2 were evaluated with selected NDT methods. Their approximate locations of the cores are included in Figure 7.24.

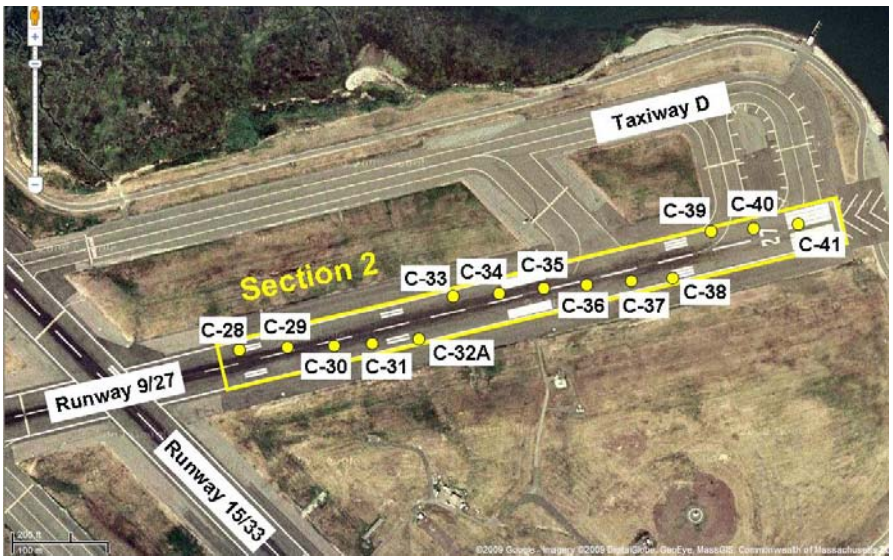

Figure 7.24 – Location of Section 2

Test Results

The selected NDT methods used in BOS were the PSPA and Impulse Response for Sections 1 and 2 and also GPR for Section 1. Results are presented next for the two sections.

Section 1

View from the west end of the section is illustrated on Figure 7.25. The ground-coupled GPR system (1.5 GHz antenna) was used on the seven test lines of Section 1. Post-processed linescans are shown in Figure 7.26. Several horizontal lines associated with the HMA interfaces are marked. Three HMA lifts are observed on all lines at depths of about 2 in., 4 in. and 6 in. Some of these interfaces show strong reflections that might indicate the presence of trapped moisture, stripping or debonding particularly for Lines 37.5'L and 50'R. In addition, two irregularities are found. The first one appeared on all lines at a distance of approximately 600 ft from the start and the other at about 450 ft and on Lines 25'L, Center and 25'R. The GPR traces at the five core locations are depicted in Appendix F.

Figure 7.25 – Field Picture of Section 1

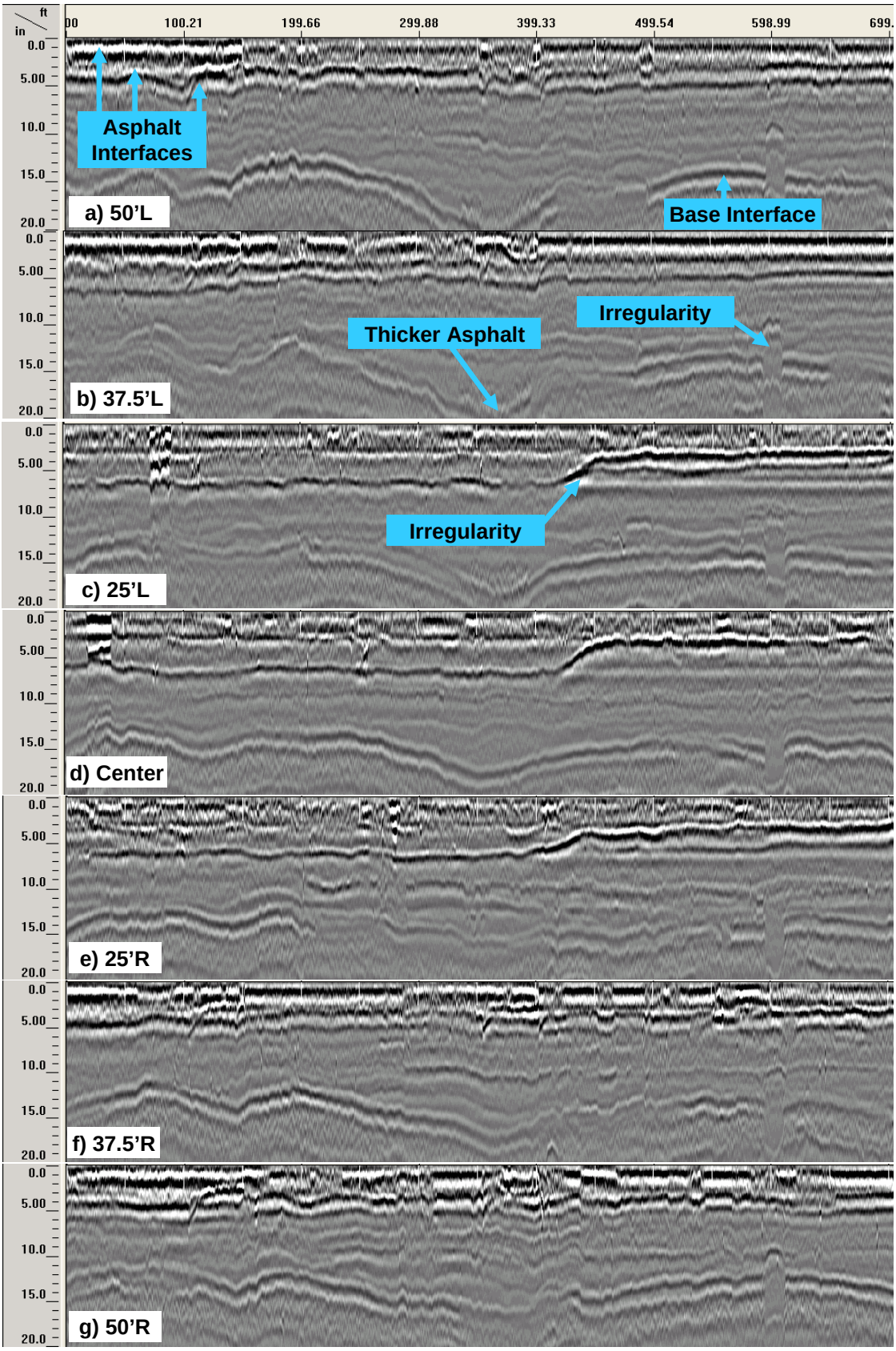

Figure 7.26 – Post-processed GPR Linescans on Section 1

The PSPA and IR results are illustrated in Figures 7.27 and 7.28 for the seven lines of Section 1. Based on both methods, the worst conditions are observed mostly about the centerline. Most of the points on these lines were identified as marginal or damaged. Dispersion curves showed stronger reduction in modulus for points about the centerline of the runway (see Appendix F).

	Test Location																												
	92900	92925	92950	92975	93000	93025	93050	93075	93100	93125	93150	93175	93200	93225	93250	93275	93300	93325	93350	93375	93400	93425	93450	93475	93500	93525	93550	93575	93600
L50	807	1,021	930	1,072	790	1,798	1,383	1,607	787	1,614	1,384	1,792	1,712	1,873	1,815	1,655	1,059	1,838	1,751	1,664	1,896	1,908	1,942	1,850	816	2,287	2,213	1,941	1,998
L37.5	799	1,188	556	1,082	823	635	1,150	997	1,601	1,110	1,998	897	814	931	601	554	548	2,036	2,129	2,129	1,536	2,187	2,226	1,991	2,109	2,179	2,321	2,036	1,937
L25	963	790	823	1,407	1,007	926	963	1,059	867	1,016	847	921	1,003	839	1,141	891	911	771	832	882	902	659	971	1,219	1,129	1,030	1,080	991	1,055
0	402	780	329	385	642	393	298	436	338	549	597	402	680	613	289	565	683	596	247	887	1,259	974	414	358	277	398	277	256	305
R25	690	975	259	594	549	716	581	489	553	654	737	655	682	1,178	609	573	524	425	488	272	542	359	553	569	554	418	375	368	337
R37.5	1,815	1,334	1,539	1,497	1,456	376	2,423	2,024	1,269	1,018	2,007	1,934	1,726	352	701	1,402	415	1,084	1,564	930	1,634	1,778	1,634	1,426	2,075	1,964	1,557	1,425	1,181
R50	1,464	1,360	1,256	1,194	1,659	1,738	1,615	1,677	1,811	1,331	1,180	1,319	1,319	2,089	1,416	1,978	1,402	2,088	1,130	2,432	1,735	2,235	2,012	2,012	1,554	2,099	1,669	2,124	1,931

Figure 7.27 – PSPA Modulus (ksi) on Section 1

	Test Location																												
	92900	92925	92950	92975	93000	93025	93050	93075	93100	93125	93150	93175	93200	93225	93250	93275	93300	93325	93350	93375	93400	93425	93450	93475	93500	93525	93550	93575	93600
L50	6.21	3.79	1.96	2.49	2.70	3.65	4.82	5.71	5.68	7.49	7.37	4.58	6.76	4.87	5.77	5.46	7.44	5.42	4.66	6.23	8.38	6.44	4.91	7.20	6.26	5.26	7.50	6.62	4.33
L37.5	4.66	5.15	4.36	3.28	6.04	3.46	6.57	6.80	9.56	9.08	6.10	4.42	3.51	5.21	4.10	3.28	1.97	5.79	5.19	5.70	6.08	6.53	6.24	4.97	5.52	4.50	6.09	6.17	6.89
L25	1.13	2.77	2.89	1.32	1.87	1.75	2.81	1.83	2.20	1.54	2.54	3.24	3.69	4.17	2.84	3.41	3.59	2.76	3.38	3.06	7.14	2.21	4.22	8.27	4.53	6.24	6.75	3.96	4.16
0	0.56	0.91	1.87	1.49	0.96	0.44	0.98	0.51	0.69	0.71	0.59	0.87	0.89	0.20	0.41	0.50	0.84	0.49	0.21	0.47	0.36	0.33	0.37	1.25	0.19	0.40	0.14	0.44	0.42
R25	0.87	0.60	0.71	0.52	0.63	1.03	0.34	1.78	0.55	0.41	1.03	1.57	2.28	1.83	1.01	4.04	0.94	0.36	0.81	0.62	0.60	0.41	1.48	0.74	0.68	0.58	0.42	0.45	1.32
R37.5	5.01	4.36	1.71	1.32	0.72	0.84	2.18	2.26	2.10	3.10	4.72	5.39	1.73	1.46	1.37	2.11	2.64	3.31	2.20	3.94	4.85	4.55	7.54	4.76	4.21	3.85	4.34	6.71	5.48
R50	2.30	3.49	3.17	3.92	0.89	1.93	3.25	6.17	2.48	3.88	2.67	3.44	2.74	5.50	4.26	7.26	2.90	4.80	1.75	4.50	2.51	4.47	4.22	3.92	9.15	2.99	2.65	5.03	6.22

Figure 7.28 – IR Results on Section 1

The conditions of the five cores previously retrieved are compared with the interpretation of the results from NDT devices in Table 7.5. The conditions of Cores C-15 (intact core) and C-18 (debonded core at 3 in.) as shown in Figure 7.29 correlated well with the results with the

PSPA and IR method. Some discrepancy was found on core C-17 (debonded at 6 in. depth), since PSPA showed marginal condition and IR intact condition, respectively.

Table 7.5 – Comparison of Core Conditions with NDT Results on Section 1

Core #	Location	GPR	PSPA	IR	Condition/Comments
C-15	929+50 @40'R	Intact	Intact	Intact	Intact
C-16	931+00 @60'R	Damaged	N/A	N/A	Intact
C-17	932+50 @10'L	Damaged	Marginal	Intact	Debonding at 6 in.
C-18	934+00 @10'R	Damaged	Damaged	Damaged	Debonding at 3 in.
C-19	935+50 @40'R	Damaged	N/A	N/A	Debonding at 7 in.

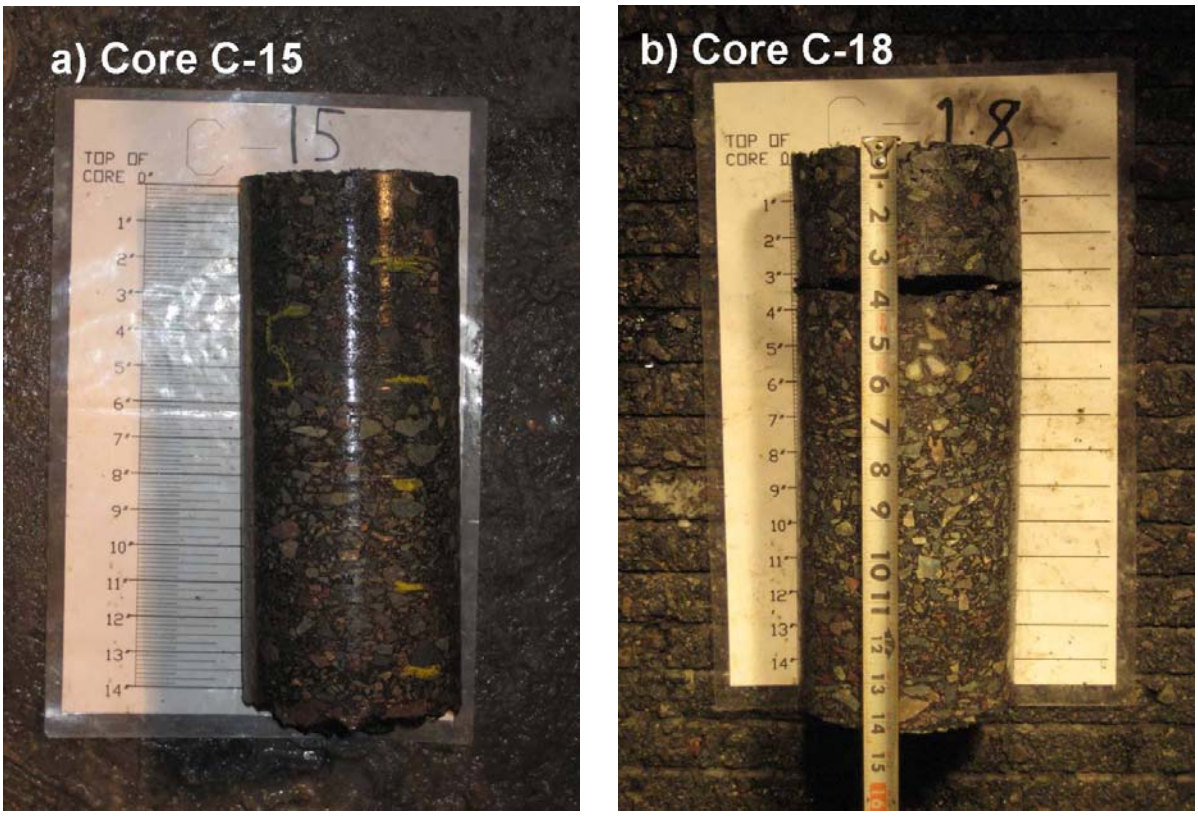

Figure 7.29 – Cores Retrieved from Section 1

Section 2

PSPA and IR results for the 15 core locations investigated are illustrated in Figure 7.30. All tests were carried out within 12 in. of the core locations. The GPR could not be used on this section because of the surface moisture present due to a rainfall.

Table 7.6 contains a comparison of the interpreted conditions from NDT methods and the actual conditions of the cores (see Figure 7.31). Most of the cores were retrieved as intact, with core lengths ranging from 13 in. to 18 in. The majority of the intact cores were classified as intact by the two NDT methods. For cores that presented debonding or stripping, the correlations were for the most part good. In general, the rate of success of the methods in the field was similar to those observed on the controlled section.

Core #	PSPA Modulus, ksi	IR FFT Ratios
C28	812	5.3
C29	1696	2.6
C30	377	2.7
C30A	812	5.8
C31	1613	9.4
C32A	966	8.3
C33	1029	9.6
C34	1197	6.9
C35A	343	4.8
C36	1278	8.2
C37	1542	4.9
C38	1599	3.7
C39	687	3.1
C40	814	2.0
C41	1391	4.8

Figure 7.30 – PSPA and IR Results on Section 2

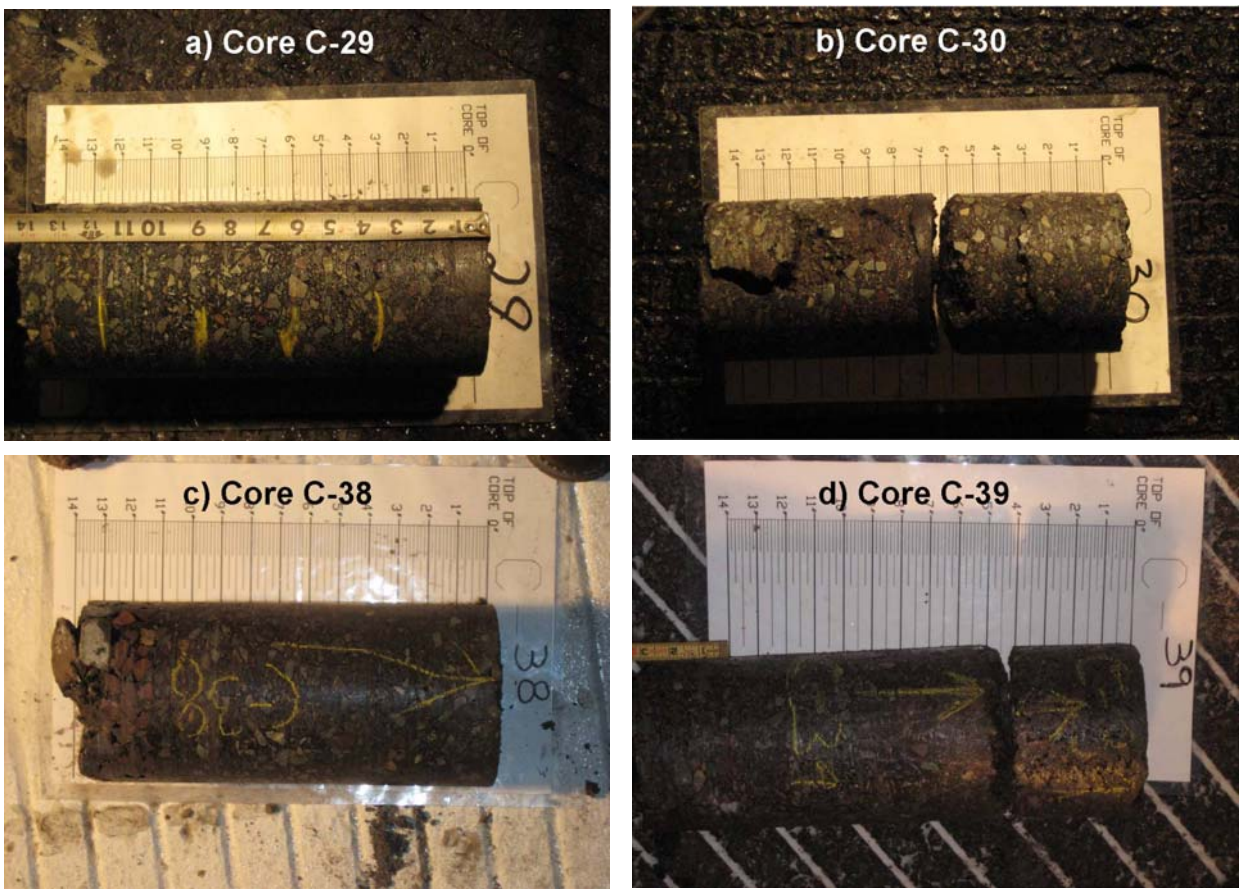

Figure 7.31 – Cores Retrieved from Section 2

These two case studies for the most part confirmed the reasonableness of the conclusions drawn from the controlled study. They also shed some light on some of the complexities of field testing. It seems that all mechanical NDT methods (PSPA, IR and FWD) can detect shallow severely debonded areas with reasonable certainty. The results from the GPR seem to be ambiguous. For complex pavement sections, the effectiveness of the FWD somewhat diminishes. One lesson learned is that the delineation of the low-quality HMA from debonded area is difficult from all mechanical NDT methods. More sophisticated processing of the data should be considered to see whether this problem can be overcome.

Table 7.6 – Comparison of Core Conditions with NDT Results on Section 2

Core #	Location	PSPA	IR	Condition/Comments
C-28	949+00 @40'L	Marginal	Intact	Intact
C-29	950+50 @10'L	Intact	Damaged	Intact
C-30	952+00 @10'R	Damaged	Damaged	Debonding at 6 in.
C-30A	952+05 @10'R	Marginal	Intact	Intact
C-31	953+50 @40'R	Intact	Intact	Intact
C-32A	954+95 @65'R	Intact	Intact	Intact
C-33	956+50 @60'L	Intact	Intact	Intact
C-34	958+00 @40'L	Intact	Intact	Intact
C-35A	959+50 @10'L	Damaged	Intact	Debonding at 7 in.
C-36	961+00 @10'R	Intact	Intact	Intact
C-37	962+50 @40'R	Intact	Intact	Core rig malfunctioned at core had to be stopped at 9 ½".
C-38	964+00 @60'R	Intact	Marginal	Intact
C-39	965+50 @60'L	Marginal	Marginal	Debonding at 4 in.
C-40	967+00 @40'L	Marginal	Damaged	Debonding at 4 in.
C-41	968+50 @10'L	Intact	Intact	Debonding at 4 in.

CHAPTER 8

EVALUATION OF NDT METHODS FOR DETECTING DELAMINATION OF HMA

The technical and practical parameters that most likely affect the successful detection of delamination with NDT methods include the accuracy, reproducibility, detectability threshold, speed of data collection, speed of data analysis, and the sophistication of data analysis. The approach applied to evaluate each of these parameters is briefly discussed in this chapter. Each of the criteria considered was assigned an individual ranking and a relative weight. The resulting weighted averages were used to rank the potential success of each method.

Accuracy

The accuracy was judged by correlating the response of the NDT methods to the degree of debonding induced in the sections. The accuracy of each method was determined using the criteria summarized in Table 8.1. The success was evaluated in percentage of correct assessment of the three levels of debonding considered. As an example, if the FWD returned an HMA modulus greater than the average minus -0.5 standard deviation (denoted as green in graphs in Chapter 6) for a given point, a value of 1 (or 100% success) was assigned to that point.

Table 8.1 – Criteria Used to Evaluate NDT Accuracy

Condition Measured with Device	Ranking Values								
	Intact			Full-Debonding			Partial-Debonding		
	Green[a]	Yellow[b]	Red[c]	Green[a]	Yellow[b]	Red[c]	Green[a]	Yellow[b]	Red[c]
Intact	1	0	0	--	--	--	--	--	--
Full-Debonding	--	--	--	0	0.5	1	--	--	--
Partial-Debonding	--	--	--	--	--	--	0	1	1

a Parameters above average minus one-half standard deviation
b Parameters between average minus one-half standard deviation and average minus one standard deviation
c Parameters below the average below one standard deviation (substantially less stiff than the control)

However, if the estimated modulus was less than the average minus -0.5 standard deviation (denoted as yellow or red in graphs in Chapter 6), a value of 0 (or a false positive) was assigned to it.

The percentage of success for every method and for every level of bonding was obtained by adding the values from all points in a given debonding category to obtain a score. This score was divided by the total number of points to define the degree of success. As such, for the case of the cool weather FWD deflection testing, the degree of success for detecting partial debonding and full-debonding in cool weather testing were about 65% and 50%, respectively. For the ground-coupled GPR, observed lengths of bonding/debonding on each line corresponding to each bonding level were measured from the linescans and were divided by the actual length corresponding to a level of debonding to obtain the degree of success.

Table 8.2 contains a summary of the degrees of success of the feasible techniques based on the criteria described above. Almost all methods interpret the intact points at a degree of better than 80%. The probability of success of detecting the fully-debonded and partially-debonded sections varied from 26% for GPR to about 70%.

Based on these results, the degree of success of different methods for detecting different defect types were ranked between 0 and 5 using the criteria in Table 8.3. The aggregate ranking of each method for different testing temperature was then obtained by considering the weighted average of the rankings for each bonding category as shown in Table 8.2.

Since detecting the fully-debonded areas are the most critical, a weight factor of 3 was assigned to the ranking for that bonding condition, while a weight of 1 was assigned to the ranking of the intact points and 3 to the ranking of the partially-debonded areas. The major observation from these rankings is that all methods work better in cool weather. Based on the

Table 8.2 – Ranking of Probability of Success of NDT Methods to Detect Delamination

Device/ Analysis Method	Test Period	Degree of Bonding	Probability of Success	Ranking by Degree of Bonding	Ranking by Test Period	Overall Ranking of Technology
PSPA/ USW	Cool	Intact	86%	5	3.1	3
		Full-debonding	60%	3		
		Partial-debonding	55%	3		
	Hot	Intact	82%	5	1.9	
		Full-debonding	60%	3		
		Partial-debonding	37%	1		
FWD/ Deflection	Cool	Intact	89%	5	3.1	3
		Full-debonding	49%	3		
		Partial-debonding	67%	3		
	Hot	Intact	82%	5	1.9	
		Full-debonding	52%	3		
		Partial-debonding	44%	1		
FWD/ Modulus	Cool	Intact	87%	5	1.9	2
		Full-debonding	70%	3		
		Partial-debonding	33%	1		
	Hot	Intact	61%	3	1.2	
		Full-debonding	54%	3		
		Partial-debonding	28%	0		
IR/ Flexibility	Cool	Intact	88%	5	3.8	4
		Full-debonding	72%	5		
		Partial-debonding	51%	3		
	Hot	Intact	89%	5	1.9	
		Full-debonding	67%	3		
		Partial-debonding	47%	1		
GPR/ Ground Coupled	--	Intact	90%	5	0.9	1
		Full-debonding	26%	0		
		Partial-debonding	41%	1		

Table 8.3 – Ranking Criteria for Accuracy of Different Methods

Probability of Detection		Ranking
Minimum	Maximum	
70	100	5
50	70	3
35	50	1
0	**35**	**0**

average of the rankings of the cool and hot weather tests, as reflected in Table 8.2, the impulse response method is the most accurate followed by the USW and FWD deflections. Interestingly, the backcalculation of the HMA layer modulus negatively impacted the accuracy of that method.

Most of the 26% to 40% of GPR detected debonded areas correspond to the defects that were constructed with either clay or talcum powder with significantly different dielectric constant than HMA. In practical terms, this indicates that the GPR may be quite successful, if moisture penetrates in the interface of the debonded layers.

Several other methods that were not as successful as anticipated in our initial work plan were not extensively tested and were not considered in the ranking.

Reproducibility

The reproducibility associated with different test procedures was quantified by conducting triplicate tests with each NDT device. Based on the degree of success of the methods, only the reproducibility of the FWD, PSPA and IR were evaluated. The GPR has shown good repeatability in many applications other than detecting debonding.

The results of the reproducibility tests for the three methods and for the cool and hot weather testing are summarized in Table 8.4. The coefficient of variation from the results of the three independent tests at each point was used to describe the reproducibility. However, for the

Table 8.4 – Reproducibility of NDT Methods

NDT Device	Weather		Coarse Surface Mix					Fine Surface Mix					Ranking
			S1	S2	S3	S4	S5	S6	S7	S8	S9	S10	
IR (FFT Ratio)	Cool	COV	4.3%	4.4%	4.6%	4.2%	3.7%	4.2%	6.0%	4.9%	5.3%	4.5%	5
		Avg.	4.2%					5.0%					
	Hot	COV	4.9%	5.9%	4.5%	5.3%	5.5%	4.7%	4.6%	6.5%	6.3%	5.6%	
		Avg.	5.2%					5.5%					
PSPA (Modulus)	Cool	COV	9.8%	9.4%	8.6%	9.6%	8.7%	9.8%	8.9%	8.6%	8.2%	9.0%	3
		Avg.	9.2%					8.9%					
	Hot	COV	6.8%	7.0%	8.6%	8.4%	7.7%	8.6%	10.5%	10.0%	9.1%	8.5%	
		Avg.	7.7%					9.3%					
FWD (Deflections)	Cool	COV	0.6%	0.5%	0.4%	0.5%	0.8%	0.4%	0.4%	0.5%	0.6%	0.8%	5
		Avg.	0.6%					0.6%					
	Hot	COV	1.3%	1.7%	1.5%	1.7%	1.4%	1.5%	1.7%	1.6%	1.2%	1.4%	
		Avg.	1.5%					1.4%					
FWD (Modulus)	Cool	COV	9.6%	6.8%	5.7%	6.1%	12.1%	1.8%	1.7%	1.9%	6.5%	5.6%	5
		Avg.	8.1%					3.5%					
	Hot	COV	4.9%	4.2%	3.8%	3.5%	3.9%	6.0%	4.5%	4.6%	7.2%	4.6%	
		Avg.	4.1%					5.4%					

FWD, because of the logistics, the last three deflections measured without moving the FWD were used. This practice slightly favors the reproducibility of the FWD reported. Rocha et al. (2004) amongst others have shown that the reproducibility of FWD without moving is better than 2% (as is the case here) and better than 5% when the FWD is resituated on a given point. In general, the reproducibility of all methods is better than 10% which is quite reasonable. IR results demonstrated an average COV of about 5%. Based on the average COV values, a ranking is assigned to the reproducibility of each method in Table 8.4.

Detectability Threshold

As reflected in Chapter 4, aside from the 4 ft by 9 ft (1.2 m by 3 m) debonded areas, smaller areas varying from 2 ft by 2 ft (0.6 m by 0.6 m) to 1 ft by 1 ft (0.3 m by 0.3 m) and 0.5 ft by 0.5 ft (0.15 m by 0.15 m) were also introduced in the sections. The outcomes of different technologies on different size defects in terms of detectability were compared to establish the detectability threshold. A comprehensive table that provides the probability of detection as functions of defect size, bonding condition, type of mix and weather condition, is included in Appendix G. Those results are summarized in Figure 8.1. As the defects become smaller and deeper, the predictive power of the selected methods diminishes.

To better quantify the detectability threshold, the percent of defects identified as a function of size, depth and severity were ranked based on the criteria described in Table 8.3. Those results are presented in Table 8.5. A weight factor was assigned to each severity and depth based on how critical they are to the safe operation of an airfield, with 4 being the weight for the shallow fully debonded points and 1 being the weight for the deep partially debonded points. Based on Table 8.5, the degree of success for detecting the 1 ft and 0.5 ft debonded areas are almost nil independent of the technology. The 4 ft by 9 ft debonded areas, especially the shallow fully-debonded ones, can be detected by most technologies with reasonable certainty; while the chance of detecting the 2 ft debonded areas are small. Given the fact that the most feasible technologies are point tests, it can be concluded that the debonded area should be at least 4 ft (1.2 m) in dimensions to be detectable.

Based on the analysis provided in Table 8.5, the Impulse Response and USW methods in relative terms rank somewhat better than FWD for detecting the large debonded areas and

significantly better than FWD for the 2 ft defects. As such, the detectability threshold of the IR and PSPA methods are ranked as 3 and FWD as 1.

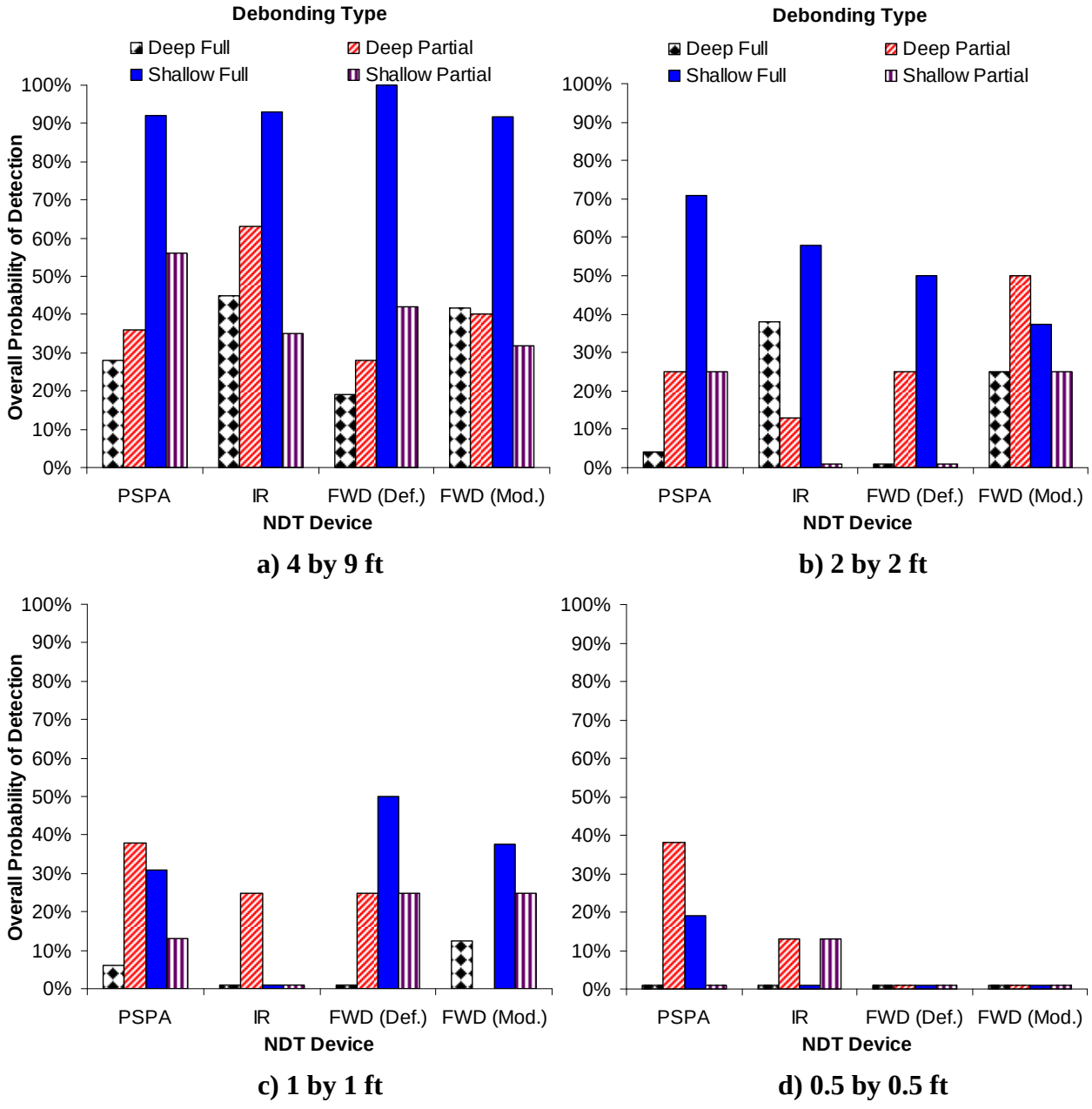

Figure 8.1 – Overall Probability of Detection of NDT Methods

Table 8.5 – Ranking of Detectability Threshold

Defect Size (ft)	Defect Type	Weight Factor	Detection Ranking				Average for all Technologies
			PSPA	IR	FWD (Def.)	FWD (Mod.)	
4 by 9	Deep Full	2	0	1	0	1	0
	Deep Partial	1	1	3	0	1	1
	Shallow Full	4	5	5	5	5	5
	Shallow Partial	3	3	1	1	0	1
	Overall	--	**3.0**	**2.8**	**2.3**	**2.3**	**2.4**
2 by 2	Deep Full	2	0	1	0	0	0
	Deep Partial	1	0	0	0	1	0
	Shallow Full	4	5	3	1	1	3
	Shallow Partial	3	0	0	0	0	0
	Overall	--	**2.0**	**1.4**	**0.4**	**0.5**	**1.2**
1 by 1	Deep Full	2	0	0	0	0	0
	Deep Partial	1	1	0	0	0	0
	Shallow Full	4	0	0	1	1	0
	Shallow Partial	3	0	0	0	0	0
	Overall	--	**0.1**	**0.0**	**0.4**	**0.4**	**0.0**
0.5 by 0.5	Deep Full	2	0	0	0	0	0
	Deep Partial	1	1	0	0	0	0
	Shallow Full	4	0	0	0	0	0
	Shallow Partial	3	0	0	0	0	0
	Overall	--	**0.1**	**0.0**	**0.0**	**0.0**	**0.0**

Speed of Data Collection

The speed of data collection for each NDT method is summarized on Table 8.6. For the methods that collect data in a continuous form, the time needed to complete a 100 ft (30 m) longitudinal line is reported. For the methods that collect point by point data, the time required to complete a test is shown. In addition, the time needed to complete the setup of each device before testing is included for reference. Based on this information a ranking of each technology is also included in Table 8.6. Continuous methods were assigned a value of 5 (high) and point by point methods received a value of 3 (medium) since the time needed to collect a point was less than two minutes.

Table 8.6 – Ranking of Speed of Data Collection

NDT Device	Setup Time, minutes	Point Test, seconds	Ranking
PSPA	10	15	3
FWD	20	120	3
IR	15	30	3
Thermal	1	10	5
GPR. Ground Antenna	45	120*	5
GPR. Air Antenna	30	60*	5

** Time needed to collect a longitudinal line on the small scale study (100 ft)*

Speed of Data Analysis

The time to complete the analysis of the raw data for each methodology is reported on Table 8.7 as a way of comparison of the speed of analysis for all NDT methods. This parameter also serves as an estimator of the difficulty and experience needed to complete the data analysis. Similar to other parameters, a ranking from 1 to 5 was given to each method. The analysis and interpretation times can be significantly improved when the methods are accepted and automated for the purpose of day to day use. Most of the analysis time for most methods was actually arranging and organizing the results that can be reduce to a minimum if the GPS coordinates of the test points were known and a custom tool were developed to conveniently visualize them.

Table 8.7 – Ranking of Speed of Data Analysis and Interpretation

NDT Device	Analysis Time of Raw Data, sec	Interpretation Time to Assess Debonding, days	Ranking
PSPA	Real Time	2	3
FWD	Real Time	2	3
IR	Real time	2	3
Thermal	Real Time	1	5
GPR. Ground Antenna	1 day	3	1
GPR. Air Antenna	1 day	3	1

Sophistication of Data Analysis

Complexity of data analysis was estimated and summarized in Table 8.8. This was achieved by asking UTEP personnel with different levels of experience to conduct the analysis. The following three levels of experience were considered: 1) an expert, 2) a person that is familiar with the method (intermediate user), and 3) a new user that was just trained. A ranking of 1 (low), 3 (average) or 5 (high) was correspondingly selected. Reduced data from each of the selected personnel was compared and the difficulties associated with each device or reduction software is reported as well.

Table 8.8 – Ranking of Sophistication of Data Analysis Needed and Difficulties Found

NDT Device	Experience Level Needed	Ranking	Difficulties Found
PSPA	Intermediate User	3	Setting parameters can be initially confusing.
FWD	Intermediate User	3	Different parameters on the backcalculation software may lead to considerably different results.
IR	Intermediate User	3	Initial confusion with frequency-domain analysis.
Thermal	New User	5	None.
GPR	Expert	1	Reduction software complicated to use and interpretation not always intuitive.

Overall Ranking of Candidate NDT Methods

The parameters described above were given relative weights to determine an overall ranking for different methods. The relative weights, which are similar to those used in Phase I of this project to conceptually rank the methods, are summarized in Table 8.9. The first three parameters were given higher weights since they are the most important factors in deciding whether a method is appropriate or not. Accuracy was determined as the most important parameter. Time required for data collection was weighted slightly higher than other practical

parameters since the timely collection of information deemed important to the day-to-day operation of an airfield. The data analysis and data presentation is rather important but they were not deemed as important as other practical items.

Table 8.9 – Utility Weights for Selection of NDT Methods

Evaluation Category		Relative Weight
1	Accuracy	0.35
2	Reproducibility	0.20
3	Detectability Threshold	0.20
4	Speed of Data Collection	0.15
5	Speed of Data Analysis	0.05
6	Sophistication of Data Analysis	0.05
Total		**1.00**

Based on the ranking in Table 8.10, the Impulse Response is ranked the highest, with the PSPA and FWD using the deflection of the first sensor ranking closely with it. The ground penetrating radar and the thermal imaging, which have the potential for rapid data collection, do not seem as feasible as the others.

Table 8.10 – Final Ranking of Feasible NDT Methods

Parameter / Method	Accuracy	Reproducibility	Detectability Threshold	Speed of Data Collection	Speed of Data Analysis	Sophistication of Data Analysis	Ranking
	Weight Factor						
	0.35	0.2	0.2	0.15	0.05	0.05	
PSPA/ Ultrasonic Surface waves	3	3	3	3	3	3	3
FWD Deflection	3	5	1	3	3	3	3
FWD Modulus	2	3	1	3	3	3	2
Impulse Response	4	5	3	3	3	3	4
GPR Ground Coupled	1	5	1	5	1	1	2

CHAPTER 9

SUMMARY, CONCLUSIONS AND RECOMMENDATIONS

Summary

A number of NDT methods were evaluated in term of their utility to detected debonding of HMA layers. Based on an extensive information search, the following technologies were considered:

- Falling Weight Deflectometer (FWD)
- Ground Penetrating Radar (GPR)
- High Frequency Sweep (HFS)
- Impact Echo (IE)
- Impulse Response (IR)
- Light Weight Deflectometer (LWD)
- Stiffness Gauge (SG)
- Thermal Imaging (TI)
- Ultrasonic Surface Waves (USW)

A 10 ft by 130 ft (3 m by 40 m) pavement section was constructed with two different mixes specifically to evaluate these methods. The test section contained the following defects:

- Extensively delaminated
- Shallow fully-debonded
- Shallow partially-debonded
- Deep fully-debonded
- Deep partially-debonded

Based on a preliminary study, the methods that were deemed the most promising were the following:

- Falling Weight Deflectometer (FWD)
- Ground-Coupled Ground Penetrating Radar (GPR)
- Impulse Response (IR)
- Ultrasonic Surface Waves (USW)

These methods were extensively studied in cool and hot weather for a number of technical and practical parameters that deem necessary for a tool be considered successful for assessing debonding. These parameters in the order of their perceived significance included the following:

1. Accuracy
2. Reproducibility
3. Detectability Threshold
4. Speed of Data Collection
5. Speed of Data Analysis
6. Sophistication of Data Analysis

Based on this evaluation, the three most promising technologies are the Impulse Response, Ultrasonic Surface Waves and the Falling Weight Deflectometer.

Based on field testing at two airports, the observations made above seem to be quite reasonable in actual field conditions.

Conclusions

Based on this study, the following conclusions can be drawn.

- **Accuracy**
  - No single method could detect all the defects incorporated in the test section.
  - The most critical defects, extensive delamination and shallow fully-debonded areas, could be detected with a degree of success of about 90% by all three methods.
  - The shallow partially debonded areas, which is the most desirable to detect, was detected at a rate of success of 60% by the PSPA and about 30 to 40% by the other two methods.
  - The Impulse Response method performed best for detecting deep fully-debonded areas, however, the detection of the deep partially debonded areas is rather difficult. The rates of success of the three devices to detect deep debonding were 30% to 45%.
  - All methods can detect debonding more readily in the cool weather than the hot weather.
- **Reproducibility**
  - The short term reproducibility of all methods is reasonably good and varies between 5 to 10%.
  - In terms of long term reproducibility (yielding the same conclusions between cool and hot weather tests), the Impulse Response and PSPA performed more favorably than FWD.
- **Detectability Threshold**
  - The practical size of the debonded area that can be detected is about 4 ft (1.2 m).
  - None of the methods could detect defects less than 2 ft in dimensions.
  - PSPA and IR because of their size had higher detectability threshold than the FWD.
  -

- **Speed of Data Collection**
  - Data collection can be carried out in less than 2 minutes with all three devices.
  - The PSPA and IR device can collect data at twice the rate of an FWD.

- **Speed of Data Analysis and Interpretation**
  - All three devices provide the analysis in real time.
  - The current data interpretation is rather straight forward for the three methods.

- **Sophistication of Data Analysis**
  - The data analysis with the IR and PSPA are the most sophisticated yet the most certain.
  - The FWD analysis is rather straightforward, but an experienced analyst is needed to minimize the uncertainty in the backcalculation.

Recommendations

- Based on extensive numerical analyses (not included in this report), it is possible to implement more sophisticated yet practical analyses, at least for the USW and IR methods. This option should be pursued in future studies.
- For the promising techniques, the delineation between low quality HMA and debonded areas is difficult since the detection of debonding is based on relative changes in parameters in the feature tested. The utilization of more sophisticated analyses should address this shortcoming.
- Since the most promising methods are based on spot tests, the feasibility of developing more automated means of performing these tests should be explored. This can range from autonomous scanning devices to rolling sensors.

- Most of the interoperation time for all methods is associated with tedious development of visual tools, such as contour maps. By adding a GPS unit and developing custom-made visualization routines, this matter can be remedied.
- Since the results of the promising methods are temperature dependent, a straightforward temperature adjustment scheme should be developed, especially for the IR method and the FWD.

REFERENCES

Al Hakim, B., Armitage, R., and Thom, N. H. (1998). ‘‘Pavement assessment including bonding condition: case studies.’’ Proceedings, 5th International Conference on Bearing Capacity of Roads and Airfields, University of Trondheim, Trondheim, Norway, 1, 439–448.

Ameri-Gaznon, M., and Little, D., “Octahedral Shear Stress Analyses on an ACP Overlay on a Rigid Base,” Proceedings of the Association of Asphalt Paving Technologists, vol. 59, pp. 443-479, 1990.

Armitage, R. J., Kruntcheva, M. R., and Willett, M. R. (2000). ‘‘Trials of the Portable Seismic Pavement Analyzer (PSPA).’’ Report Prepared for Highways Agency, Pavement Engineering Group, Scott Wilson Pavement Engineering, Nottingham, U.K.

Asphalt Institute, “Asphalt in Pavement Maintenance,” Manual Series No. 16 (MS-16), Third Edition.

Bognacki, C. J., Frisvold, A. and Bennert, T. (2007), “Investigation of asphalt pavement slippage failures on Runway 4R-22L, Newark International Airport.” FAA Worldwide Airport Technology Transfer Conference. Atlantic City, New Jersey, USA.

Bonnaure, F., Gavois, A., and Udron, J., “A New Method for Predicting the Fatigue Life of Bituminous Mixes,” Proceedings of the Association of Asphalt Paving Technologists, vol. 49, pp. 499-529, 1980.

Carroll, N., M., and Dempsey, B., J. (2007), “Anti-Icing Pavement Coating Study at Chicago O’Hare International Airport. Report No. DOT/FAA/AR-06/58, U.S. DOT, FAA.

Department of the Air Force. Engineering Technical Letter (ETL) 02-7: Preventing Concrete Deterioration under B-1 and F/A-18 Aircraft, August 7, 2002.

Eedula ,S., and Tandon, V. (2006), "Tack Coat field acceptance criterion," Research Report 0-5216-1, Center for Transportation Infrastructure Systems, UTEP, El Paso, TX.

Garbacz, A. and Garboczi, E. J. "Ultrasonic Evaluation Methods Applicable to Polymer Concrete Composites." NISTIR 6975; 73 p. April 2003. National Institute of Standards and Technology, Gaithersburg, MD 20899.

Gomba, S.M. (2004) "Evaluation of interlayer bonding in hot mix asphalt pavements." Master Thesis. Rowan University, Glassboro, New Jersey.

Hammons, M., I., Von Quintus, H., Maser, K., and Nazarian, S. (2005) "Detection of stripping in hot mix asphalt." Applied Research Associates Project Number 16355, prepared for: Office of Materials and Research, Georgia Department of Transportation.

Hachiya, Y., and Sato, K., "Effect of Tack Coat on Bonding Characteristics at Interface between Asphalt Concrete Layers," Proceedings of 8th International Conference on Asphalt Pavements, vol. 1, pp. 349-362, 1997.

Kruntcheva, M., R., Collop, A., C. and Thom, N., H. (2004) "Feasibility of assessing bond condition of asphalt concrete layers with dynamic nondestructive testing." Journal of Transportation Engineering, Vol. 130, No. 4.

Kruntcheva, M. R., Collop, A. C., and Thom, N. H. (2005). "Effect of Bond Condition on Flexible Pavement Performance." Journal of Transportation Engineering, Volume 131, Issue 11, pp. 880-888, November 2005.

Kruntcheva, M., R., Collop, A., C. and Thom, N., H. (2006) "Properties of asphalt concrete layer interfaces. Journal of Materials in Civil Engineering, Vol. 18, No. 3.

Kulkarni, M., B. (2004) "Effect of tack and prime coats, and bag-house fines on composite asphalt pavements." Ph.D. Dissertation, North Carolina State University, Raleigh, NC.

Lepert, P., Poilane, J. P., and Villard-Bats, M. (1992). “Evaluation of various field measurement techniques for the assessment of pavement interface condition.” Proceedings, 7th International Conference on Asphalt Pavements, Vol. 3, 224–237.

Li, Y., and Nazarian, S. (1994), “Evaluation of Aging of Hot-Mix Asphalt Using Wave Propagation Techniques,” Engineering Properties of Asphalt Mixtures And the Relationship to Their Performance, ASTM STP 1265, Philadelphia, Pa., pp.166-179.

Liu, W. and Scullion, T. “MODULUS 6.0 for Windows: User's Manual,” Research report 0-1869-2. Texas Transportation Institute, College Station, TX, October 2001.

Mohammad, L. N., Raqib, M. A., and Huang, B., “Influence of Asphalt Tack Coat Materials on Interface Shear Strength,” Transportation Research Record, no 1789, pp. 56-65, 2002.

Moropoulou, A., Avdelidis, N., P., Koui, M., and Kakaras, K. (2002) “Flaw detection and evaluation of airport pavements by means of infrared thermography.” http://www.flirthermography.com/media/Detection_Evaluation_Airport_Paving.pdf

Mukhtar, M. T., and Dempsey, B. J., “Interlayer Stress Absorbing Composite (ISAC) for Mitigating Reflection Cracking in Asphalt Concrete Overlays,” Final Report Project IHR-533, Illinois Cooperative Highway Research Program, June, 1996.

Nazarian, S., M. Baker, and K. Crain. 1997. "Assessing Quality of Concrete with Wave Propagation Techniques," Materials Journal, ACI, Farmington Hills, MI, Vol. 94 (4) 296-306

Newman, K., and Shoenberger, J., E. (2002), “Polymer concrete micro-overlay for fuel and abrasion resistant surfacing: laboratory results and field demonstrations.” 2002 FAA Airport Technology Transfer Conference.

Rocha, S., Tandon, V., and Nazarian, S., "Falling Weight Deflectometer Fleet: Repeatability and Reproducibility," International Journal of Road Materials and Pavement Design, Volume 5 – Issue 2/2004, pp. 215-238.

Sangiorgi, C., Collop, A., C. and Thom, N., H. (2003) "A nondestructive impulse hammer for evaluating the bond between asphalt layers in a road pavement." Non-Destructive Testing in Civil Engineering, International Symposium, Liverpool, UK.

Shahin, M. Y., Kirchner, K., Blackmon, E.W., and Tomita, H., "Effect of Layer Slippage on Performance of Asphalt-Concrete Pavements," Transportation Research Record, no. 1095, pp. 79-85, 1986.

Shahin M.Y. Pavement management for airports, Roads and Parking Lots. Springer, 2005.

Sholar, G. A., Page, G. C., Musselman, J. A., Upshaw, P. B., Moseley, H. L., "Preliminary Investigation of a Test Method to Evaluate Bond Strength of Bituminous Tack Coats," Proceedings of the Association of Asphalt Paving Technologists, Preprints, pp. 107-137, 2004.

Smith, S., S., Scullion, T. Development of Ground-Penetrating Radar Equipment for Detecting Pavement Condition for Preventive Maintenance. SHRP-H-672. Strategic Highway Research Program. National Research Council Washington, DC 1993.

Tschegg, E., Kroer, G., Tan, D., Stanzl-Tschegg, S., and Litzka, J., "Investigation of Bonding between Asphalt Layers on Road Construction," Journal of Transportation Engineering, vol. 121, no. 4, pp. 309-316, 1995.

Tsubokawa, Y., Mizukami, J., Esaki, T., and Hayano, K. (2007) "Study on infrared thermographic inspection of de-bonded layer of airport flexible pavement." FAA Worldwide Airport Technology Transfer Conference. Atlantic City, New Jersey.

Uzan, J., “Influence of the Interface Condition on Stress Distribution in a Layered System,” Transportation Research Record, no. 616, pp. 71-73, 1976.

Uzan, J., Livneh, M., and Eshed, Y., “Investigation of Adhesion Properties between Asphaltic-Concrete Layers,” Proceedings of the Association of Asphalt Paving Technologists, vol. 47, pp. 495-521, 1978.

West, Randy C; Moore, Jason R; Zhang, Jingna, “Evaluating Tack Coat Applications and the Bond Strength between Pavement Layers,” Proceedings of the 2006 Airfield and Highway Pavement Specialty Conference, ASCE, pp, 578-588, 2006.